ON-LINE PERFORMANCE PARAMETER ESTIMATION OF SR-30 TURBOJET ENGINE

By

Joaquín Miguel Valencia Bravo

A thesis submitted in partial fulfillment of the requirements for the degree of

MASTER OF SCIENCE

in

MECHANICAL ENGINEERING

UNIVERSITY OF PUERTO RICO
MAYAGÜEZ CAMPUS

December, 2010

Approved by:

Frederick Just, Ph.D Member, Graduate Committee	Date
Orlando E. Ruiz, Ph.D Member, Graduate Committee	Date
David Serrano, Sc.D President, Graduate Committee	Date
Edgardo Lorenzo, Ph.D Representative of Graduate Studies	Date
Gustavo Gutierrez, Ph.D Chairperson of the Department	Date

Abstract of Dissertation Presented to the Graduate School
of the University of Puerto Rico in Partial Fulfillment of the
Requirements for the Degree of Master of Science

ON-LINE PERFORMANCE PARAMETER ESTIMATION OF SR-30 TURBOJET ENGINE

By

Joaquín Miguel Valencia Bravo

December 2010

Chair: David Serrano
Major Department: Mechanical Engineering

Accurate estimation of jet engines performance parameters is the key to develop reliable diagnostics systems. The development of a reliable and accurate nonlinear model of the SR-30 turbojet engine is proposed.

To comply with this general objective, it was necessary to achieve specific objectives. Models of the compressor and turbine characteristic maps were required and developed. These models were constructed based on SR-30 engine's dimensions, fundamental theory and initial conditions of operation. A nonlinear model was developed for the SR-30 engine and implemented using Simulink. Resulting model is based on nested iterations, two iterations are used for the steady state performance model and one iteration for the transient state model. The characteristic maps developed are crucial for the steady state behavior of the engine model. The nonlinear engine model was validated using experimental data obtained from actual SR-30 test runs, using the same command input, to produce the system output.

Correction factors were used, before implementing the Kalman filter estimator, to improve the model results.

For the tuning/fitting procedure, the dual unscented Kalman filter (DUKF) was developed. DUKF is based on two Kalman filters which work simultaneously; one of these is the state estimation filter and the other is the parameter estimation filter. DUKF uses the residual parameter vector, which is the difference between the model outputs and the measured outputs, to modify the tuners. The tuners are health parameters, such as efficiency and flow capacity which represent performance deteriorations of engine components. These tuners are used to adjust the output engine model parameters to closely match the measured values. The simulation results with the use of correction factors, were satisfactory. However, the results were improved by using the DUKF. Areas for future work are identified.

Resumen de Disertación Presentado a Escuela Graduada
de la Universidad de Puerto Rico como requisito parcial de los
Requerimientos para el grado de Maestría en Ciencias

ESTIMACIÓN DE PARÁMETROS DE COMPORTAMIENTO EN-LÍNEA DEL MOTOR TURBORREACTOR SR-30

Por

Joaquín Miguel Valencia Bravo

Diciembre 2010

Consejero: David Serrano
Departamento: Ingeniería Mecánica

La estimación precisa de los parámetros de comportamiento de los motores a reacción es la clave para desarrollar sistemas de diagnóstico fiables. En el presente trabajo, se ha propuesto desarrollar un modelo confiable y preciso del motor turborreactor SR-30.

Para cumplir con este objetivo general, fue necesario cumplir con algunos objetivos específicos. Se desarrolló el modelo de los mapas característicos del compresor y de la turbina. Estos modelos se construyeron basado en sus dimensiones y las condiciones iniciales de funcionamiento. A continuación, un modelo no lineal ha sido desarrollado para el motor SR-30. Este modelo esta basado en iteraciones anidadas; dos iteraciones fueron usadas para el modelamiento del comportamiento en estado estacionario y una iteración para modelar el estado transitorio. Los mapas característicos, los cuales fueron cargados en el modelo del motor, son cruciales para el modelamiento del comportamiento en estado estacionario. El modelo no lineal del motor y la datos experimentales, usan el mismo comando de entrada para producir

los resultados. Factores de corrección se utilizaron, antes de usar el estimador del filtro de Kalman, con el fin de mejorar los resultados.

Para el procedimiento de ajuste, el dual uncscented Kalman filter (DUKF) fue desarrollado. DUKF se basa en dos filtros de Kalman que trabajan al mismo tiempo, una sirve para estimar los estados variables y el otro para estimar los parmetros de comportamiento. DUKF utiliza el vector de parámetros residuales, que es la diferencia entre los resultados del modelo y los resultados medidos, para modificar los parametros de ajuste (parmetros de salud, tales como la eficiencia y la capacidad de flujo, que representan el deterioro del comportamiento de los componentes del motor). Este parámetros de ajuste se utilizan para hacer el ajuste de los parámetros de salida del modelo del motor con la finalidad de que coincidan con los valores medidos.

Esta técnica se ha desarrollado y algunos resultados experimentales del motor turborreactor RS-30 se utilizó para su validación. La resultados de la simulación con el uso de factores de corrección, fue satisfactorio. Sin embargo, estos resultados fueron mejorados por el filtro dual DUKF. Se identificaron areas para trabajos futuros en cuanto al modelaje y aplicaciones a sistemas de diagnóstico.

To my family

ACKNOWLEDGMENTS

To Pratt & Whitney which is the institution that supported this work.

To Dr. Allan Volponi for his comments which helped improve the results of this work.

To Dr. Frederick Just and Dr. Orlando Ruiz for their observations, recommendations and willingness to help improve the thesis.

To my advisor, Dr. David Serrano, for his guidance and recommendations in the development of this work.

To the Mechanical Engineering Department of Interamericana University for allowing me to use the SR-30 gas turbine located in its laboratory.

And thanks to the Mechanical Engineering Department of the University of Puerto Rico Mayagüez Campus for allowing me to do my Masters studies.

TABLE OF CONTENTS

LIST OF TABLES

LIST OF FIGURES

LIST OF ABBREVIATIONS

TIT	Turbine Inlet Temperature.
SOT	Stator Outlet Temperature.
FAR	Fuel-air ratio.
UKF	Unscented Kalman Filter.
UT	Unscented transformation.
DUKF	Dual Unscented Kalman Filter.
MSE	Mean Square Error.
RR	Radius ratio.
PLF	Pressure loss factor.
LHV	Lower Heating Value.

LIST OF SYMBOLS

A_1	Area at impeller inlet
A_t	Average annulus area at the turbine.
A_{mc}	Maximum cross-sectional area of the combustor.
b_{2I}	Axial width at impeller exit.
b	Blade.
C_D	Drag coefficient.
C_L	Lift coefficient.
CL	Combustor loading.
c_p	specific heat at constant pressure.
C	Absolute flow velocity.
C_{w1}	Pre-swirl of the flow.
C_{w2I}	Swirl component of the absolute velocity at impeller exit.
C_{r2I}	Radial component of the absolute velocity at impeller exit.
C_1	Absolute velocity at compressor exit.
C_{a1}	Axial component of the absolute velocity.
C_a	= Free stream flow velocity.
d_0	Pitch circle diameter.
d_0	Dynamic pressure.
dH/T	Work parameter.
D_1	Mean diameter at compressor inlet.
D_t	Diameter at the impeller tip.
D_r	Diameter at the impeller root.
e	Mean radius of curvature ($e = 20$).
$f_*()$	Function of.
f_g	Coefficient which depend on the type of bearing.
E	Denote mathematical expectation.
F_0	Constant (use in slip factor equation)
F_N	Net thrust.
h	Specific enthalpy or health parameters.
h_{ref}	Referential specific enthalpy.
H	Blade height.
l	Chord length.
L	Is the state dimension.
ka1	Pressure loss coefficient at the intake.
ka45	Pressure loss coefficient at the nozzle.
K	Kalman gain matrix.
K_{cold}	Cold loss factor.
K_{hot}	Hot loss factor.

$\dot{m}$	Mass flow.
$\dot{m}_a$	Stream air mass flow.
M	Mach number.
M_a	Inlet Mach number.
n_b	Number of blades or number of bearings.
N	Rotational speed.
P	Covariance.
PW_{loss}	Power loss.
PW_t	Turbine output power.
PW_c	Compressor output power.
p_a	Ambient pressure.
p_{0a}	Stream ambient pressure.
p_{01}	Stagnation or total pressure at impeller inlet.
PR_c	Compressure pressure ratio.
Q_{tcal}	Capacity calculated from the flow path in the turbine.
Q_{tmap}	Capacity obtained from the turbine map.
$\dot{Q}_{in}$	Heat released by the fuel.
r	Residual.
R	Gas constant for an individual gas (dry air of combustion products)
s	Distance between blades (pitch).
t	Thickness.
T_a	Ambient temperature.
T_{0a}	Stream stagnation (total) temperature.
r_1	Mean radius at impeller eye.
r_{2I}	Radius at impeller exit.
Re	Reynolds number.
T	Static temperature.
T_{ref}	Referential static temperature.
u	Control command inputs.
U_1	Tangential velocity of the blades at the impeller eye.
U_{2I}	Tangential velocity of the blades at the impeller tip.
U_t	Tangential velocity at impeller tip.
U_r	Tangential velocity at impeller root.
V_1	Relative flow velocity at compressor inlet.
VOL	Can volume of the combustion chamber.
w	Weights for the neural networks.
$W_i^{(c)}, W_i^{(m)}$	Weights.
x	Vector of state variables.
y	Measurable outputs vector.
Y_p	Profile loss coefficient.
$\sqrt{P}$	Is the i^{th} column of the matrix square root (lower triangular cholesky factorization).
Δh_{euler}	The ideal specific enthalpy change of the working fluid.
Δh_{int}	Internal loss correlations.
Δh_{prs}	Parasitic loss correlations.

Δh_{act}	Actual specific enthalpy.
Δh_i	Incidence loss.
Δh_{bld}	Blade loading loss.
Δh_{sf}	Skin friction loss.
Δh_{cl}	Clearance loss.
Δh_{mix}	Mixing loss.
Δh_{vld}	Vaneless diffuser loss.
Δh_{df}	Disk friction loss.
Δh_{rc}	Recirculation loss.
Δh_{lk}	Leakage loss.
Δh_{sf}	Skin friction loss.

Greek letters

α	Absolute flow angle ($chapter_3$), determines the spread of the sigma points around the state and is usually set to a small positive value ($chapter_5$).
β	Relative flow angle or it is used to incorporate prior knowledge of the distribution of the state x
β_i	Relative incidence angle at.
β_{2BI}	Blade angle.
σ	Slip factor.
Θ	Opening at the throat between two blades
ν_k	System noise vector.
ω_k	Measurement noise vector.
λ	Scaling parameter.
κ	Is a secondary scaling parameter which is usually set to 0.
γ	Ratio of specific heat.
ϕ	Entropy function.
ϕ_{ref}	Referential entropy function.
ρ	Static density.
η_c	Compressor efficiency.
λ_{RLS}	Forgetting factor.
η_i	Intake efficiency.
η_r	Ram efficiency.
η_b	Combustion efficiency.
BETA	Is the line drawn parallel to surge line on the compressor map.
ν_{oil}	Viscosity of the oil.
Λ	Degree of reaction of the turbine rotor.

Subscripts

0	Denote initialization.
1	Impeller inlet.
2I	Impeller exit and vaneless diffuser inlet.
2Iabs	Absolute value at impeller exit and vaneless diffuser inlet.

2Irel	Relative value at impeller exit and vaneless diffuser inlet.
2D	Vaneless diffuser exit and vaned diffuser inlet.
2	Vaned diffuser exit.
3	Nozzle inlet.
4N	Nozzle exit and rotor inlet.
4	Rotor exit.
5	Nozzle exit.
a	Axial component or ambient conditions.
abs	Absolute.
k	Actual time.
k+1	Future time.
k-1	Past time.
rel	Relative.
r	Radial component.
w	Whirl component.
map	Referred to compressor map characteristics before correction.
cmap	Abbreviation of correlated compressor map due to the use of factors and deltas.
ss	Steady state.

Superscript

-	Denotes that the estimate is *a priori*.
ˆ	Denotes the parameter estimate.
i	Denote the sigma points.
T	Transpose.

CHAPTER 1
INTRODUCTION

1.1 Justification

Gas turbines are used in power aircraft, trains, ships, electrical generators, and military equipment. The gas turbine engine used by aircrafts requires better attention since a fault in the operation at higher altitudes and velocities would result in catastrophic consequences such as human loses. Early detection of anomalies and their characterization are essential for health management, which includes prognosis of impending failures in critical components and mitigation of their detrimental effects on the engine operation.

An engine condition monitoring system can be realized by estimation of engine component parameter deviation. The accurate in-flight estimation of aircraft engine performance parameters can be identified from on-board engine simulations.

Many researchers [1–6], have studied the application of on-board engine models, based on Kalman filters, to estimate the performance parameters by evaluating response in nominal and off-nominal conditions. Off-nominal engine behavior could be caused by degradation through several mechanisms such as fouling, erosion, oxidation, corrosion, tip clearance (due to the aging process) and abrupt faults like the foreign and domestic object damage [7, 8]. In their investigations they used the linear and non-linear engine models with the help of Kalman filter observers to estimate engine deterioration. Results including strengths and weaknesses of their models were presented.

Advantages in the use of non-linear models against linear models as part of the Kalman filtering implementation, are:

- A single or a few Kalman gain matrices are sufficient to cover the entire engine operating envelope [2].
- The non-linear approach can capture the nonlinearity of aircraft engine operation under the influence of anomalies due to component faults [2].

The present work proposes to develop a reliable SR-30 turbojet engine non-linear model tuned with a Kalman filter technique and suitable for use in anomaly detection, health monitoring and prognosis of SR-30 turbojet engines.

1.2 Objetives

General objective

Development of the on-line estimation of the SR-30 gas turbine performance parameters based on the unscented Kalman filter.

Specific objectives

- Generate the centrifugal compressor map.
- Generate the axial turbine map.
- Develop the nonlinear engine model making use of the component maps.
- Develop the experimental tests in order to validate the engine performance model.
- Develop the estimation of the nonlinear model performance parameters based on Kalman filter technique.

1.3 Literature Review

An extensive literature survey was performed primarily on the SR-30 turbojet engine. Relevant literature on turbofan engines was also included. The results are subdivided into the following sections:

- Component maps.
- Engine performance model.
- Application of Kalman filter for on-line parameter estimation

1.3.1 Component maps

T. Witkowski et al. [9] from the University of Minnesota used the Engineering Equation Solver (EES) software [10] to do a one-dimensional analysis of the SR-30 gas turbine components. Their objective was to independently compute the flow through the radial compressor and through the one-stage axial turbine, at the design point, using only the size dimensions of each component and the initial conditions of the flow entering each component, given by experimental measurements. To achieve their goals, they predicted and estimated the losses through those components and they used the Stodola's equation for slip factor calculation. The results they presented were the velocities and thermodynamic states of the flow at different points within the compressor and the turbine only at a rotational speed of $N = 78000\,rpm$, considered as the design speed. They did not present the validation of results.

Two works which use as a reference the design point analysis, done by T. Witkowski et al. [9], follow. One of them, the work done by May et al. [11] describes the procedure followed to obtain the velocity triangles for the characteristics maps of the SR-30 gas turbine. An iterative calculation in Excel is mentioned, but, the relationships used to achieve this goal are not presented. The resulting maps are plotted using the Smooth-C and Smooth-T commercial softwares [12]. The model was used to monitor health operation of the engine. The authors state that the accuracy of the simulation is strongly dependent on the use of precise engine characteristic performance maps, therefore these are important to achieve accurate development of health monitoring systems. The other work based on reference [9], is that described by O. Léonard et al. [13] from the University of Liège, the authors took into account the analysis on the compressor characteristic curves from Vertessen [14] in which the compressor map was developed from a mean-line analysis and then stored it in the β-lines format to prevent numerical interpolation problems.

The authors did not use a map for the turbine, instead, it was characterized using Stodola's ellipsis equation.

Compressor and turbine losses are considered in the calculation of the velocity triangles. Yoon and Chung [15] tested most of the loss models previously published in the open literature, they found an optimum set of empirical loss models for a reliable performance prediction of centrifugal compressors. In order to improve the prediction of efficiency curves they recommended a modified parasitic loss model. The mean streamline analysis procedure has been utilized to find the best combination of internal as well as parasitic loss models. They found that the predictive performance curves by the proposed optimum set agree fairly well with experimental data for a variety of centrifugal compressors. Reference [11] cites these loss correlations for the calculation of the compressor map.

In radial flow machines like the centrifugal compressors the angular momentum imparted to the flow is reduced by a factor known as the slip factor. Theodor von Backström [16] developed a method that unifies the trusted centrifugal impeller slip factor prediction methods of Busemann [17], Stodola [18], Stanitz [19], Wiesner [20], Eck [21], and Csanady (reported by Dixon [22]) in one equation. The simple analytical method derives the slip velocity in terms of a single relative eddy (SRE) centered on the rotor axis instead of the usual multiple (one per blade passage) eddies. It proposes blade solidity (blade length divided by spacing at rotor exit) as the prime variable determining slip and it contains a constant, F_0, that may be adjusted for specifically constructed families of impellers to improve the accuracy of the prediction.

Various papers describe analytical models of centrifugal compressors different from that used by the SR-30 Gas Turbine. Jiang et al.[23] developed an analytical model for the centrifugal compressor from first principles where energy transfer is being taken into consideration. The dynamic performance, including the losses, is

determined from the compressor geometry. In these papers, the incident and friction losses are modeled, and the other losses such as clearance loss, backward loss and volute loss are considered constants for all off-desing conditions. The authors compared their simulation results with the corresponding results presented in another paper published by Gravdahl [24] who made a similar calculation.

Other methods used to obtain the characteristic curves and the respective tabulated form of the axial compressors maps are described in the following references. Gustafson et al.[25] used data available including a large number of steady state and transient data points collected, to develop, train and test neural networks, in generating the map for a jet engine compressor. The authors expected to reduce the time required to obtain steady-state compressor maps. The learned correlations, by neural networks, were expected to provide information for predicting stall and surge inception. Ghorbanian et al. [26] used different types of neural networks to simulate the performance maps of an axial compressor.

Kurzke [27] used the data read from maps published in the literature to reproduce them through the programs such as Smooth_C and Smooth_T [12]. Kurzke [27], studied the scaling procedure for compressor maps existing in the literature. He applied the statistical analysis to normalize compressor maps and capture its topology with three characteristic numbers like the region where efficiency is highest, the mass flow speed relationship and the shape of the speed line.

There is no compressor map or turbine map available for the SR-30 turbojet engine that has been validated using experimental data. There is only one publication [9] in which a one-dimensional streamline analysis to compute the velocity triangles at the design point were performed. Only one work [11] based on this analysis generate the compressor and turbine characteristic curves using commercial software.

1.3.2 Engine Performance Model

Leonard et al. [13] from the Turbomachinery Group of the University of Liège, built a computer model of the SR-30 engine with the help of EcosimPro′s built-in algorithms (EcosimPro is a commercial software [28]), the characteristic curves of compressor map were obtained using the mean-line analysis. Instead of the turbine map they used Stodola's ellipsis. The authors used an extended Kalman filter to perform the model fitting/tuning at steady state performance, so the experimental data and the model predictions are minimized in the least square sense. They do not show the validation of their results in transient state. May et al. [11] simulated the SR-30 gas turbine using the Gas Turbine Simulation Program (GSP) [29], the model was used to perform the health monitoring of the engine. They performed the one-dimensional modeling of design and off-design engine performance using the characteristic performance curves of the engine. In order to build the maps they used as a guide the geometric data and the approximate design point analysis published by Witkowski et al. [9]. They used the Smooth_C and Smooth_T programs to plot the compressor and turbine maps. The results were validated with experimental data in transient conditions. The figures published by the authors show that the model does not match closely to the experimental data, as they did not use any tuning technique.

Sharma [30], developed a real time simulation program in Matlab/Simulink environment, based on model presented by Auler et al. [31]. The author used component maps, but, did not present how he build them. Sharma validated his model with experimental data and derived the linear model using linear analysis toolbox of Matlab (R-14) [32] at one operating point of the engine. This paper does not show the validation with experimental results, the only validation presented is the validation of linear model with the nonlinear model.

Modeling of steady and transient state was performed for a micro-jet engine by Davison and Birk [33], this aero-thermal model uses generic performance maps for the compressor and turbine which were modified, based on operating data, to represent the components in the engine under study. Unlike other works, the authors examined the effect of ambient humidity on the engine operating point, which is considered when the humidity level is high. They validated their simulation results comparing with the steady-state operating point from the run on a rig test. They concluded that the steady state model is in good agreement with the actual engine data under both healthy and degraded states. In the case of the transient state there is a noticeable difference that requires to be adjusted between the model results and experimental results. The neural network approach was applied to model the single-shaft engine performance, by Lazzaretto and Toffolo [34]. They first constructed compressor and turbine maps from scaling generalized maps, then used a commercial equation solver (EES [10]) to implement the analytical model, they only considered the steady-state performance. As in other works, they used the analytical results to implement the neural networks.

Stationary gas turbine models were studied by Sekhon et al. [35] and Chacartegui et al. [36]. In these publications they developed a nonlinear dynamic model which simulates the transient and steady state of gas turbines under nominal operating conditions. These models are capable of predicting engine performance at load conditions, their results were validated with experimental data.

1.3.3 On-line Engine Estimation

Some gas turbine faults phenomena only appear during transient processes, which could seriously degrade the operability of the engine especially at altitude and during aircraft maneuvers. In recent years much research effort on gas turbine diagnostics and prognostics has focused on the implementation of on-line unsteady state engine health monitoring and engine fault diagnostics. To achieve this goal, it

is of vital importance to construct reliable on-board engine models and determine the fault indices for a specific engine.

Brotherton et al. [1] and Volponi [37] describe the development of a hybrid engine model for a commercial turbofan engine which is the result of fusing two diverse modeling methodologies. A physics-based model approach (with a linear kalman filter as the tuner) and an empirical neural net model approach were used. Among the intended uses for such a model is to enable real-time, on-board tracking of engine module performance changes and engine parameter synthesis to provide enhanced diagnostic and prognostic capabilities. Based on the Constant Gain Extended Kalman Filter (CGEKF) technique, Kobayashi [2] investigated the in-flight estimation of non-measurable performance parameters of a turbofan engine. Kobayashi developed a CGEKF by combining an on-board engine model and a single Kalman gain matrix. This CGEKF can maintain accurate estimation performance when it is applied to aircraft engines at off-nominal conditions. Despite the fact that the Kalman gain was designed at a specific operating point, the CGEKF was stable throughout a typical flight profile. The CGEKF is much more computationally intensive than the linear approach since the nonlinear plant model must be executed in real-time. Kobayashi suggested that to further improve the estimation performance of the CGEKF, a technique to select an optimal set of tuning parameters is desired. The CGEKF filter was first applied in a system identification technique designed by Sugiyama [3] to recognize parameter change in engine components and to estimate unmeasurable variables over whole flight conditions. The effectiveness of the filter was evaluated for a two-spool turbofan engine over full flight envelope. The authors suggested that this approach will be useful as part of engine condition monitoring and engine control.

Many publications in the literature have developed and analyzed the fault detection, isolation and diagnostics based on the implementation of on-line engine

estimation. Dewallef and Léonard [5] implemented the dual estimation of both the state and health parameters of a gas turbine engine during transient sequences based on the robust form of the unscented Kalman filter. This approach is very suitable for on-line engine performance monitoring which minimizes storage and requires limited computational effort. The weaknesses of this method is that physical models are too slow to achieve real time health monitoring. Kobayashi et al. [38], developed a diagnostic system for its application to in-flight fault detection of aircraft engine sensors, based on a hybrid Kalman filter which combines a nonlinear on-board engine model (OBEM) and piecewise linear models. The utilization of the nonlinear OBEM allows the reference health baseline of the diagnostic system to be updated, through a relatively simple process, to the health condition of degraded engines. The performance of this approach was evaluated at multiple steady-state operating points at a cruise condition and also evaluated over minor transients considering a fixed fault threshold, so they recommend the use of an adaptive threshold to improve the overall capability of the in-flight sensor fault detection system.

Borguet et al. [39] investigated the ability of a diagnosis method to process unsteady data rather than steady-state data, with the objective to reduce the time and the efforts spent to obtain a reliable diagnosis. In the test cases they considered, the fault level was constant in time that is unlikely to be the case in an on-board application. This dual filters approach prevents from being applicable to an embarked controller because it is slow to achieve the real time health monitoring. There are other works, in the field of fault diagnostics, presented by Kobayachi and Simon [40] and [41] , they applied a bank of Kalman filters to aircraft gas turbine engine sensor and actuator fault detection and isolation (FDI) in conjunction with the detection of component faults. This approach was applied to a commercial aircraft engine simulation at nominal and aged conditions and its performance was evaluated at cruise operating conditions.

There are also studies who applied unscented Kalman filter (UKF) to parameter estimation and neural network training, they applied this technique to various fields, some of them are presented here. Van der Merwe and Wan [42] developed different techniques based on Kalman filter for parameter estimation and training neural network. Between these techniques are the UKF and other techniques which use derivative-free forms instead of Jacobians or Hessians used by the extended Kalman filter (EKF). They concluded that the square root forms introduced in the filter like UKF have better numerical properties than their non square root forms and provide similar performance relative to EKF.

Choi et al. [43] developed an approach to nonlinear state-space modeling using recurrent multilayer perceptrons (RMLPs) trained with unscented Kalman filter. The UKF offers fast convergence over the RMLP alone, derivative-free computations and easy implementation compared with the EKF. Choi et al. [44] presented a decision feedback equalizer, a recurrent neural network equalizer trained with UKF. Compared to gradient descent learning technique training with UKF has fast convergence and good performance.

Geng [45] trained the nonlinear autoregressive recurrent neural networks with UKF to predict pseudorange corrections for Differential Global Positioning System (DGPS). He concluded that conventional algorithms have difficulties in precisely predicting the DGPS corrections online compared with the proposed recurrent neural networks trained with UKF.

CHAPTER 2
THEORETICAL BACKGROUND

2.1 Turbojet Engine

The first and simplest type of gas turbine is the turbojet. The turbojet engine was first used as a means of aircraft propulsion by Von Ohain (first flight August 27, 1939) and Whittle (first flight May 15, 1941). The "heart" of a turbojet engine and other engine systems is the gas generator. The compressor, combustor, and turbine are the major components of the gas generator which is common not only for turbojet engine, but also for turbofan, turboprop, and turboshaft engines. The purpose of a gas generator is to supply high-temperature and high-pressure gas.

Aircraft gas turbine cycles, as in the case of turbojet, differ from shaft power cycles in that the useful power output is in the form of thrust. The whole of the thrust of the turbojet is generated in propelling nozzles. A second distinguished feature is the need to consider the effect of forward speed and altitude on the performance. It was the beneficial aspect of these parameters, together with a vastly superior power/weight ratio, that enabled the gas turbine to so rapidly replace the reciprocating engine for aircraft propulsion except for low-power light aircraft.

Unlike stationary gas turbines, this type of engine has two main components additional to the gas generator, which are: the intake, and the propelling nozzle. The intake, under static conditions or at very low forward speeds, acts as a nozzle in which the air accelerates relative to the engine. At normal forward speeds, however, the intake performs as a diffuser with the air decelerating and the static pressure rising. The nozzle expands the working fluid to give a high velocity jet before being

discharged to the surroundings. The overall change in the velocity of the gases relative to the engine gives rise to the propulsive force, or thrust.

2.1.1 Brayton cycle

In the Brayton cycle it is assumed an air-standard analysis in which the working fluid is air modeled as an ideal gas. The intake, compressor, turbine, and nozzle processes are assumed isentropic, and the combustor is assumed to operate at constant pressure. The nomenclature of a simple turbojet engine (to be adopted in this thesis) and its correspondence ideal enthalpy-entropy (h-s) diagram of the processes is shown in Figure 2–1.

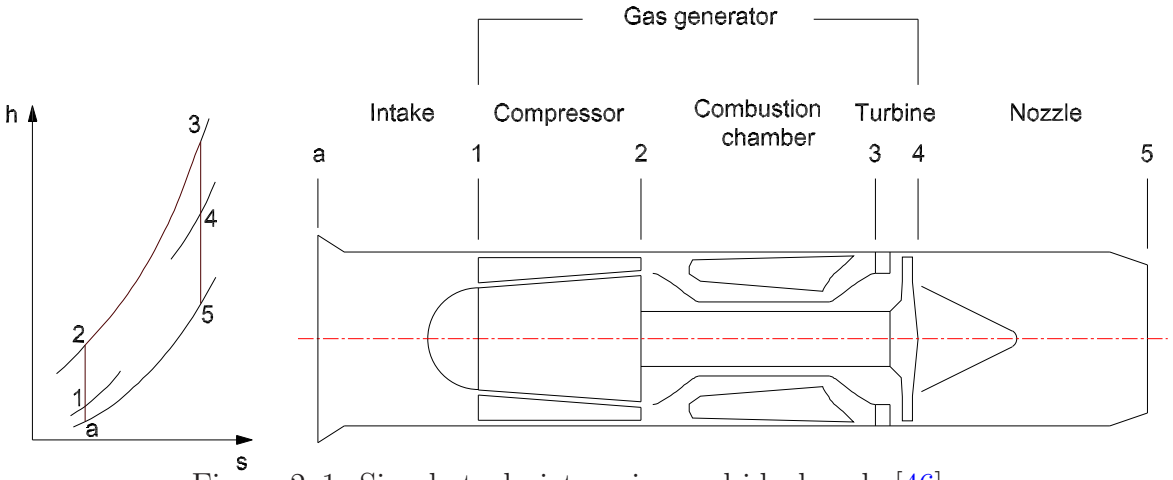

Figure 2–1: Simple turbojet engine and ideal cycle [46].

The processes are as follow [47]:

- Process a-1 shows the pressure rise that occurs in the diffuser as the air decelerates isentropically through this component.
- Process 1-2 is an isentropic compression.
- Process 2-3 is a constant-pressure heat addition.
- Process 3-4 is an isentropic expansion through the turbine during which work is developed.

- Process 4-5 is an isentropic expansion through the nozzle in which the air accelerates and the pressure decreases.

2.1.2 SR-30 Turbojet Engine Description

The SR-30 Turbojet engine is designed and manufactured by Turbine Technologies [48]. The engine is similar in design to powerplants typical of aircraft, marine and rail propulsion systems. It is also comparable to industrial and power generation type gas turbines. The only significance difference from these examples is the size.

Showcasing the internal configuration of the basic turbojet, the SR-30 turbojet engine cutaway in Figure 2–2 facilitates a qualitative understanding of gas turbine fundamentals.

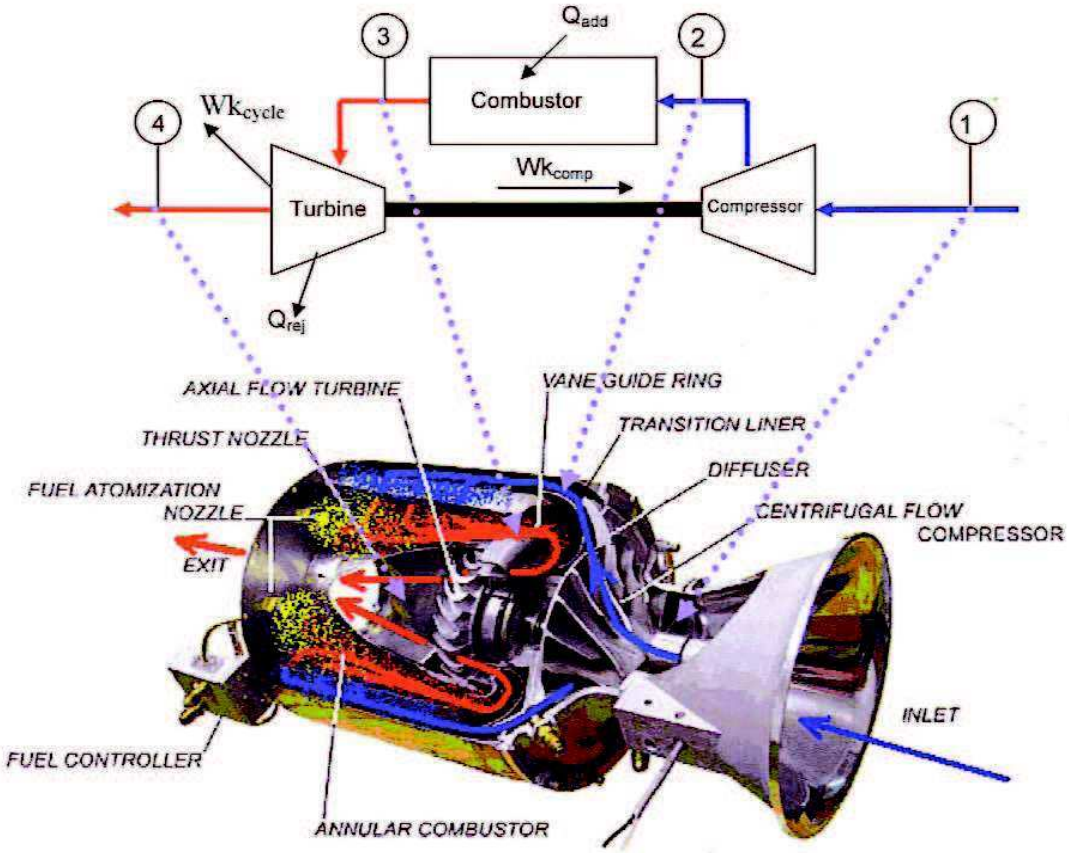

Figure 2–2: SR-30 Turbojet Engine Components and its Schematic of Brayton Cycle [49].

The following sections provide a brief introduction to each of the principal engine components (for more details refer to the operator's manual [49]).

Intake

The intake is the first engine component to encounter the gaseous working fluid (atmospheric air) necessary for the operation of the gas turbine engine. The intake (or inlet bell) of the SR-30 engine is illustrative of a typical subsonic inlet duct in which ambient air is directly routed to the face of the compressor.

Centrifugal Compressor: Impeller

The SR-30 utilizes a centrifugal (radial flow) compressor. The compressor typically rotates anywhere from 50000 to 90000 revolutions per minute (RPM). This high rotational speeds takes inlet air at the impeller hub and centrifugally accelerates it in a radial direction toward the outer circumference of the impeller where it is discharged through the diffuser. The compressor blade geometry and the corresponding aerodynamic and fluid forces resulting from the rotation effects a useful change in the working fluid velocity and pressure.

Centrifugal Compressor: Diffuser

The diffuser (stator) works in conjunction with the impeller to further process the working fluid. The compressor discharge air is directed through the diffuser where the fluid velocity is decreased and the static pressure increased. This discharge air also undergoes a 90 degree change in direction, transitioning from a radial to axial flow (oriented along the length of the engine). The rotating impeller and diffuser working together comprise the compressor stage of the engine and in the Brayton cycle it is represented from state 1 to state 2.

Annular Combustor

High pressure air leaving the diffuser now enters the combustion chamber or combustor where it further increases the internal energy content of the working fluid through combustion of a gaseous fuel and air mixture. The SR-30 engine features

an annular type combustor which is oriented in a reverse flow arrangement with the inlet of the combustor situated at the rear of the engine. Only a small fraction of the available compressor air, known as primary air, and fuel is ignited during the engine start by a high voltage spark type igniter plug. Air in excess of that needed for combustion, termed secondary air, enters through the larger combustor holes and helps to both stabilize and position the combustion flame within the combustor walls and to cool the combustion gases to a value suitable for engine operation. The combustion process is designated from state 2 to state 3.

Fuel Atomization Nozzle

Fuel enters the combustion inlet through six equally spaced fuel atomization nozzles located at the extreme rear of the engine.

Fuel Controller

Fuel is provided to the atomization nozzles via the fuel controller. Engine speed is regulated by controlling the amount of fuel entering the combustor through the fuel atomization nozzles. Fuel is delivered to the controller at constant pressure.

Transition Liner

Hot combustion gases leaving the annular combustor in the reverse direction are turned back 180 degrees by the transition liner to return the flow path to the normal front to back direction.

Axial Flow Turbine: Vane Guide Ring

The vane guide ring (stator) is the first component in the turbine stage. Through the small airfoil blades of the ring, the hot, high pressure combustion gases are accelerated to a high velocity, high energy flow, in such a manner as to produce the most effective reaction against the turbine blades.

Axial Flow Turbine: Rotor

The turbine (rotor) absorbs energy from the accelerating gas flow, coming from the vane guide ring, and converts it into usable mechanical power to drive the

compressor and overcome the mechanical frictions to drive the entire flow process. The turbine stage is represented by the process $3-4$ from the Brayton cycle in Figure 2–2.

Thrust Nozzle

The thrust nozzle is a convergent tube of gradually decreasing cross-section which converts the remaining combustion heat energy into kinetic energy resulting in propulsive thrust at the nozzle exit.

2.2 Centrifugal Compressors

The centrifugal compressors consists essentially of a stationary casing containing a rotating impeller which imparts a high velocity to the air, and a number of fixed diverging passages in which the air is decelerated with a consequent rise in static pressure [46]. Figure 2–3 which is extracted from reference [50] shows the configuration of a centrifugal compressor.

The impeller inlet is called the inducer, or eye, and the outlet the exducer. The impeller has a tip clearance relative to a stationary shroud, and has seals relative to a back plate. The impeller vanes at the exducer may be radial, or for higher efficiency at the expense of frontal area, backswept. In the vaneless space the flow is in free vortex (whirl velocity varies inversely with radius) until the leading edge of the diffuser vanes. On leaving the diffuser the flow will have a high degree of swirl, typically around 50^o, and so usually it flows around a bend into a set of axial straightener vanes before entering the combustion system.

Inlet Guide Vanes

The Inlet Guide Vanes (IGV) gives circumferential velocity to the fluid at the inducer inlet. This function is called prewhirl [51]. The purpose of IGVs is to decrease the relative Mach number at the inducer tip (impeller eye) inlet because

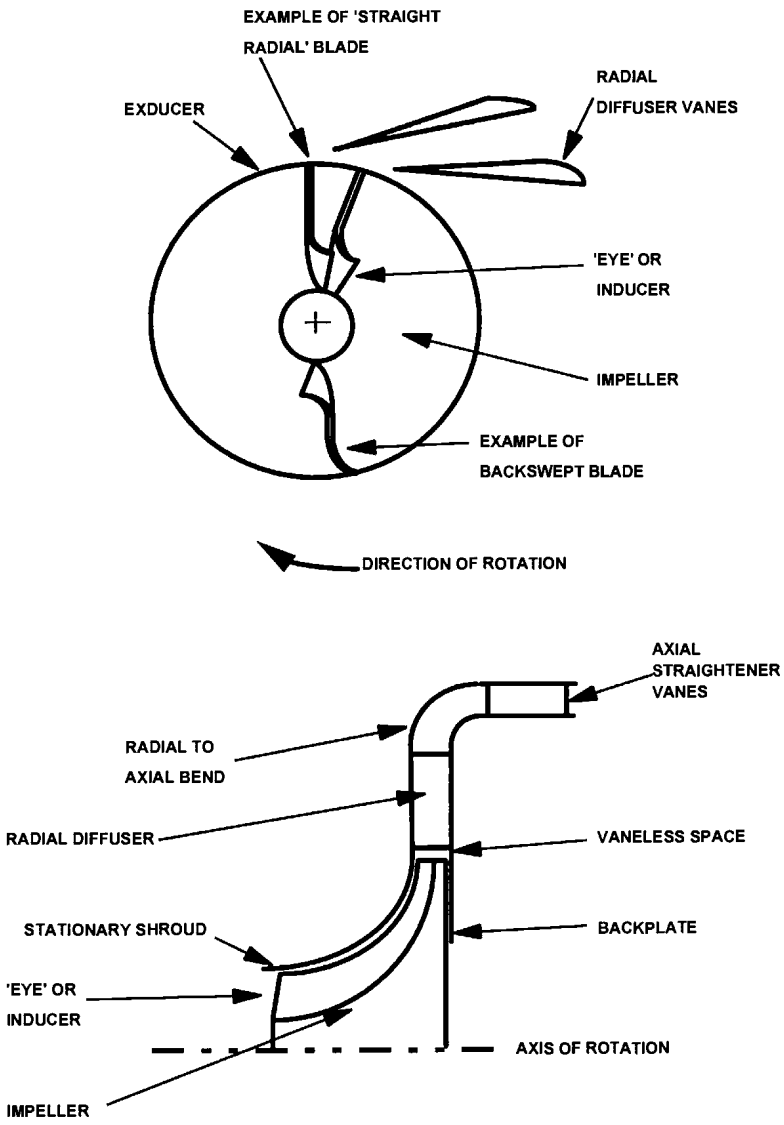

Figure 2–3: Centrifugal compressor configuration.

the highest relative velocity at the inducer inlet is at the tip section. The SR-30 does not have the IGV, so no prewhirl of flow is present.

Slip Factor

Due to its inertia, the air trapped between the impeller vanes is reluctant to move with the impeller. This results in a higher static pressure on the leading face of a vane than the trailing face. It also prevents the air from acquiring a whirl velocity equal to the impeller speed, this effect is known as *slip* (σ) [46]. Various approximate analysis of the flow in an impeller channel have led to formulae for σ.

Centrifugal Compressor Performance

Calculating the performance of a centrifugal compressor in both design and off-design conditions requires a knowledge of various losses encountered in a centrifugal compressor. The losses, which are usually expressed as a loss of heat or enthalpy, are divided into two groups: (1) Losses which occur in the rotor (impeller), (2) and losses encountered in the stator (vaneless diffuser and vaned diffuser).

Rotor losses are divided into the following categories: Incidence loss (Δh_{inc}), disc friction loss (Δh_{df}), Diffusion-blading loss (Δh_{bl}), Clearance loss (Δh_{cl}) and skin friction loss (Δh_{sf}).

The stator losses are: Incidence loss (Δh_{inc}), skin friction loss (Δh_{sf}), wake-mixing loss (Δh_{rc}), and vaneless diffuser loss (Δh_{vdl}).

The theoretical total head available (Δh_{act})) is equal to the head available from the energy equation (Δh_{euler}) plus the head (known as parasitic losses), which is lost because of leakage (Δh_{lk}), disc friction (Δh_{df}), and resulting from any recirculation (Δh_{rc}) of the air back into the rotor from the diffuser. To see the calculations go to the appendix A, and for more information go to reference [15] and [51].

2.3 Axial-flow Turbines

Because the SR-30 turbojet engine uses an axial-flow turbine it is necessary to understand about its performance in order to develop the turbine map.

Ainley and Mathieson (1951) published a method of estimating the performance of an axial flow turbine. In essence the total pressure loss and gas efflux angle for each row of a turbine stage is determined at a single $reference$ diameter and under a wide range of inlet conditions. This reference diameter was taken as the arithmetic mean of the rotor and stator rows inner and outer diameters. Dunham and Came (1970) gathered together details of several improvements to the method of Ainley

and Mathieson which gave better performance prediction for *small* turbines than the original method.

The overall total pressure loss is composed of three parts: (i) profile loss, (ii) secondary loss, and (iii) tip clearance loss.

(i) A **profile loss coefficient** is defined as the loss in stagnation pressure across the blade row or cascade, divided by the difference between stagnation and static pressures at blade outlet. The blade shape and the pressure gradient to which the flow is subjected are major factors in this type of loss. The variation of profile loss coefficient at zero incidence against pitch/chord ratio (s/l) is shown in Fig. 2–4 (extracted from reference [22]) for nozzles and impulse blading at various flow outlet angles. Fig. 2–4 is useful to calculate profile loss for other types of blading intermediate between nozzle blades and impulse blades.

(ii) **The secondary losses** arise from complex three-dimensional flows set up as a result of the end wall boundary layers passing through the cascade. There is substantial evidence that the end wall boundary layers are convected inwards along the suction-surface of the blades as the main flow passes through the blade row, resulting in a serious mal-distribution of the flow, with losses in stagnation pressure often a significant fraction of the total loss.

(iii) **Tip clearance loss** occurs when the blade tip is mechanically free of the shroud casing, and the pressure gradient across the blade thickness induces flow leakage through the clearance space. This flow across the tip causes turbulence, a pressure drop, and interferes with the main stream flow. The equations used to calculate the three loss coefficients, described above, are presented in chapter three.

2.4 Kalman Filter

Theoretically the Kalman filter is an estimator for what is called the linear quadratic problem, which is the problem of estimating the instantaneous state of

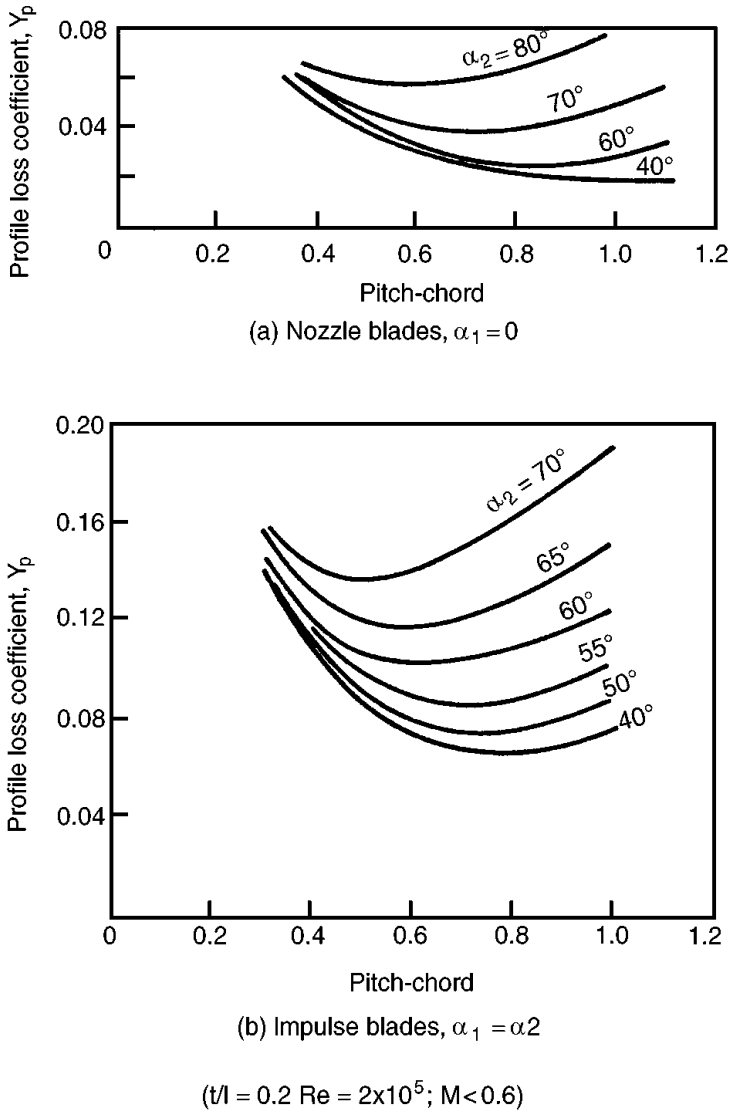

Figure 2–4: Profile loss coefficients of turbine nozzle and impulse blades at zero incidence.

a linear dynamic system perturbed by white noise by using measurements linearly related to the state but corrupted by white noise [52].

Linear filters are used for linear systems. Unfortunately linear systems do not exist. All systems are ultimately nonlinear. However many systems are close enough to linear that linear estimation approaches give satisfactory results. Eventually, we run across a system that does not behave linearly even over a small range of operation, and our linear approaches for estimation no longer give good results.

There is still a lot of room for advances and improvement in nonlinear estimation techniques. However, some nonlinear estimation methods have become (or are becoming) widespread [53]. These techniques include nonlinear extensions of the Kalman filter (EKF), unscented Kalman filter (UKF), and particle filtering.

2.4.1 Unscented Kalman Filter (UKF)

The Unscented Kalman Filter UKF was introduced for the first time by Julier and Uhlmann in 1995 [54], then the same authors demonstrated the potential of UKF as an estimator [55] better than the extended Kalman filter (EKF).

The state distribution, as in the case of extended Kalman filter (EKF) technique, is again represented by Gaussian Random Variables (GRV), but is now specified using a minimal set of carefully chosen sample points. These sample points completely capture the true mean and covariance of the GRV, and when propagated through the true non-linear system, captures the posterior mean and covariance accurately to the 3rd order (Taylor series expansion) for any nonlinearity. (UKF) is a straightforward extension of the Unscented Transformation (UT) to the recursive estimation.

The unscented transformation (UT) is a method for calculating the statistics of a random variable which undergoes a nonlinear transformation.

A simple example is shown in Figure 2–5 for a 2-dimensional system: the left plot shows the true mean and covariance propagation using Monte-Carlo sampling; the center plots show the results using a linearization approach as would be done in the EKF; the right plots show the performance of the UT (note only 5 sigma points are required). The superior performance of the UT is clear. For more details on this topic refer to [42] and [55].

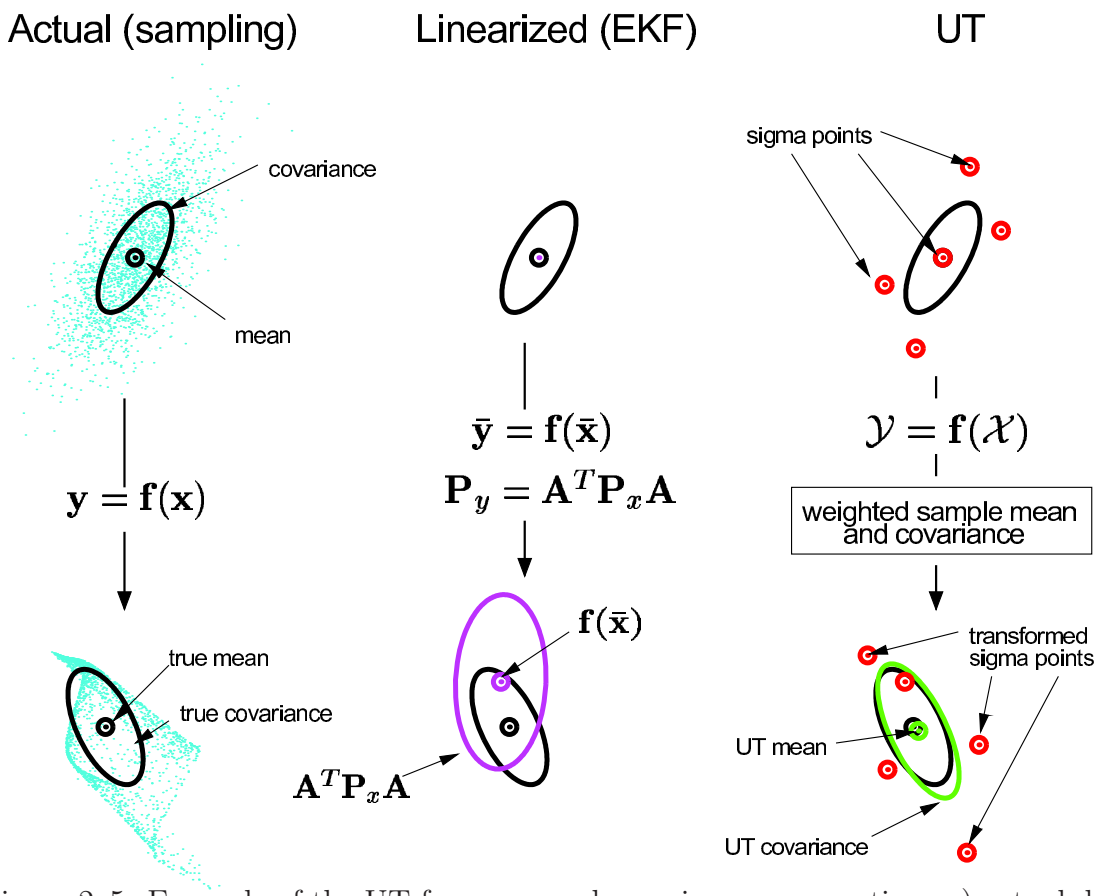

Figure 2–5: Example of the UT for mean and covariance propagation. a) actual, b) first-order linearization, c) UT.

2.4.2 UKF Dual Estimation

Wan and Van der Merwe [42] extended the use of UKF to a broader class of nonlinear estimation problems, including nonlinear system identification, training of neural networks, and dual estimation problems.

For these dual estimation problems it is considered a discrete-time nonlinear dynamic system,

$$x_{k+1} = F(x_k, v_k, w) \tag{2.1}$$

$$y_k = H(x_k, n_k, w) \tag{2.2}$$

The dual estimation problem consists of simultaneously estimating the clean state x_k and the model parameters w from the noisy data y_k (see equation 2.2).

The primary benefit of dual estimation is the ability to temporarily decouple the parameter filter from the state filter as needed. Decoupling can prevent erratic behavior due to poor measurements or initial estimate of the parameter estimation from causing the state filter to diverge.

CHAPTER 3
CHARACTERISTICS MAPS

The performance maps of the turbomachinery components of a jet engine, namely, compressors and turbines, constitute an essential input to overall engine performance models, because of this, an analytical model is presented, in order to obtain the performance maps. The maps are introduced into the engine model through tabulated functions, and interpolation is used for obtaining the values of the dependent parameters (mass flow rate $\dot{m}$, pressure ratio PR, and efficiency η) corresponding to arbitrary values of the independent ones.

3.1 Thermodynamic Properties

The properties of the working fluid in a gas turbine engine have a powerful impact upon its performance. These gas properties will be accounted rigorously in calculations. The working fluid will be considered dry air until the combustor inlet. From the combustor chamber until the engine exit, the working fluid will be the products of combustion from the mixture of dry air and kerosene (fuel). All gases employed as the working fluid in gas turbine engines, except for water vapor, may be considered as real gases [22], hence, the present work will assume the working fluid as a real gas. Also, the analysis presented in this work assumes that mass fraction of water vapor, in the combination of ambient humidity and product of combustion, is less than 10%, therefore it will be neglected the content of water due to humidity [22].

3.1.1 Dry air

Dry air is a mixture of two main component gases (nitrogen and oxygen) together with traces of a number of other gases. The composition of dry air is presented in table 3–1 obtained from Walsh and Fletcher [50].

Table 3–1: Composition of dry air.

	By mole or volume (%)	By mass (%)
Nitrogen (N_2)	78.08	75.52
Oxygen (O_2)	20.95	23.14
Argon (Ar)	0.93	1.28
Carbon dioxide	0.03	0.05
Neon	0.002	0.001

There are also trace amounts of helium, methane, krypton, hydrogen, nitrous oxide and xenon. These are negligible for gas turbine performance purposes.

Critical temperatures and pressures for dry air are $-140.2\,^{\circ}\mathrm{C}$ and 37.2atm (3769.3 kPa).

3.1.2 Combustion products

When a hydrocarbon fuel is burnt in air, the products of combustion change the composition significantly. The degree of change in air composition depends both on fuel air ratio and fuel chemistry.

Distilled liquid fuels such as kerosene has relatively fixed chemistry. Properties of their combustion products can be evaluated versus fuel air ratio and temperature using unique formulae, with the fuel chemistry built-in [50].

Dissociation of combustion products is not taken into account because the maximum temperature is less than $1500\,^{\circ}\mathrm{K}$, therefore, the specific heat at constant pressure (c_p) and heat capacity ratio (γ) do not depend on pressure.

3.1.3 Correlations

The working fluid through all the engine will be considered as real gases due to the following considerations:

- As mentioned above the humidity will be neglected.
- The temperature of dry air is higher than its critical temperature.
- The pressure of dry air is less than its critical pressure.

The correlations which are presented below are taken from reference [50].

- Gas constant, (R).

  The gas constant for dry air is 287.05 J/kgK and the gas constant for products of combustion in dry air for kerosene is:

$$R = 287.05 - 0.00990 * FAR + 10^{-7} * FAR^2; \qquad \text{J/kgK} \tag{3.1}$$

- Specific heat at constant pressure, c_p; (kJ/kg K).

  Dry air, $c_p = f_{c_p}(T)$:

$$\begin{aligned} c_p = A_0 + A_1 * TZ + A_2 * TZ^2 + A_3 * TZ^3 + A_4 * TZ^4 \\ + A_5 * TZ^5 + A_6 * TZ^6 + A_7 * TZ^7 + A_8 * TZ^8 \end{aligned} \tag{3.2}$$

  Where $TZ = T/1000$, T is the static temperature and the values for constants are as follow:

$$\begin{aligned} A_0 &= 0.992313 & A_6 &= -3.234725 \\ A_1 &= 0.236688 & A_7 &= 0.794571 \\ A_2 &= -1.852148 & A_8 &= -0.081873 \\ A_3 &= 6.083152 & A_9 &= 0.422178 \\ A_4 &= -8.893933 & A_{10} &= 0.001053 \\ A_5 &= 7.097112 \end{aligned}$$

Combustion products of kerosene or diesel in dry air, $c_p = f_{c_p}(T, FAR)$:

$$\begin{aligned} c_p = {} & A_0 + A_1 * TZ + A_2 * TZ^2 + A_3 * TZ^3 + A_4 * TZ^4 \\ & + A_5 * TZ^5 + A_6 * TZ^6 + A_7 * TZ^7 + A_8 * TZ^8 \\ & + \frac{FAR}{1 + FAR} * [B_0 + B_1 * TZ + B_2 * TZ^2 + B_3 * TZ^3 \\ & + B_4 * TZ^4 + B_5 * TZ^5 + B_6 * TZ^6 + B_7 * TZ^7] \end{aligned} \tag{3.3}$$

Where $TZ = T/1000$, T is the static temperature, $A_0 - A_8$ are the values for dry air and the values for constants $B_0 - B_9$ are shown below.

$$\begin{aligned} B_0 &= -0.718874 & B_5 &= 3.081778 \\ B_1 &= 8.747481 & B_6 &= -0.361112 \\ B_2 &= -15.863157 & B_7 &= -0.003919 \\ B_3 &= 17.254096 & B_8 &= 0.0555930 \\ B_4 &= -10.233795 & B_9 &= -0.0016079 \end{aligned}$$

- Ratio of specific heats, (γ).

$$\gamma = \frac{c_p}{c_p - R} \tag{3.4}$$

- Specific enthalpy, $h = h_{ref} + \int_{T_{ref}}^{T} c_p dT$; (MJ/kg).

For dry air, $h = f_h(T)$:

$$\begin{aligned} h = {} & A_0 * TZ + \frac{A_1}{2} * TZ^2 + \frac{A_2}{3} * TZ^3 + \frac{A_3}{4} * TZ^4 \\ & + \frac{A_4}{5} * TZ^5 + \frac{A_5}{6} * TZ^6 + \frac{A_6}{7} * TZ^7 + \frac{A_7}{8} * TZ^8 \\ & + \frac{A_8}{9} * TZ^9 + A9 \end{aligned} \tag{3.5}$$

For combustion products of kerosene or diesel in dry air, $h = f_h(T, FAR)$:

$$\begin{aligned} h = {} & A_0 * TZ + \frac{A_1}{2} * TZ^2 + \frac{A_2}{3} * TZ^3 + \frac{A_3}{4} * TZ^4 \\ & + \frac{A_4}{5} * TZ^5 + \frac{A_5}{6} * TZ^6 + \frac{A_6}{7} * TZ^7 + \frac{A_7}{8} * TZ^8 \\ & + \frac{A_8}{9} * TZ^9 + A9 + \frac{FAR}{1+FAR}[B_0 * TZ + \frac{B_1}{2} * TZ^2 + \frac{B_2}{3} * TZ^3 \\ & + \frac{B_3}{4} * TZ^4 + \frac{B_4}{5} * TZ^5 + \frac{B_5}{6} * TZ^6 + \frac{B_6}{7} * TZ^7 + B_8] \end{aligned} \tag{3.6}$$

Where for each cases, $TZ = T/1000$ and the constants are as per equation 3.2 and 3.3.

- Entropy function, $\phi = \phi_{ref} + \int_{T_{ref}}^{T} \frac{c_p}{T} dT$; (kJ/kgK).

For dry air, $\phi = f_\phi(T)$:

$$\begin{aligned} \phi = {} & A_0 * ln(TZ) + A_1 * TZ + \frac{A_2}{2} * TZ^2 + \frac{A_3}{3} * TZ^3 \\ & + \frac{A_4}{4} * TZ^4 + \frac{A_5}{5} * TZ^5 + \frac{A_6}{6} * TZ^6 + \frac{A_7}{7} * TZ^7 \\ & + \frac{A_8}{8} * TZ^8 + A_{10} \end{aligned} \tag{3.7}$$

For combustion products of kerosene or diesel in dry air, $\phi = f_\phi(T, FAR)$:

$$\begin{aligned} \phi = {} & A_0 * ln(TZ) + A_1 * TZ + \frac{A_2}{2} * TZ^2 + \frac{A_3}{3} * TZ^3 \\ & + \frac{A_4}{4} * TZ^4 + \frac{A_5}{5} * TZ^5 + \frac{A_6}{6} * TZ^6 + \frac{A_7}{7} * TZ^7 \\ & + \frac{A_8}{8} * TZ^8 + A_{10} + \frac{FAR}{1+FAR} * [B_0 * ln(T_2) + B_1 * TZ \\ & + \frac{B_2}{2} * TZ^2 + \frac{B_3}{3} * TZ^3 + \frac{B_4}{4} * TZ^4 + \frac{B_5}{5} * TZ^5 \\ & + \frac{B_6}{6} * TZ^6 + \frac{B_7}{7} * TZ^7 + B_9] \end{aligned} \tag{3.8}$$

where $TZ = T/1000$ and T is the static temperature.

3.2 Compressor Map

Performance maps of turbomachinery components are built by manufacturers, if they are not available, these maps must be generated using a model based on its design point analysis. Therefore, a design point analysis is required for the SR-30 in

order to build the analytical model of performance maps of the compressor and turbine. Witkowski et al. [9] published a paper which contains blade geometry and an approximate design point analysis, so for each component, the design point velocity triangles are drawn and then their results were published. The aim of this section is to verify those results. The SR-30 is equipped with a centrifugal compressor with both a vaneless and vaned diffuser.

3.2.1 Preliminary considerations

The nomenclature of stations used in the analysis, based on fluid mechanics and thermodynamics, for the centrifugal compressor which is shown in Figure 3–1, is described as follow:

- Entrance to impeller: 1.
- Exit from impeller - entrance to vaneless diffuser: 2i
- Exit from vaneless diffuser - entrance to vaned diffuser: 2d
- Exit from vaned diffuser: 2

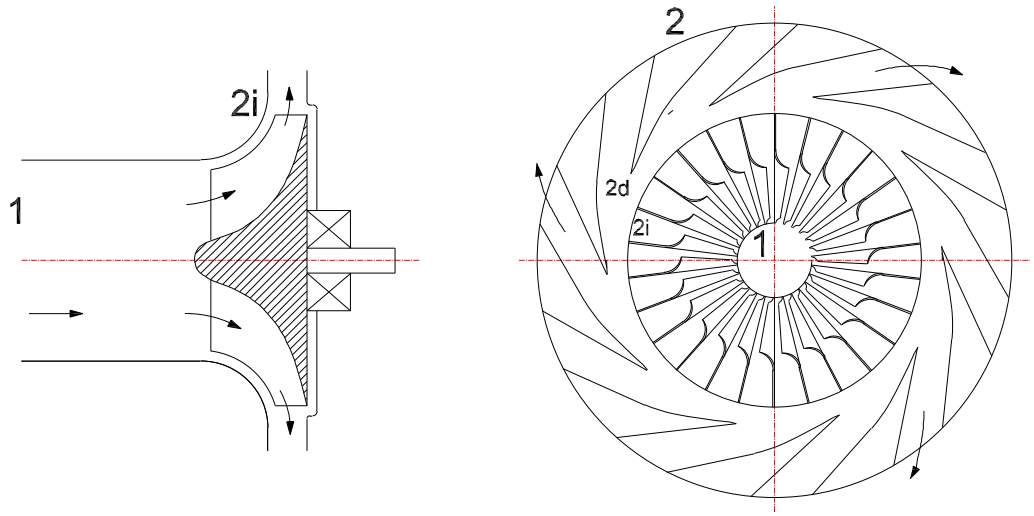

Figure 3–1: Nomenclature of stations in the centrifugal compressor.

The analysis for the flow through the compressor is based in the one-dimensional steady flow analysis, in which according to Dixon [22], the velocity and density are

regarded as uniform across each section of a duct or passage. Considering the conservation of mass flow rate through the compressor:

$$\dot{m} = \rho_1 C_{a1} A_1 = \rho_{2i} C_{a2i} A_{2i} = \rho_{2d} C_{a2d} A_{2d} = \rho_2 C_2 A_2; \qquad \text{kg/s} \qquad (3.9)$$

where ρ_1, C_{a1}, A_1 are the static density, velocity of the air flow and the area at station "1"; ρ_{2i}, C_{a2i}, A_{2i} are the static density, velocity of the air flow and the area at station "2i"; ρ_{2d}, C_{a2d}, A_{2d} are the static density, velocity of the air flow and the area at station "2d"; and ρ_2, C_2, A_2 are the static density, velocity of the air flow and the area at station "2".

The Mollier diagram shown in Figure 3–2, for the centrifugal compressor is used to obtain the thermodynamics relations required for the analysis.

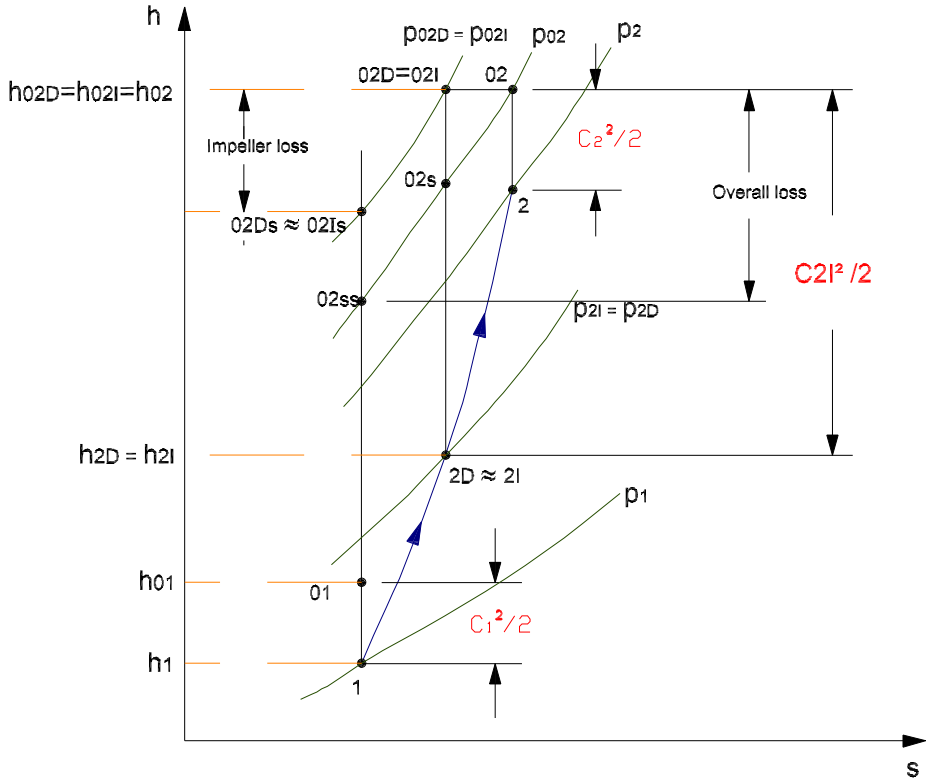

Figure 3–2: Mollier diagram for the complete centrifugal compressor stage.

Compressor maps will be developed from data points obtained from the calculations of the next four performance parameters:

- Mass flow rate (dry air) $\dot{m}$.

- Rotational speed N.
- Pressure ratio PR_c.
- Isentropic efficiency η_c.

The first two parameters mentioned above will be the input variables used to find the other two parameters:

$$PR_c = f_{PR_c}(\dot{m}, N)$$

$$\eta_c = f_{\eta_c}(\dot{m}, N)$$

The operating conditions used to develop the design point velocity triangles are according to Witkowski et al. [9]:

$$\dot{m} = 0.294 \text{ : Air mass flow (kg/s)}$$

$$N = 78000 \text{ : Rotational speed (rpm)}$$

The off-design velocity triangles are constructed taking into account the next range of values for the operating conditions:

$$\dot{m} = 0 - 0.5; \qquad \text{kg/s}$$

$$N = 50000 - 90000; \qquad \text{rpm}$$

3.2.2 Data

The geometric data and input conditions from the centrifugal compressor of the SR-30 turbojet engine are required to begin the calculations, this information has been published by Witkowski et al. [9], as shown in table 3–2. Where C_{W1} is the pre-swirl of the flow. Furthermore the properties of dry air, which were described in the previous section are required as well.

The data of the centrifugal compressor, shown in table 3–2, was fixed at the design point performance, now the compressor map may be generated to define its performance under all off-design conditions. Next, calculations are performed to

Table 3–2: Dimensions of centrifugal compressor and inlet conditions of the flow entering the impeller.

Dimensions		**Inlet conditions**
Impeller	**Diffuser**	
- Eye root diameter: $D_r = 20.6\,mm$	- Radial width of vaneless diffuser: $\omega_r = 4.76\,mm$	$p_{01} = 100\,kPa$
- Eye tip diameter: $D_t = 60.3\,mm$	- Radius at entrance of vaned diffuser: $r_{2D} = 55.76\,mm$	$T_{01} = 300\,K$
- Impeller tip diameter: $D_2 = 102\,mm$	- Radius at exit of vaned diffuser: $r_2 = 78\,mm$	
- Axial width at exit of impeller: $b_{2I} = 6.35\,mm$	- Diffuser vane length: $L = 60\,mm$	$C_{W1} = 0$
- 9 primary blades and 9 secondary blades: $n_b = 24$		(No pre-swirl of the flow entering the impeller)
- Tip clearance: $\varepsilon = 0.5\,mm$		
- $\beta_{1b} = -57\,deg$ and $\beta_{2Ib} = -20\,deg$		

obtain the velocity diagrams for flow through the stage of the centrifugal compressor.

3.2.3 Velocity triangle at impeller inlet or station "1"

The velocity triangle was drawn at the impeller inlet considering the assumption imposed. The assumption is that pre-whirl is not considered because the experimental gas turbine module does not have the fixed inlet guide vane (see figure 3–3 a) that reduces the relative velocity, and hence the Mach number at the intake. So $C_{W1} = 0$ (as shown in figure 3–3 b). Then,

$$C_1 = C_{a1} \tag{3.10}$$

At the impeller inlet (known also as eye or inducer) there are many velocity triangles so the average of velocity triangles are taken that correspond to mean radius between the eye root radius and the eye tip radius, as it is shown in Figure 3–5.

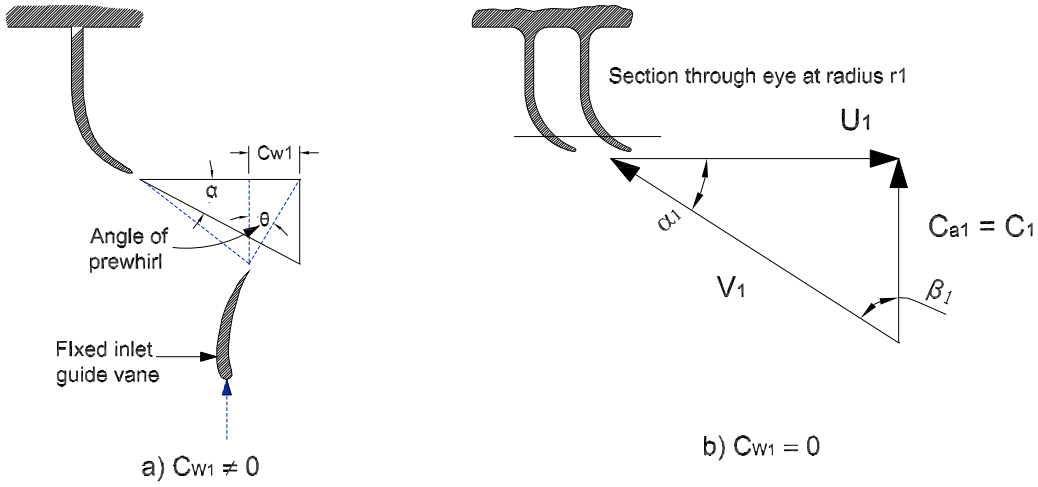

Figure 3–3: Velocity diagram for flow at station 1.

The effective diameter is defined according to:

$$D_1 = \frac{1}{2}\left(D_t^2 + D_r^2\right); \qquad mm \tag{3.11}$$

where D_t is the diameter at the impeller eye tip and D_r is the diameter at the impeller eye root.

The mean tangential speed at the inducer can be calculated as:

$$U_1 = \frac{\pi D_1 N}{60 * 10^3}; \qquad \text{m/s} \tag{3.12}$$

Also we can find the velocities at impeller tip and at impeller root, as follow:

$$U_t = \frac{\pi D_t N}{60 * 10^3}; \qquad \text{m/s}$$
$$U_r = \frac{\pi D_r N}{60 * 10^3}; \qquad \text{m/s}$$

The annulus area of impeller eye is:

$$A_1 = 10^{-6} * \frac{\pi(D_t^2 - D_r^2)}{4}; \qquad m^2 \tag{3.13}$$

To calculate the axial component of the absolute velocity C_{a1}, a trial and error process will be performed. Figure 3–4 shows the iterative procedure followed

to obtain the parameters at compressor inlet or station "1", according to this flow diagram, the density is calculated on the basis of the known stagnation temperature and pressure. Then from the continuity equation an an initial estimate of the axial velocity C_{a1} is obtained. With this value and with the help of thermodynamic relations from the Mollier diagram, the density is recalculated, and the actual velocity determined from the continuity equation. If the assumed and calculated velocities do not agree it is necessary to iterate until agrement is reached.

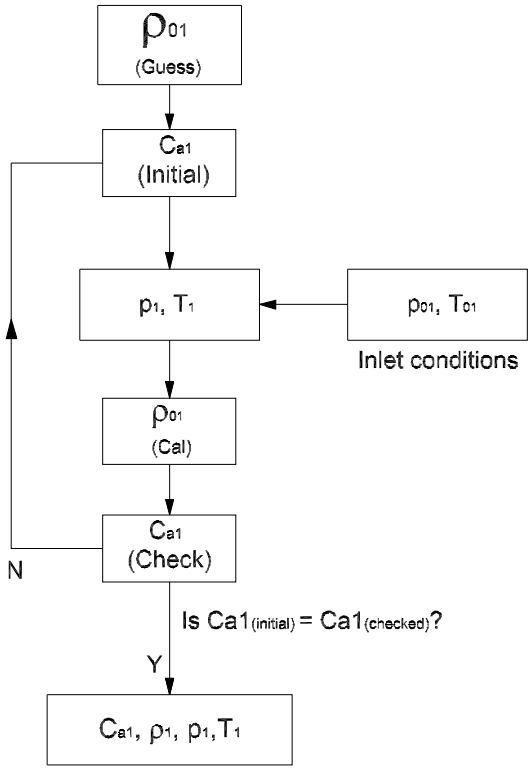

Figure 3–4: Flow diagram of the iterative procedure for obtaining parameters at station "1"

Then equations needed to calculate the above described quantities are as follow:

- Static enthalpy h_1:

$$h_{01} = f_h(T_{01}); \qquad \mathrm{J/kg\,K} \tag{3.14}$$

$$h_1 = h_{01} - \frac{1}{2}C_1^2; \qquad \mathrm{J/kg\,K} \tag{3.15}$$

- Static temperature T_1:

$$T_1 = f_{T_1}(h_1); \qquad \text{K} \tag{3.16}$$

- Static pressure p_1:

$$p_1 = \frac{p_{01}}{e^{\frac{\phi_{01}-\phi_1}{R}}}; \qquad \text{kPa} \tag{3.17}$$

Where $\phi_{01} = f_\phi(T_{01})$ and $\phi_1 = f_\phi(T_1)$.

- Density ρ_1 and axial velocity C_{a1}:

$$\rho_1 = 10^3 * \frac{p_1}{R\,T_1}; \qquad kg/m^3 \tag{3.18}$$

$$C_{a1} = \frac{\dot{m}}{\rho_1\,A_1}; \qquad \text{m/s} \tag{3.19}$$

where equation 3.18 is the equation of state for a perfect gas and 10^3 is a conversion factor.

- Additional calculations:

$$V_1 = \sqrt{C_1^2 + U_1^2}; \qquad \text{m/s} \tag{3.20}$$

$$\beta_1 = \arctan\left(\frac{U_1}{C_1}\right) \tag{3.21}$$

$$\beta_i = \beta_{1b} - \beta_1 \tag{3.22}$$

$$M_{1abs} = \frac{C_1}{\sqrt{\gamma\,R\,T_1}} \tag{3.23}$$

3.2.4 Velocity triangle at impeller exit or station "$2I$"

As shown in the figure 3–5, the air leaves the impeller tip with an absolute velocity C_{2I}, it will have a tangential or whirl component C_{w2I} and a small radial component C_{r2I}. Under ideal conditions the whirl component will be equal to the impeller tip speed U_{2I}. Due to the relative eddies in the impeller blade passage the impeller exit flow angle differs from the impeller exit blade angle; a measure of deviation can be calculated using the concept of a slip factor.

There are many correlations about the slip factor. Von Backström [16] describes a method that unifies the centrifugal impeller slip factor prediction methods of Busemann [17], Stodola [18], Stanitz [19], Wiesner [20], Eck [21], and Csanady (reported by Dixon [22]) in one equation that will be used in this work. This equation is:

$$\sigma = 1 - \frac{1}{1 + F_0\left(\frac{l}{Se}\right)(cos\beta_{2BI})^{0.5}}, \tag{3.24}$$

where F_0 is a constant which its value was adjusted to improve the accuracy of the prediction, β_{2BI} is the blade angle at impeller exit, $RR = \frac{r_i}{r_e}$ is the radius ratio, $\frac{l}{S_e} = \frac{(1-RR)n_b}{2\pi cos\beta_{2BI}}$ is the blade row solidity and n_b is the number of blades.

The area at impeller exit A_{2I} and the blade speed U_{2I} are:

$$A_{2I} = 10^{-6} * \pi D_{2I} b_{2I}; \qquad m^2 \tag{3.25}$$

$$U_{2I} = \frac{\pi D_{2I} N}{60 * 10^3}; \qquad \text{m/s} \tag{3.26}$$

The whirl component of absolute velocity C_{w2I} as a function of the slip factor and the blade tangential speed is calculated, as follow:

$$C_{w2I} = \sigma U_{2I}; \qquad \text{m/s} \tag{3.27}$$

Some designers consider the value of the radial component C_{r2I} the same as the inlet axial velocity C_{a1} [46], but in the current model is considered the initial guess, and the final value of the radial component is determined following the method of iteration shown in the Figure 3–6.

The absolute velocity at impeller exit is:

$$C_{2I} = \sqrt{C_{w2I}^2 + C_{r2I}^2}; \qquad \text{m/s} \tag{3.28}$$

From the Mollier diagram (figure 3–2) and the assumption of pressure ratio PR_{2I} and η_{2I} at station "2i", thermodynamic relations to find p_{02I}, p_{2I}, T_{02I} and

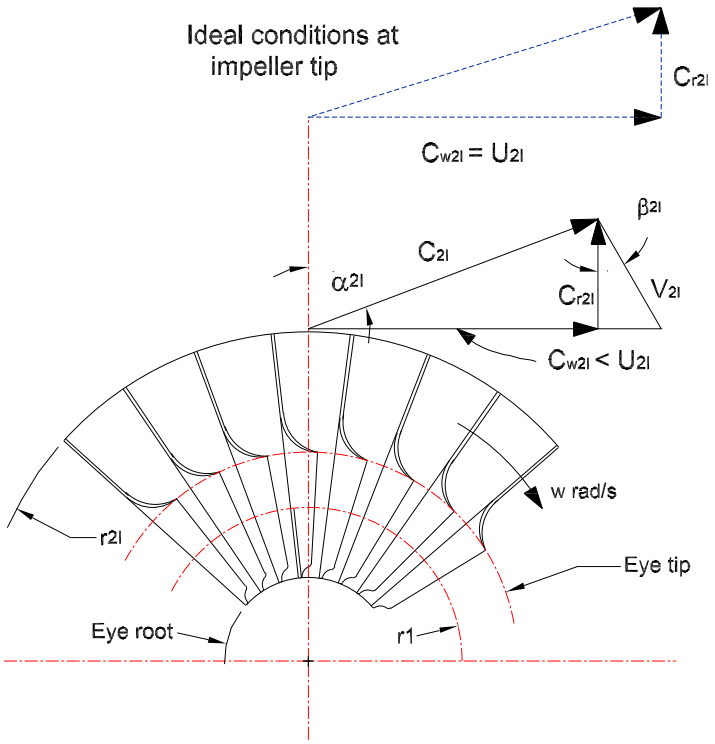

Figure 3–5: Nomenclature at station "2I".

T_{2I} may be obtained:

$$\phi_{01} = f_{\phi}(T_{01}); \qquad \text{J/kg K} \tag{3.29}$$

$$p_{02I} = p_{01} * PR_{2I}; \qquad \text{kPa} \tag{3.30}$$

once p_{2I} is obtained, it is possible to find ϕ_{02Is} from the isentropic process:

$$\phi_{02Is} = \phi_{01} + R\,ln\left(\frac{p_{02I}}{p_{01}}\right); \qquad \text{J/kg K} \tag{3.31}$$

T_{02Is} is obtained from the inverse of the equation 3.7,

$$T_{02Is} = f_T(\phi_{02Is}); \qquad \text{K} \tag{3.32}$$

h_{01} and h_{02Is} are obtained from equation 3.5,

$$h_{01} = f_h(T_{01}); \qquad \text{J/kg K} \tag{3.33}$$

$$h_{02Is} = f_h(T_{02Is}); \qquad \text{J/kg K} \tag{3.34}$$

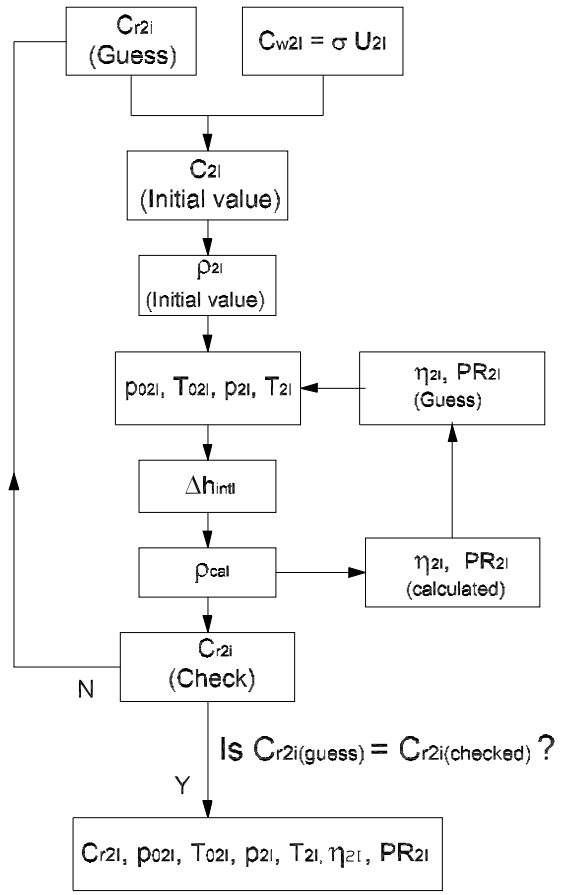

Figure 3–6: Flow diagram of the iterative procedure for obtaining parameters at station "2I".

with the values calculated above, T_{02I} is obtained,

$$h_{02I} = h_{01} + \frac{h_{02Is} - h_{01}}{\eta_{2I}}; \qquad \text{J/kg K} \qquad (3.35)$$

$$T_{02I} = f_T(h_{02I}); \qquad \text{K} \qquad (3.36)$$

then T_{2I} is calculated from the following relations:

$$\phi_{02I} = f_\phi(T_{02I}); \qquad \text{J/kg K} \qquad (3.37)$$

$$h_{2I} = h_{02I} - \frac{1}{2}C_{2I}^2; \qquad \text{J/kg K} \qquad (3.38)$$

$$T_{2I} = f_T(h_{2I}); \qquad \text{K} \qquad (3.39)$$

and p_{2I} is derived from the isentropic process equation:

$$p_{2I} = \frac{p_{02I}}{e^{\frac{\phi_{02I}-\phi_{2I}}{R}}}; \qquad \text{kPa} \tag{3.40}$$

The density and the radial component of absolute velocity calculated are:

$$\rho_{2I} = 10^3 * \frac{p_{2I}}{R\,T_{2I}}; \qquad kg/m^3 \tag{3.41}$$

$$C_{r2I} = \frac{\dot{m}}{\rho_{2I}\,A_{2I}}; \qquad \text{m/s} \tag{3.42}$$

Additional calculations:

$$V_{2I} = \sqrt{C_{r2I}^2 + (U_{2I} - C_{w2I})^2}; \qquad \text{m/s} \tag{3.43}$$

$$M_{2Iabs} = \frac{C_{2I}}{\sqrt{\gamma\,R\,T_{2I}}} \tag{3.44}$$

$$M_{2Irel} = \frac{V_{2I}}{\sqrt{\gamma\,R\,T_{2I}}} \tag{3.45}$$

$$\alpha_{2I} = \arctan(\frac{C_{w2I}}{C_{r2I}}) \tag{3.46}$$

$$\beta_{2I} = \arctan(\frac{U_{2I} - C_{w2I}}{C_{r2I}}) \tag{3.47}$$

The performance parameters are also affected by the losses that occur inside the compressor. The correlations used for the compressor losses were taken from references [15] and [23].

The calculated pressure ratio and isentropic efficiency are obtained from equations obtained from Oh et al. [15]:

$$PR_{2I} = \left[\left(\frac{\Delta h_{euler} - \sum \Delta h_{intI}}{c_p\,T_{01}}\right) + 1\right]^{\gamma/(\gamma-1)} \tag{3.48}$$

$$\eta_{2I} = \frac{\Delta h_{euler} - \sum \Delta h_{intI}}{\Delta h_{act}} \tag{3.49}$$

where:

$$\Delta h_{act} = \Delta h_{euler} + \Delta h_{prs}; \qquad \text{J/kg} \qquad (3.50)$$

$$\Delta h_{euler} = \sigma\, U_2^2; \qquad \text{J/kg} \qquad (3.51)$$

$$\sum \Delta h_{intI} = \Delta h_{iI} + \Delta h_{bld} + \Delta h_{sfI} + \Delta h_{cl}; \qquad \text{J/kg} \qquad (3.52)$$

$$\sum \Delta h_{prs} = \Delta h_{df} + \Delta h_{rc} + \Delta h_{lk}; \qquad \text{J/kg} \qquad (3.53)$$

3.2.5 Velocity triangle at diffuser inlet or station "$2D$"

This station will have only the absolute velocity and its components; the relative velocity does not exist because there is no element in motion. To determine the whirl component at the vaneless diffuser exit C_{w2D} , we can consider the conservation of angular momentum within it, $C_{w2D}\, r_{2D} = C_{w2I}\, r_{2I}$, so:

$$C_{w2D} = \frac{C_{w2I}\, r_{2I}}{r_{2D}}; \qquad \text{m/s} \qquad (3.54)$$

Figure 3–7 shows the nomenclature used for calculations in the vaneless diffuser and vaned diffuser. Similarly at station "2I", the area and absolute velocity to consider are obtained from:

$$A_{2D} = 2\pi\, r_{2D}\, b_{2D} * 10^{-6}; \qquad m^2 \qquad (3.55)$$

$$C_{2D} = \sqrt{C_{r2D}^2 + C_{w2D}^2}; \qquad \text{m/s} \qquad (3.56)$$

The iteration method followed at station "2I" is applied at this station with the modifications presented in figure 3–8. The thermodynamic relations are extracted from the Mollier Diagram (3–2).

Bernoulli's equation, applied to compressible flow through the vaneless diffuser, is expressed as:

$$h_{02I} + \frac{1}{2} v_{02I}^2 = h_{02D} + \frac{1}{2} v_{02D}^2 \qquad (3.57)$$

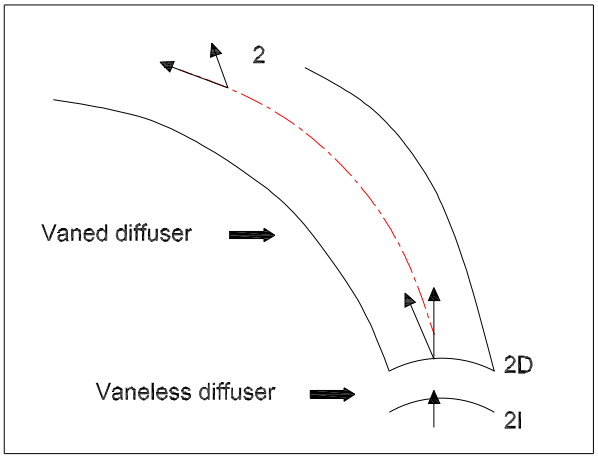

Figure 3–7: Diffuser velocity diagram.

No further energy is supplied to the air after it leaves the impeller, so that neglecting the effect of friction, the angular momentum must be constant [46]. The above means that no work is done in the vaneless diffuser and the process is adiabatic. Then, from reducing the equation 3.57, considering the assumptions described before, the following relation is obtained:

$$h_{02I} = h_{02D} \tag{3.58}$$

The pressure ratio and isentropic efficiency will be calculated in the same way as in the last station:

$$PR_{2D} = \left[\left(\frac{\Delta h_{euler} - \sum \Delta h_{intVD}}{c_p \, T_{01}} \right) + 1 \right]^{\gamma/(\gamma-1)} \tag{3.59}$$

$$\eta_{2D} = \frac{\Delta h_{euler} - \sum \Delta h_{intVD}}{\Delta h_{act}} \tag{3.60}$$

where we have to consider the losses in the impeller and the vaneless diffuser, as follows:

$$\sum \Delta h_{intVD} = \sum \Delta h_{intI} + \Delta h_{vld}; \qquad \text{J/kg} \tag{3.61}$$

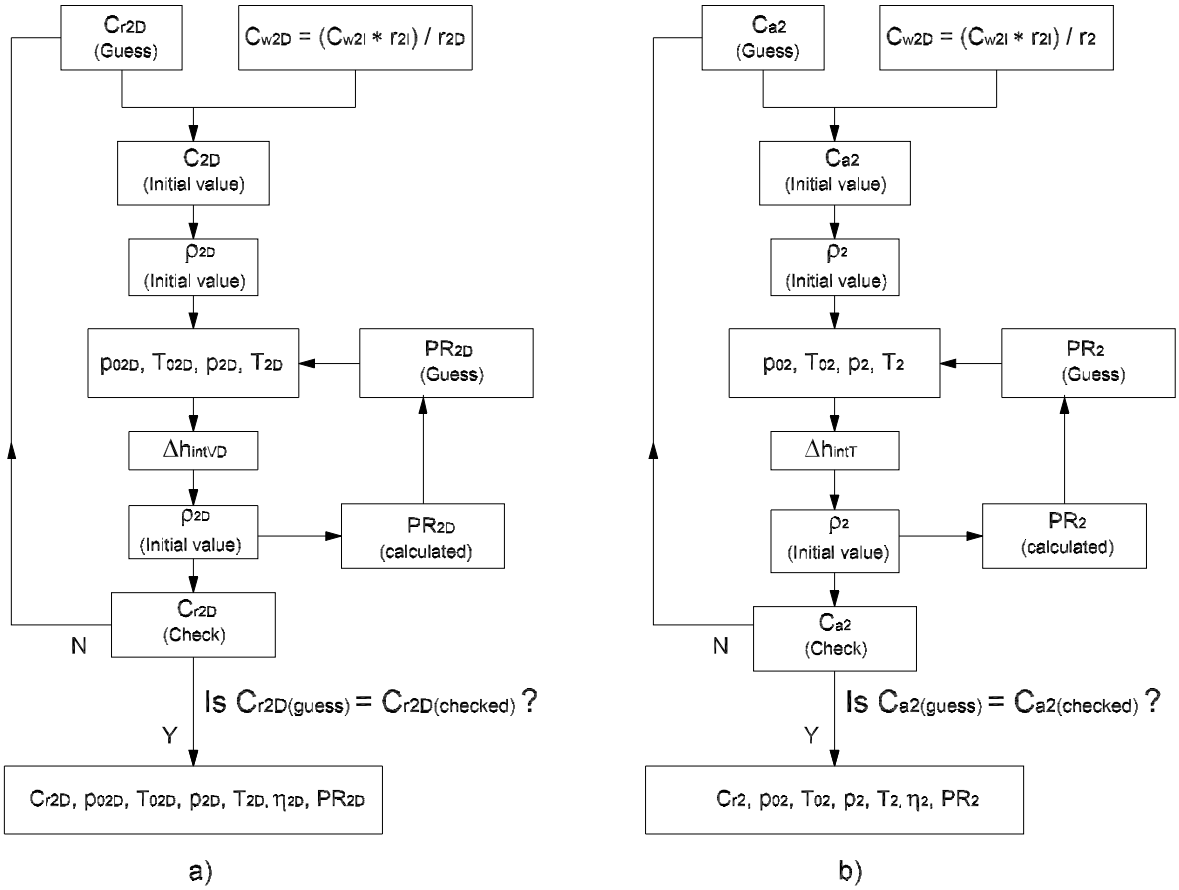

Figure 3–8: Flow diagram of the iterative procedure for obtaining parameters at: a) station "2D" and b) station "2".

3.2.6 Velocity triangle at vaned diffuser exit or station "2"

At this station the whirl component of the velocity, will be found through the conservation of angular momentum, $C_{w2}\, r_2 = C_{w2D}\, r_{2D}$, then:

$$C_{w2} = \frac{C_{w2D}\, r_{2D}}{r_2}; \qquad \text{m/s} \qquad (3.62)$$

The area and the absolute velocity (magnitude) are:

$$C_2 = \sqrt{C_{a2}^2 + C_{w2}^2}; \qquad \text{m/s} \qquad (3.63)$$

$$A_2 = 2\pi\, r_2\, b_2; \qquad m^2 \qquad (3.64)$$

The procedure to obtain the velocities and the thermodynamic states are similar to the previous case.

Assumptions done for the case of vaneless diffuser may be applied for the diffuser, so:

$$h_{02D} = h_{02} \tag{3.65}$$

In the relations (3.59) and (3.60) we have to consider the losses through the entire compressor stage (impeller, vaneless diffuser and vaned diffuser), as shown in the next relation:

$$\sum \Delta h_{intT} = \sum \Delta h_{intVD} + \Delta h_{iD} + \Delta h_{sfD}; \qquad \text{J/kg} \tag{3.66}$$

$$\tag{3.67}$$

3.3 Turbine Map

The SR-30 has a single stage axial turbine composed of one row of nozzles and one rotor. Once again we will verify the results about the design point of velocity triangles presented in reference [9].

3.3.1 Previous considerations

Figure 3–9 shows the nomenclature employed in the calculations for an axial flow turbine stage.

The design point losses were calculated based on Ainley and Mathieson correlations [22]. The parameters to be estimated with which we will build the turbine maps are related as:

$$PR_t = f_{PR_t}(\dot{m}, N) \tag{3.68}$$

$$\eta_t = f_{\eta_t}(\dot{m}, N) \tag{3.69}$$

The operating conditions to develop the design point velocity triangles were:

$$\dot{m} = 0.3 \ : \text{Total mass flow (kg/s)}$$

$$N = 78000 \ : \text{Rotational speed (rpm)}$$

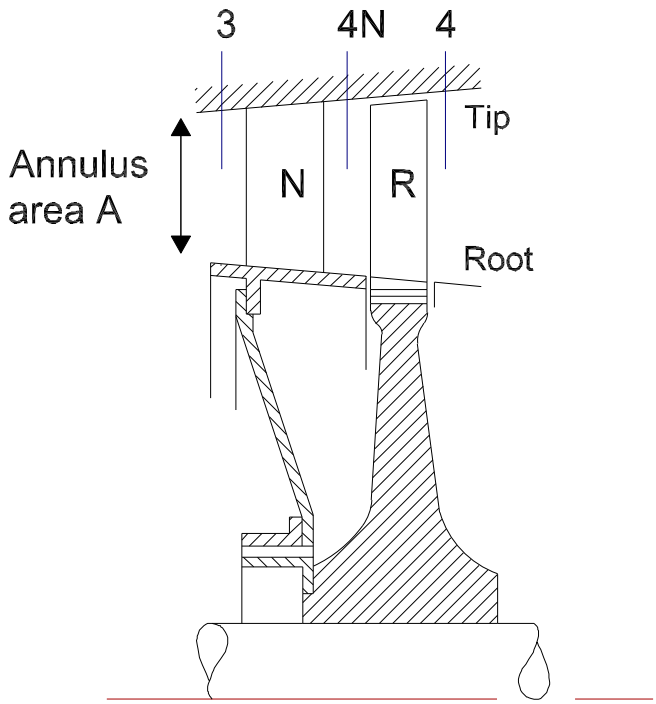

Figure 3–9: Nomenclature for the axial turbine.

After the design point velocity triangle is calculated, the off design velocity triangles may be generated, where each velocity triangle corresponds to one operating condition. By sweeping the operating conditions such as like the spool rotational speed and mass flow, the off-design velocity triangles are drawn, at the rotor inlet and rotor outlet. The operating conditions vary in the following ranges of values:

$$\dot{m} = 0.1 - 0.32; \qquad \text{kg/s}$$

$$N = 50000 - 90000; \qquad \text{rpm}$$

A Mollier diagram showing the change of state through a complete turbine stage, including the effects of irreversibility, is given in Figure 3–10.

For preliminary calculations, it is sufficiently accurate to take the intensity of mass flow at the mean diameter as being the mean intensity of the mass flow, this is one reason why it is convenient to design the turbine on conditions at mean diameter. Moreover, we can consider the mean diameter equal in all stations because the difference between the station mean diameters are negligible, so the effective

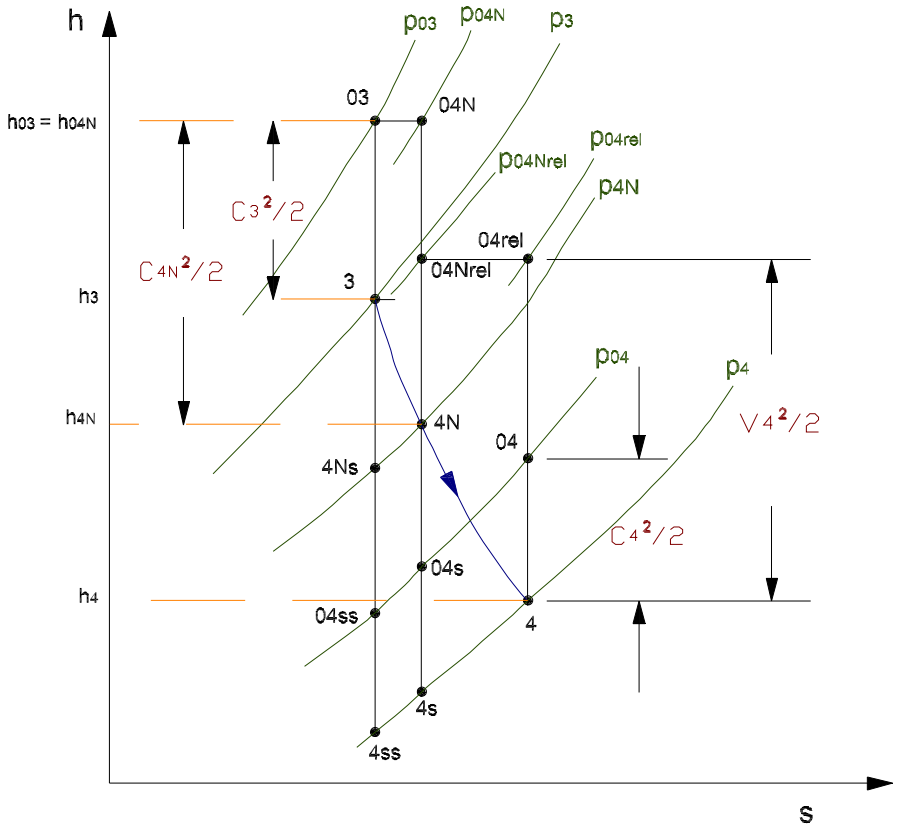

Figure 3–10: Mollier diagram for a turbine stage.

diameter at each station will be as follow:

$$D_m = \frac{1}{2}\left(D_r^2 + D_t^2\right); \qquad \text{mm} \tag{3.70}$$

With the effective diameter calculated in equation 3.70 and the rotational speed, we can obtain the mean blade speed which will be useful for the calculation in each station, this is:

$$U = \frac{\pi\, D_m\, N}{60000}; \qquad \text{m/s} \tag{3.71}$$

The mean annulus area for each station, will be calculated from:

$$A_m = 10^{-6} * \frac{\pi\left(D_{tip}^2 - D_{root}^2\right)}{4}; \qquad m^2 \tag{3.72}$$

3.3.2 Data

Geometric dimensions and inlet conditions are presented in table 3–3, these were extracted from Witkowski et al. [9].

Table 3–3: Dimensions of the turbine stage and inlet conditions of the flow entering the nozzle.

Rotor	**Inlet conditions**
- Root diameter: $D_h = 64\,mm$	$p_{01} = 250\,kPa$
- Tip diameter: $D_{tip} = 88.9\,mm$	$T_{01} = 973\,K$
- Blade max. thickness: $t = 3\,mm$	
- Point max. thickness: $a = 10.3\,mm$	$C_{W1} = 0$
- Chord length: $L = 18.2\,mm$	(No pre-swirl of the flow
- Number of blades in the rotor: 26	entering the impeller)
- Number of blades in the stator: 21	
- Blade angle at rotor inlet: $\beta'_{4N} = 58\,deg$	
- Blade angle at rotor outlet: $\beta'_4 = 68\,deg$	
- Tip clearance: $\kappa = 2.44\,mm$	

It is assumed that the stator blades have the same shape as the rotor blades.

The fluid through the turbine is the air-fuel combustion products, its properties, are determined based on equations 3.1, 3.3, 3 and 3.8.

In the following sections, calculations of design point velocity triangles are presented.

3.3.3 Velocity triangle at nozzle inlet or station "3"

In a single-stage turbine the velocity at turbine inlet C_3 will be axial, so, the angle between the absolute flow velocity and the axial shaft $\alpha_3 = 0$, and $C_3 = C_{a3}$ (C_{a3} is the axial component of the velocity at turbine inlet) [46], this will be taken as constant for all off-design conditions. It can be viewed in the figure 3–11.

Figure 3–12 shows the iterative procedure to calculate C_{a3}, this method is similar to the calculation made for the entrance of the compressor impeller. The calculations of static temperature and pressure are obtained from the thermodynamic relations according to the Mollier diagram for a turbine stage, Figure 3–10, as follow:

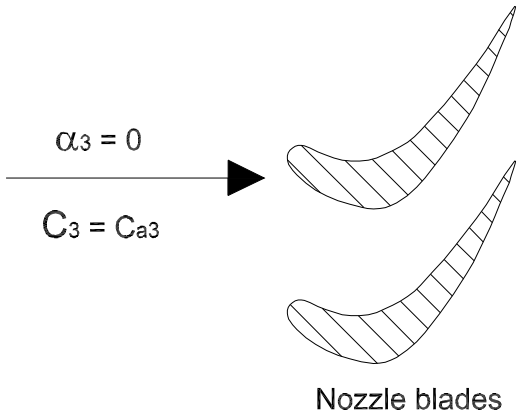

Figure 3–11: Velocity diagram at the nozzle inlet.

$$h_{03} = f_h(T_{03},\, FAR); \qquad \text{J/kg} \tag{3.73}$$

$$h_3 = h_{03} - \frac{1}{2}C_3^2; \qquad \text{J/kg} \tag{3.74}$$

$$T_3 = f_T(h_3); \qquad \text{K} \tag{3.75}$$

$$\phi_{03} = f_\phi(T_{03}); \qquad \text{J/kg} \tag{3.76}$$

$$\phi_3 = f_\phi(T_3); \qquad \text{J/kg} \tag{3.77}$$

$$p_3 = \frac{p_{03}}{e^{\frac{phi_{03}-phi_3}{R}}}; \qquad \text{kPa} \tag{3.78}$$

The density calculated is:

$$\rho_3 = 10^3 * \frac{p_3}{R\,T_3}; \qquad kg/m^3 \tag{3.79}$$

From continuity equation, the axial velocity C_{a3} is:

$$C_{a3} = C_3 = \frac{\dot{m}}{\rho_3\, A_m}; \qquad \text{m/s} \tag{3.80}$$

And the corresponding mach number is:

$$M_{3abs} = \frac{C_3}{\sqrt{\gamma\, R\, T_3}} \tag{3.81}$$

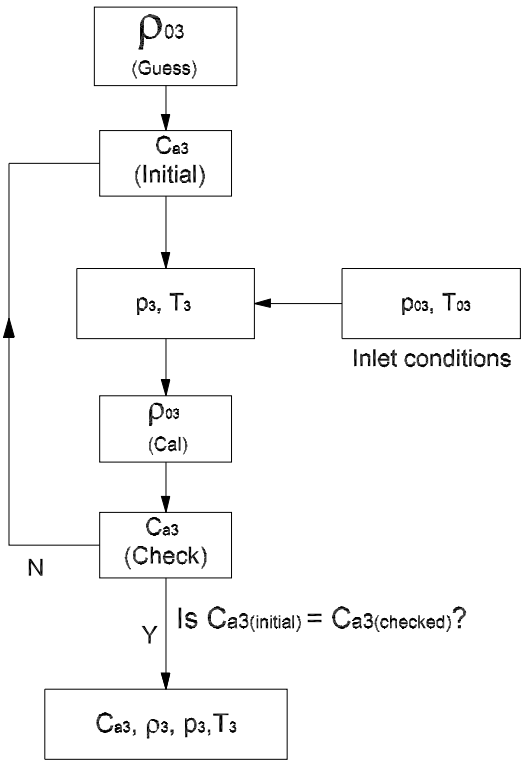

Figure 3–12: Iteration procedure to calculate the axial velocity C_{a3}.

3.3.4 Velocity triangle at nozzle outlet or station "4N"

It was assumed, in the last section the inlet flow gas angle as constant an equal to the vane angle, now, here we can consider the deviation across the nozzle as constant at all off-design conditions, so:

$$\alpha_{4N} = constant \tag{3.82}$$

This will result in the losses across the nozzle being constant for all off-design conditions. As a result, the relationship between the whirl component C_{w4N} and the axial component C_{a4N}, shown in figure 3–13, will be constant according to the next relation:

$$\tan \alpha_{4N} = \frac{C_{w4N}}{C_{a4N}} \tag{3.83}$$

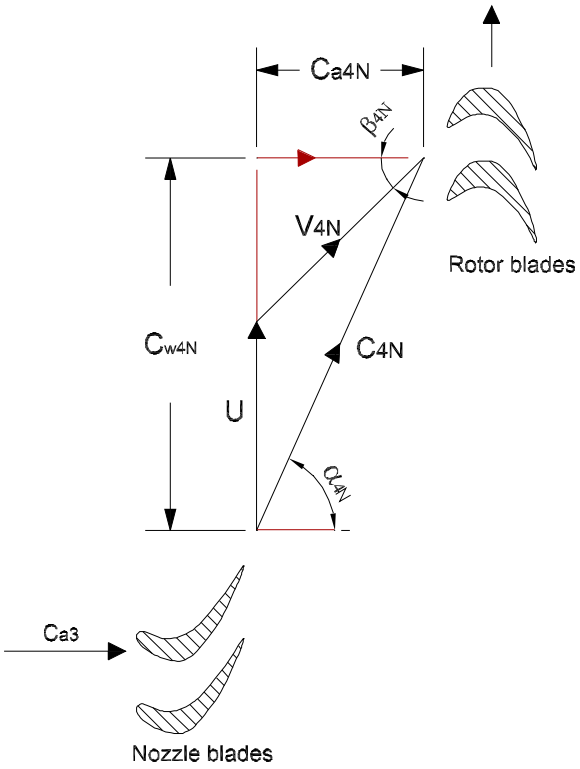

Figure 3–13: Velocity diagram at station "4N".

Since no work is done (adiabatic process) by the gas in the nozzle, h_0 must be constant over the annulus at the outlet, then from Mollier diagram shown in figure 3–10, $h_{03} = h_{04N}$.

Figure 3–13 shows the iteration procedure to obtain the axial component of the absolute velocity C_{a4N}. Stagnation and static temperatures and pressures are obtained from Mollier diagram (3–10) using the following relationships:

$$h_{4N} = h_{04N} - \frac{1}{2}C_{4N}^2; \qquad \text{J/kg} \qquad (3.84)$$

$$T_{4N} = f_T(h_{4N}); \qquad \text{K} \qquad (3.85)$$

$$h_{4Ns} = h_{4N} - \lambda_N \frac{C_{4N}^2}{2}; \qquad \text{J/kg} \tag{3.86}$$

$$T_{4Ns} = f_T(h_{4Ns}); \qquad \text{K} \tag{3.87}$$

$$\phi_{03} = f_\phi(T_{03}); \qquad \text{J/kg} \tag{3.88}$$

$$\phi_{4Ns} = f_\phi(T_{4Ns}); \qquad \text{K} \tag{3.89}$$

$$P_{4N} = \frac{P_{03}}{e^{\frac{\phi_{03}-\phi_{4Ns}}{R}}} \tag{3.90}$$

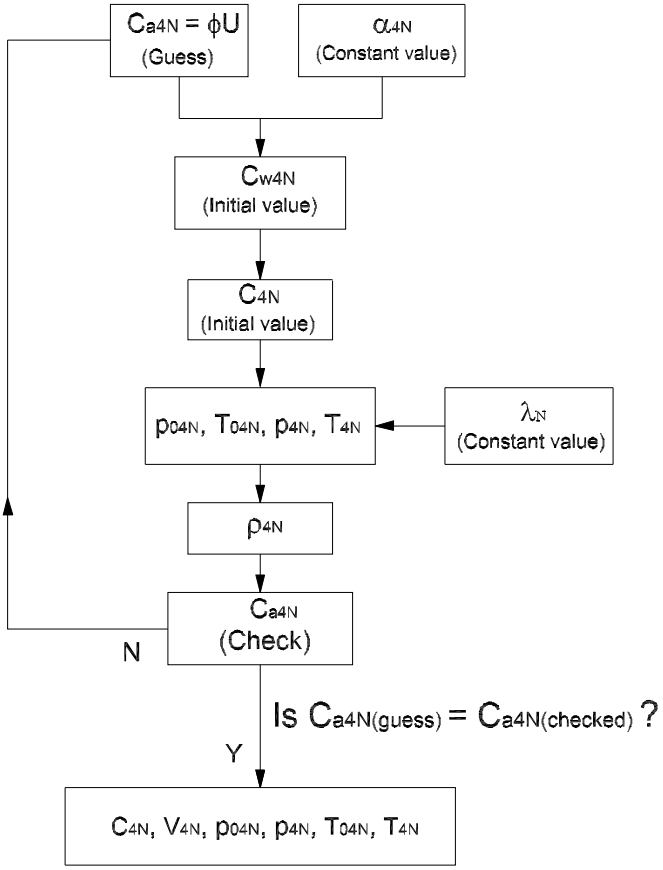

Figure 3–14: Flow diagram of iterative procedure at station "4N".

The critical pressure ratio was taken into account, which ignoring the effect of friction, is as follow:

$$\frac{P_{03}}{P_c} = \left(\frac{\gamma+1}{2}\right)^{\frac{\gamma}{\gamma-1}} \tag{3.91}$$

If the pressure ratio $P_{03}/P_{4N} < P_{03}/P_c$, then, the nozzle is not chocked.

The density ρ_{4N} and the axial flow velocity C_{a4N} are as follow:

$$\rho_{4N} = 10^3 * \frac{P_{4N}}{R\,T_{4N}}; \qquad kg/m^3 \tag{3.92}$$

$$C_{a4N} = \frac{\dot{m}}{\rho_{4N}\,A_m}; \qquad \text{m/s} \tag{3.93}$$

The whirl component of velocity C_{w4N}, the absolute velocity C_{4N} and the relative velocity V_{4N} are respectively:

$$C_{w4N} = C_{a4N}\tan\alpha_{4N}; \qquad \text{m/s} \tag{3.94}$$

$$C_{4N} = \sqrt{C_{a4N}^2 + C_{w4N}^2}; \qquad \text{m/s} \tag{3.95}$$

$$V_{4N} = \sqrt{(C_{w4N} - U)^2 + C_{a4N}^2}; \qquad \text{m/s} \tag{3.96}$$

The absolute and relative flow angles are:

$$\alpha_{4N} = \arctan\left(\frac{C_{w4N}}{C_{a4N}}\right) \tag{3.97}$$

$$\beta_{4N} = \arctan\left(\frac{C_{w4N} - U}{C_{a4N}}\right) \tag{3.98}$$

3.3.5 Velocity triangle at rotor outlet or station "4"

The flow diagram of the iterative procedure at station "4" is presented in Figure 3–15. According to this diagram, we first calculate the exit angle β_4 from the equations shown in references [22] and [9]:

$$\beta_4 = \begin{cases} -11.5 + 1.154\,cos^{-1}\left(\frac{\theta}{s}\right) + \frac{4\,s}{e} & \text{if } 0 < M_4 \leq 0.5, \\ cos^{-1}\left(\frac{\theta}{s}\right) & \text{if } M_4 \geq 1. \end{cases} \tag{3.99}$$

Where $\frac{\Theta}{s} = 0.41$.

In order to perform the first approximation regarding the axial component of the absolute velocity, $C_{a4} = C_{a4N}$. Using the two previous parameters the whirl component of the absolute velocity can be evaluated, as follows:

$$C_{w4} = U - C_{a4}\, tan\beta_4; \qquad \text{m/s} \qquad (3.100)$$

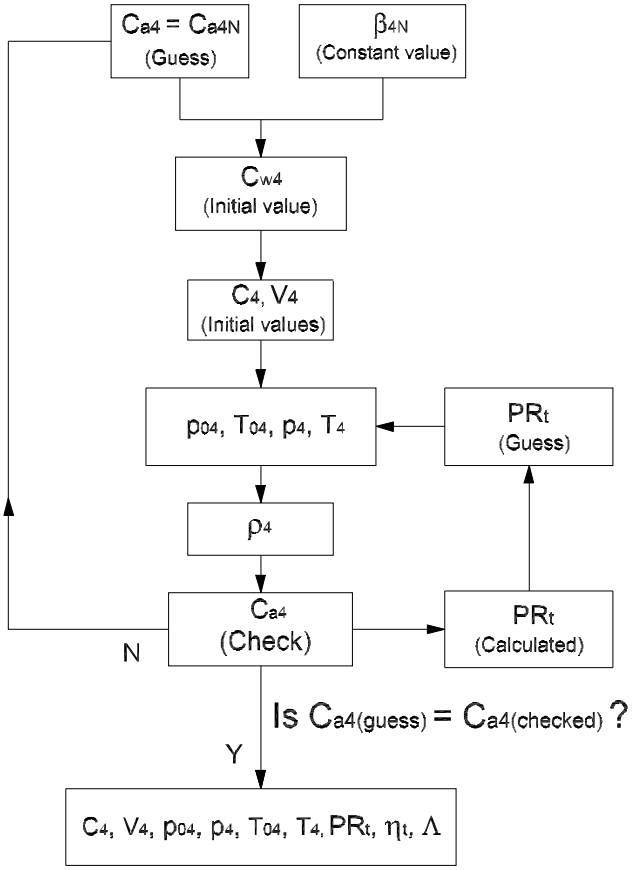

Figure 3–15: Flow diagram of iterative procedure at station "4".

The absolute and relative velocity can be found, according to the figure 3–16 at station "4", from the following equations,

$$C_4 = \sqrt{C_{w4}^2 + C_{a4}^2} \qquad (3.101)$$

$$V_4 = \sqrt{(U - C_{w4})^2 + C_{a4}^2} \qquad (3.102)$$

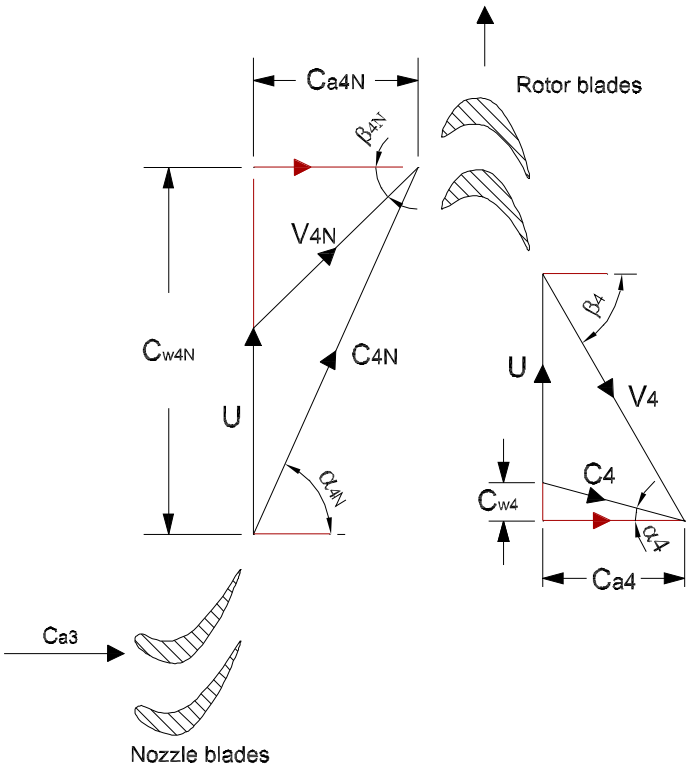

Figure 3–16: Velocity diagram of the total stage.

When the velocity triangles are superimposed, the velocity diagram for the stage is shown in Fig. 3–17. The geometry of the diagram provides the following equations:

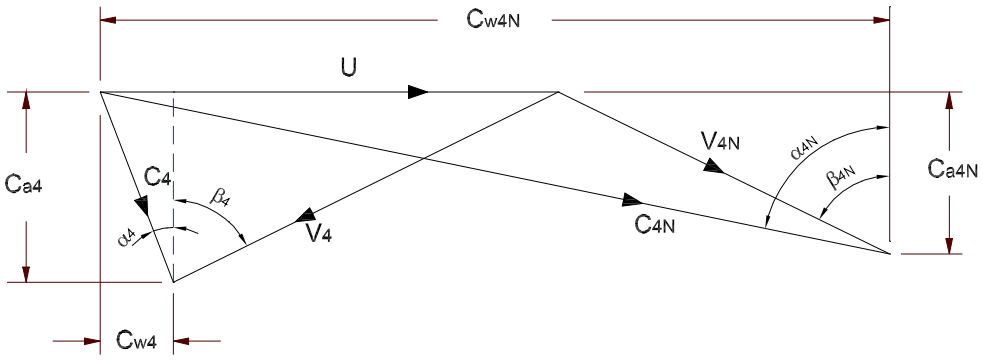

Figure 3–17: Superimposed velocity diagram.

$$\frac{U}{C_{a4N}} = \tan\alpha_{4N} - \tan\beta_{4N} \tag{3.103}$$

$$\frac{U}{C_{a4}} = \tan\beta_4 + \tan\alpha_4 \tag{3.104}$$

Applying the principle of angular momentum to the rotor, the stage work output per unit mass flow is:

$$W_s = h_{03} - h_{04} = U(C_{w4N} + C_{w4}) \tag{3.105}$$

Therefore, from equation 3.105 and Fig. 3–17 we obtain a relationship with which we can obtain the stagnation entalphy at station "4".

$$h_{04} = h_{03} - U\,C_{a4N}\left(\frac{2\,U}{C_{a4N}} + \tan\beta_{4N} - \frac{C_{a4}}{C_{a4N}}\,\tan\beta_4\right); \qquad \text{J/kg} \tag{3.106}$$

Again, from Mollier diagram (figure 3–10), the relationships used to find the stagnation and static temperatures are, as follows,

$$h_4 = h_{04} - \frac{1}{2}\,C_4^2; \qquad \text{J/kg} \tag{3.107}$$

$$T_4 = f_T(h_4,\, FAR); \qquad \text{K} \tag{3.108}$$

$$T_{04} = f_T(h_{04},\, FAR); \qquad \text{K} \tag{3.109}$$

And to obtain the stagnation and static pressures, the equations are:

$$P_{04} = \frac{P_{03}}{PR_t}; \qquad \text{kPa} \tag{3.110}$$

$$P_4 = \frac{P_{04}}{e^{\frac{\phi_{04}-\phi_4}{R}}}; \qquad \text{kPa} \tag{3.111}$$

where an initial value for PR_t is assumed and and at the end it is calculated, then $\phi_{04} = f_\phi(T_{04})$ and $\phi_4 = f_\phi(T_4)$.

As in the previous cases, the density and the axial velocity component are calculated,

as follows,

$$\rho_4 = 10^3 * \frac{P_4}{R\,T_4}; \qquad kg/m^3 \tag{3.112}$$

$$C_{a4} = \frac{\dot{m}}{\rho_4\,A_m}; \qquad m/s \tag{3.113}$$

The Mach numbers is estimated from:

$$(M_4)_{abs} = \frac{C_4}{\sqrt{\gamma\,R\,T_4}} \tag{3.114}$$

$$(M_4)_{rel} = \frac{V_4}{\sqrt{\gamma\,R\,T_4}} \tag{3.115}$$

The degree of reaction Λ which expresses the fraction of the stage expansion which occurs in the rotor, and it is usual to define it in terms of static enthalpy (or temperature) drops, namely:

$$\Lambda = \frac{h_{4N} - h_4}{h_3 - h_4} \tag{3.116}$$

Previous calculations to find isentropic efficiency and pressure ratio are,

$$h_{4s} = h_4 - \frac{1}{2}\,V_4^2\,\lambda_R; \qquad \text{J/kg} \tag{3.117}$$

$$h_{4ss} = h_{4s} - \left(\frac{T_4}{T_{4N}}\right)(h_{4N} - h_{4Ns}); \qquad \text{J/kg} \tag{3.118}$$

$$T_{4ss} = f_T(h_{4ss}); \qquad \text{K} \tag{3.119}$$

$$\phi_{4ss} = f_\phi(T_{4ss},\, FAR); \qquad \text{J/kg} \tag{3.120}$$

$$\phi_{04ss} = \phi_{4ss} + R\,ln\left(\frac{p_{04}}{p_4}\right); \qquad \text{J/kg} \tag{3.121}$$

$$T_{04ss} = f_T(\phi_{04ss},\, FAR); \qquad \text{K} \tag{3.122}$$

$$h_{04ss} = f_h(T_{04ss}); \qquad \text{K} \tag{3.123}$$

where λ_R is the total loss coefficient in the turbine rotor.

Then, the isentropic efficiency is calculated by:

$$\eta_t = \frac{h_{03} - h_{04}}{h_{03} - h_{04ss}} \tag{3.124}$$

Finally, the pressure ratio (or expansion ratio) can be found from:

$$PR_t = \frac{p_{03}}{p_{04}} = e^{\frac{\phi_{03}-\phi_{04ss}}{R}} \tag{3.125}$$

3.3.6 Estimation of nozzle losses

The loss coefficients were obtained from Dixon [22].

a) Profile loss coefficient

$$Y_p = \left\{ Y_{p(\alpha_3=0)} + \left(\frac{\alpha_3}{\alpha_{4N}}\right)^2 \left[Y_{p(\alpha_3=\alpha_{4N})-Y_{p(\alpha_3=0)}} \right] \right\} \left(\frac{t/l}{0.2}\right)^{\alpha_3/\alpha_{4N}} \tag{3.126}$$

where α_3 and α_{4N} will be found on figure 7-24 from reference [46] or figure 3-25 from reference [22].

If $(M_{4N})_{abs} > 1$ then:

$$Y_p = [Y_p \text{ from eq. } 3.126] * [1 + 60(M_{4N} - 1)^2] \tag{3.127}$$

a) Secondary losses

This correlation was given by Dunham and Came (reported by Dixon [22]).

$$Y_s = 0.0334\left(\frac{l}{H}\right)\left(\frac{cos\alpha_{4N}}{cos\alpha'_3}\right)Z \tag{3.128}$$

According to Witkowski [9], $H/l = 1.46$, "Z" is the Zweifel parameter which can be obtained from:

$$Z = \left(\frac{C_L}{s/l}\right)^2 \frac{cos^2\alpha_{4N}}{cos^3\alpha_m} \tag{3.129}$$

where C_L is the lift coefficient and the equation which can be obtained is,

$$C_L = 2\left(\frac{s}{l}\right)\cos\alpha_m(\tan\alpha_3 + \tan\alpha_{4N}) - C_D\tan\alpha_m \tag{3.130}$$

where,

$$\alpha_m = \arctan\left[\frac{1}{2}(\tan\alpha_{4N} - \tan\alpha_3)\right]$$

$$C_D = 0.02 : \text{Drag coefficient}$$

$$\frac{s}{l} = \frac{2\pi\, r_{pitch}}{l * \eta_{b,stator}}$$

Finally the total loss coefficient is,

$$\lambda_N = Y_p + Y_s \tag{3.131}$$

3.3.7 Estimation of rotor losses

a) Profile loss coefficient

$$Y_p = \left\{Y_{p(\beta_{4N}=0)} + \left(\frac{\beta_{4N}}{\beta_4}\right)^2 \left[Y_{p(\beta_{4N}=\beta_4)} - Y_{p(\alpha_{4N}=0)}\right]\right\}\left(\frac{t/l}{0.2}\right)^{\beta_{4N}/\beta_4} \tag{3.132}$$

Where β_{4N} and β_4 will be found on figure 7-24 from reference [46] or figure 3-25 from reference [22].

If $(M_4)_{rel} > 1$ then:

$$Y_p = [Y_p \text{ from eq. } 3.132] * [1 + 60(M_4 - 1)^2] \tag{3.133}$$

b) Secondary losses

$$Y_s = 0.0334\left(\frac{l}{H}\right)\left(\frac{cos\beta_4}{cos\beta'_{4N}}\right)Z \tag{3.134}$$

Z is the Zweifel parameter which can be obtained from:

$$Z = \left(\frac{C_L}{s/l}\right)^2 \frac{cos^2\beta_4}{cos^3\beta_m} \tag{3.135}$$

where C_L is the lift coefficient and the equation which can be obtained is:

$$C_L = 2\left(\frac{s}{l}\right)\cos\beta_m(\tan\beta_{4N} + \tan\beta_4) - C_D\tan\beta_m \tag{3.136}$$

where,

$$\beta_m = \tan^{-1}\left[\frac{1}{2}(\tan\beta_4 - \tan\beta_{4N})\right]$$

$$C_D = 0.02 : \text{Drag coefficient}$$

c) Tip clearance loss can be calculated as follows,

$$Y_k = B\left(\frac{l}{H}\right)\left(\frac{k}{l}\right)^{0.78} Z \tag{3.137}$$

Where $B = 0.5$ for plain tip clearance.

So, the total loss coefficient is:

$$\lambda_R = Y_p + Y_s + Y_k \tag{3.138}$$

3.4 Results

3.4.1 Compressor map

Results for the design point performance

The results at each location for the design point operation, from the analysis described above, is presented in table 3–4. These approximately match the results published by Witkowski et al. [9]. This table was generated under the rotational speed of $N = 78000\,rpm$ and $\dot{m} = 0.297\,kg/s$.

where P.W. means present work.

The plots corresponding to the results at the design point performance, shown in table 3–4, are presented in Figures 3–18 and 3–19.

The plots presented in Fig. 3–18 and 3–19 show pressure ratio vs flow capacity characteristic and efficiency vs mass flow rate characteristic under a fixed rotational speed ($N = 78000rpm$) and a variable mass flow rate. As shown, point "A" corresponds to maximum efficiency and maximum pressure ratio and any further increase in mass flow will result in a fall of pressure ratio. On the other hand, at point "B"

Table 3–4: Results of thermal and hydraulic analysis for the compressor.

Parameters	Inlet to impeller		Exit of impeller		Entrance to vaned diffuser		Exit to vaned diffuser	
	1		2I		2D		2	
	Ref. [9]	P.W.	Ref. [9]	P.W.	Ref. [9]	P.W.	Ref. [9]	P.W.
Area (m^2)	0.002522	0.002522	0.001714	0.001714	0.001874	0.001874	0.002622	0.002622
P_0 (kPa)	100	100	323	323.01	319	306.87	269	286.84
T_0 (K)	300	300	445	446.32	445	446.32	445	446.32
P (kPa)	93.6	93.591	167	183.18	199.5	191.15	269	249.07
T (K)	294	294.37	379	380.15	390	390.42	430	428.9
C (m/s)	106	106.3	366.5	366.47	335.2	336.94	175.6	188.34
Mabs	0.31	0.309	0.87	0.94	0.86	0.85	0.42	0.45
V (m/s)	195	196.45	123	—	—	—	—	—
Mrel	0.57	0.571	0.31	—	—	—	—	—
U (m/s)	163.7	163.7	416.6	—	—	—	—	—

a breakaway of the air occurs due to the mass flow greatly in excess of that corresponding to the design mass flow (0.297kg/s [9]).

Off-design performance

After the design point velocity triangle is calculated, the rotational speed and the mass flow rate are varied to obtain the off-design performance, as shown in the Figure 3–20. The assumptions made in the off-design calculations are that the absolute inlet velocity remains axial, and the design point value of the slip factor was also relatively constant for all off-design conditions. Figures 3–21 and 3–22 show characteristics curves obtained for different speeds. Figure 3–21 shows the variation of pressure ratio over the complete range of mass flow and rotational speed; the left-hand extremities of the constant speed curves may be joined up to form the surge line, while the right-hand extremities represent the points where choking occurs.

3.4.2 Turbine map

Design point performance

The results for the design point analysis at a constant speed (N=78000rpm) and a constant mass flow ($\dot{m} = 0.3kg/s$) are presented in table 3–5. This table also shows the comparison with the results obtained from reference [9]. It can be observed that both results match closely at locations "3" and $4N$ (although, from reference [9], there is an error in the calculations of static pressure and temperature). The great difference between both results are in the absolute and relative velocities on location "4".

Table 3–5: Results of thermal and hydraulic analysis for the turbine.

Parameters	Inlet to stator		Exit from stator and entrance to rotor		Exit from rotor	
	3		4N		5	
	Ref. [9]	Present work	Ref. [9]	Present work	Ref. [9]	Present work
Area (m^2)	0.001714	0.001714	0.001874	0.001874	0.002622	0.002622
P_0 (kPa)	250	250	233.5	228.83	120	120.13
T_0 (K)	973	973	973	973	841.3	854.76
P (kPa)	93.6	244.23	127.6	127.85	115	105.55
T (K)	294	967.41	833.5	841.09	832.4	827.24
C (m/s)	114	114.08	556.8	550.33	140.8	249.93
Mabs	0.19	0.19	0.98	0.97	0.25	0.37
V (m/s)	—	—	255	259.62	260	307.64
Mrel	—	—	0.45	0.46	0.46	0.56
U (m/s)	—	—	316.3	316.3	—	—

After performing the design point calculations, the characteristic curves such as like the mass flow rate vs work parameter are plotted as shown in Figure 3–23 and the efficiency vs work parameter as shown in Figure 3–24.

As shown in Fig. 3–23 the maximum value of $\dot{m}\sqrt{T_{03}}/p_{03}$ is reached at a work parameter which produce choking conditions at some point in the turbine. And Figure 3–24 shows that the efficiency is nearly constant.

Off-design performance

After doing the design point performance analysis we can vary the speed and the mass flow to obtain the off-design performance. The speed was varied form 50000rpm to 90000 rpm, and the mass flow was varied until the design mass flow value was reached ($0.3kg/s$).

Figure 3–25 shows that for every speed there is a maximum value of mass flow for which there is choke conditions at some point in the turbine. The constant speed lines merge into a single horizontal line at maximum mass flow.

Figure 3–26 shows that for rotational speed closely to the design point speed the efficiency is greater. Also it shows that the efficiency is nearly constant over a wide range of rotational speed and work parameter. This is because the accelerating nature of the flow turbine blading to operate over a wide range of incidence without much increase in the loss coefficient.

The results of the design point calculations for each component was compared with that presented by Witkowski et al [9]. In the case of compressor, the maximum difference was 9.5%, which correspond to the velocity at impeller exit. In the case of the turbine, there was a great difference in the velocity at the rotor exit, in 77%, however, in the rest of the parameters, the maximum error does not exceed 16%.

In order to further improve the modeling of the component maps, it should be developed the validation with experimental data or with maps obtained from manufacturers.

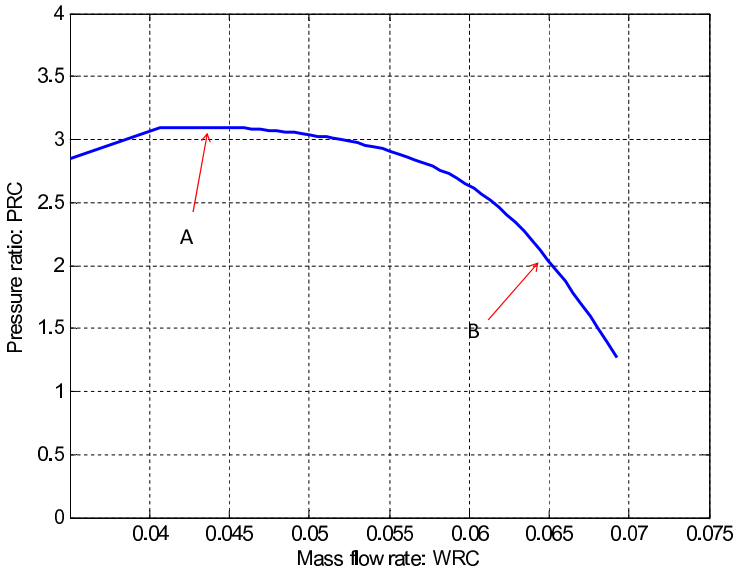

Figure 3–18: Pressure ratio vs mass flow rate design point characteristic curve.

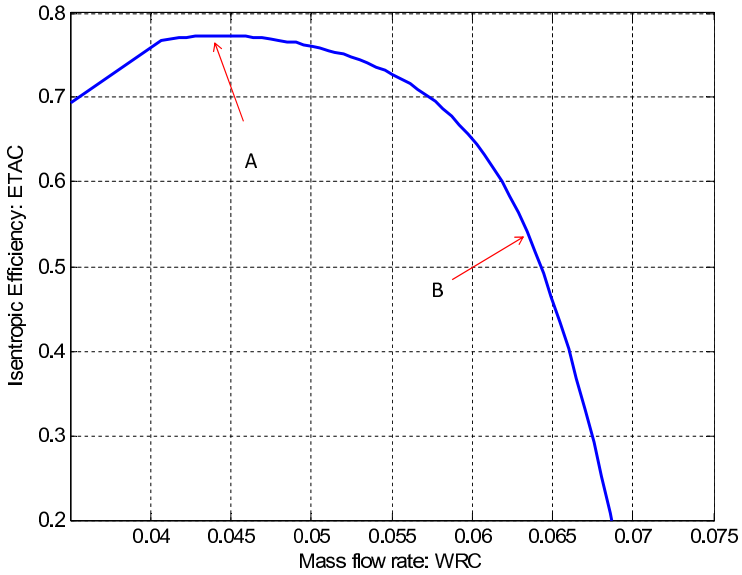

Figure 3–19: Isentropic efficiency vs mass flow rate design point characteristic curve.

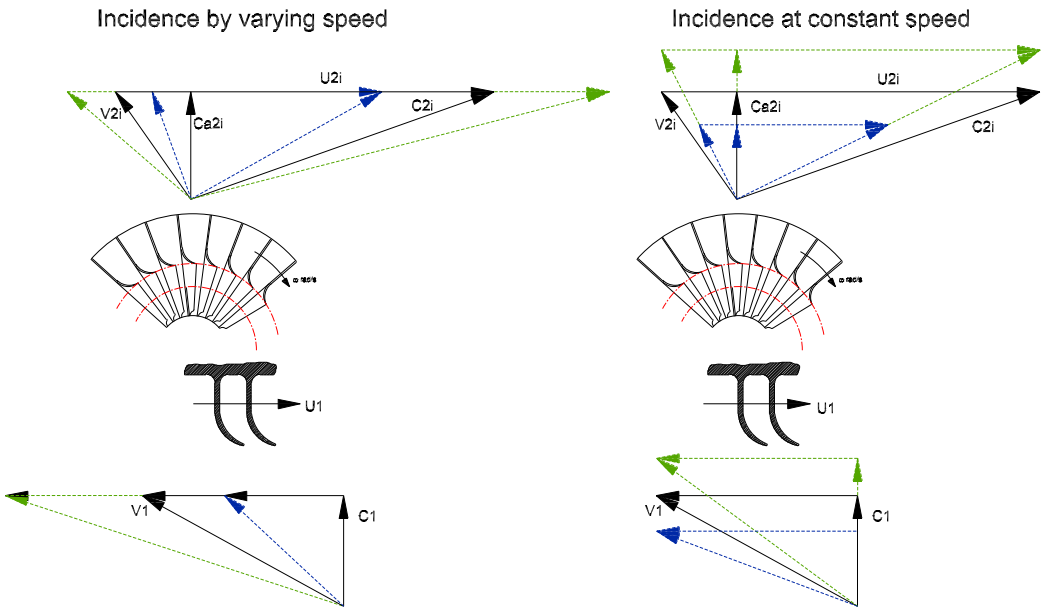

Figure 3–20: Velocity diagram for the off-design conditions.

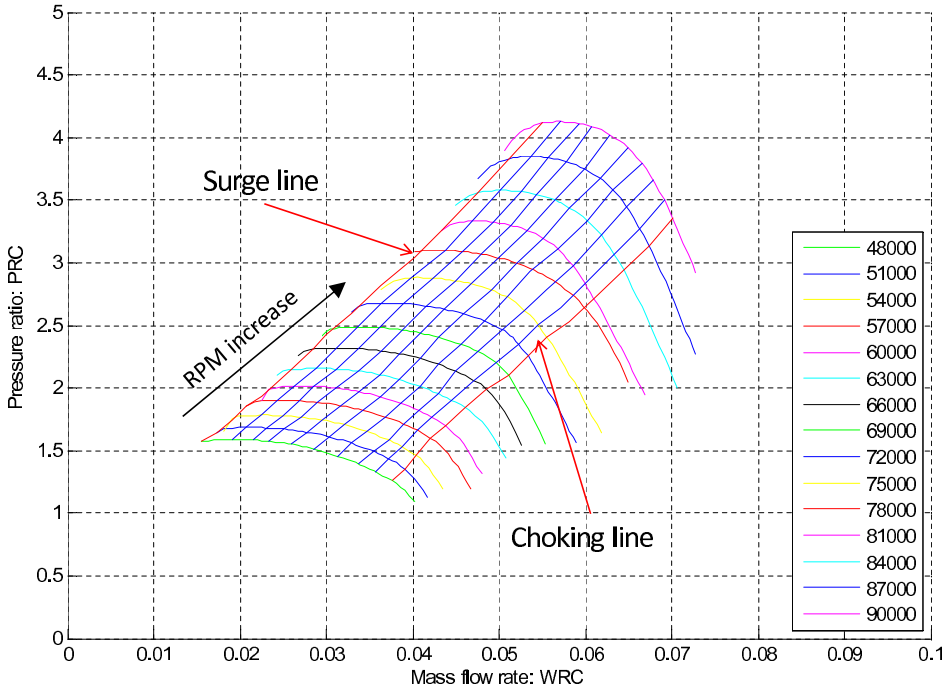

Figure 3–21: Pressure ratio vs mass flow rate characteristics for off-design performance.

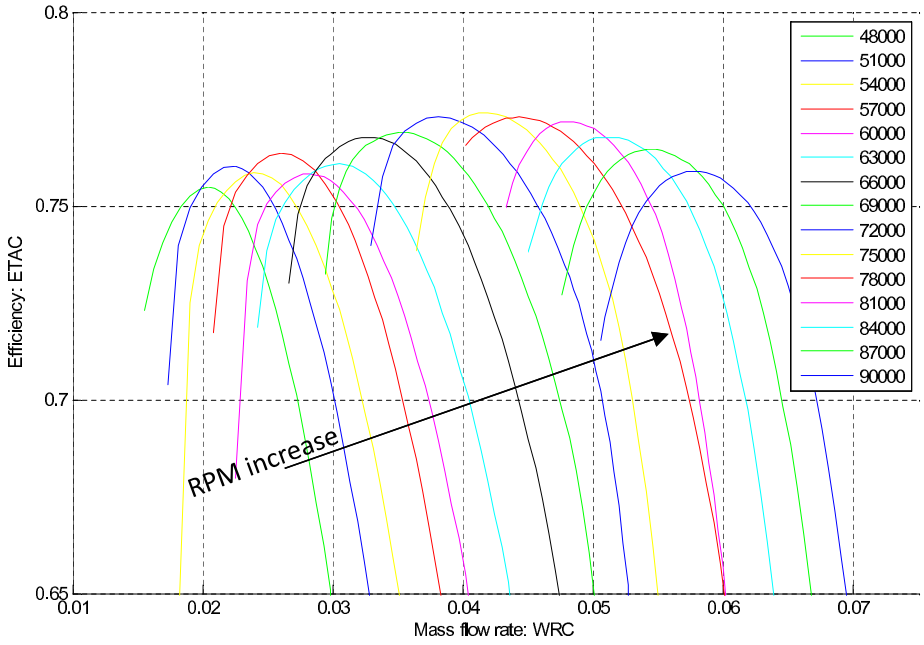

Figure 3–22: Efficiency vs mass flow rate characteristics for off-design performance.

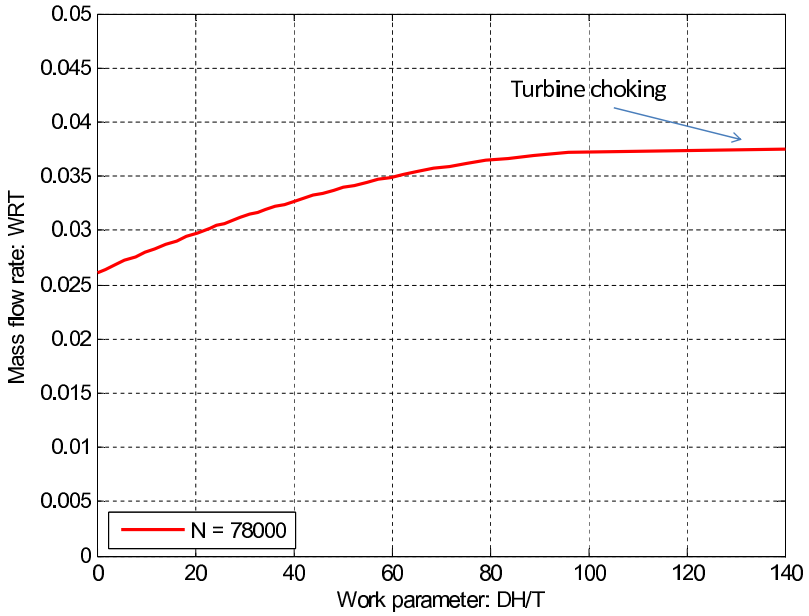

Figure 3–23: Mass flow rate vs work parameter characteristics for the design point rotational speed.

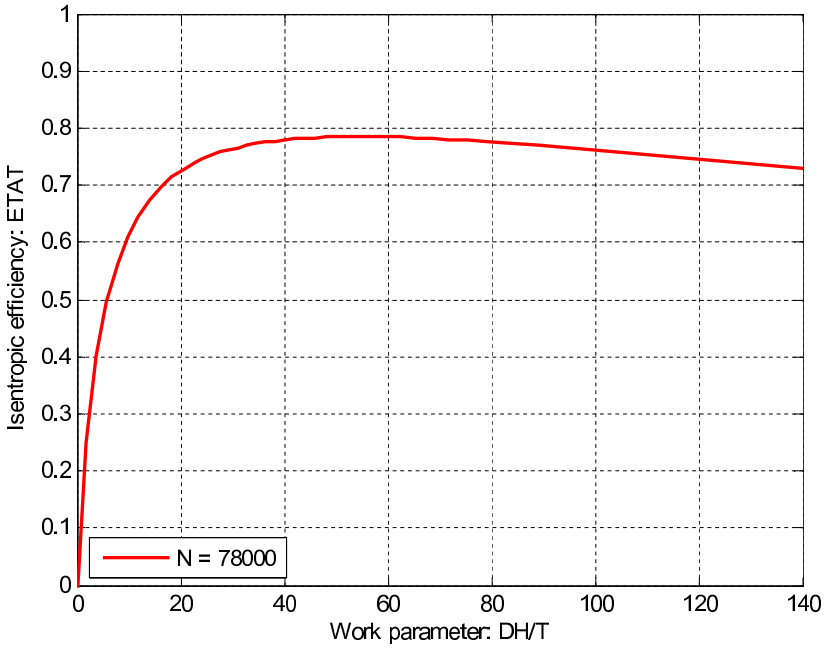

Figure 3–24: Efficiency vs work parameter characteristics for the design point rotational speed.

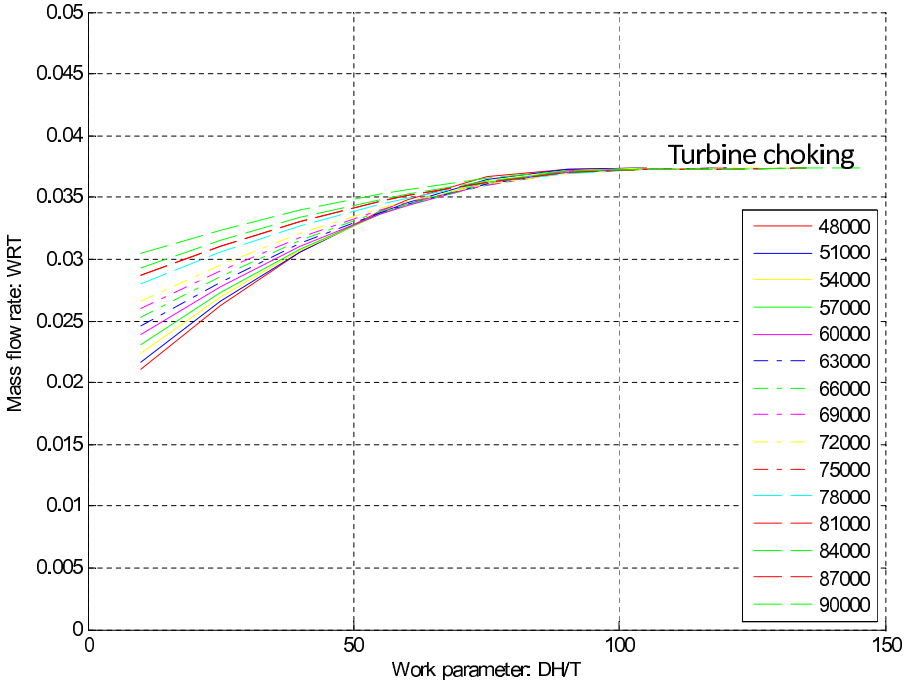

Figure 3–25: Mass flow rate vs work parameter characteristics under the off-design performance.

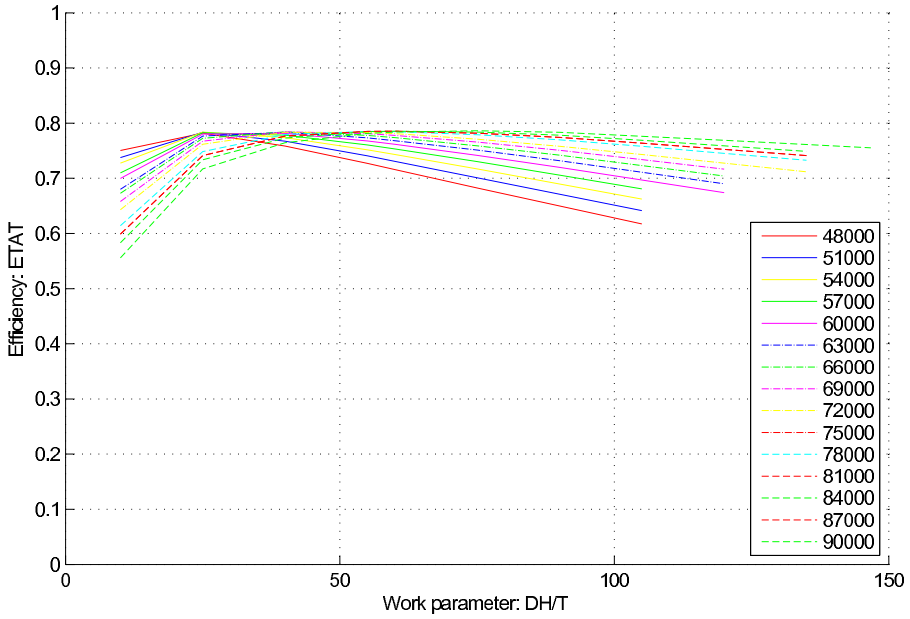

Figure 3–26: Efficiency vs work parameter characteristics under the off-design performance.

CHAPTER 4
ENGINE SIMULATION

In this chapter, the nonlinear simulation of the SR-30 turbojet engine will be developed. First, it is important to deal with the thermodynamic properties of the working fluid (air and combustion gases) that cross through the engine. The characteristics maps developed in the previous chapter will be useful to get an accurate engine model. The steady state model to be developed has a matching scheme which is basically as per a single spool gas generator and free power turbine. To meet this goal we need the information about the atmospheric conditions, the flight speed and installation pressure losses on each engine stage. The relations on each component and the iterative method applied to the model will be presented. Finally, transient performance above idle will be covered.

4.1 Steady State Performance

The first step to develop the steady state performance is to perform the design point performance calculation. Design point performance is central to the engine concept design process. The operating condition where an engine will spend most time has been traditionally chosen as the engine design point. The design rotational speed for the SR-30 engine was considered 78000 rpm [9].

The second step is to develop the off design engine performance modeling which determines each component's operating point as it is matched to the others. This step is often termed *matching*, and is a highly iterative process. The iterative procedure, for the SR-30 engine, requires successive guesses of the operating point

on compressor and turbine maps. These are updated as iteration continues until other known conditions are satisfied. Once this iteration is complete, overall cycle parameters such as thrust can be derived.

The iteration described above is achieved either via serial nested loops or via a matrix solution. Serial nested loops technique becomes computationally inefficient for more than five nested loops [50]. To model the off-design performance of SR-30 engine, it is possible to apply the serial nested loops technique due to the existence of only two nested loops.

4.1.1 Free stream Conditions

The free stream total pressure (P_{0a}) is a function of both pressure altitude and flight Mach number (M_a). Free stream total temperature (T_{0a}) is also a function of ambient temperature and flight Mach number [50]. The free conditions are obtained using the equations obtained from [46], as follow,

$$\frac{T_{0a}}{T_a} = [1 + \frac{\gamma - 1}{2} * M_a^2] \tag{4.1}$$

$$\frac{p_{0a}}{p_a} = \left(\frac{T_{0a}}{T_a}\right)^{\frac{\gamma}{\gamma-1}} \tag{4.2}$$

where γ is the ratio of specific heat, M_a is the inlet Mach number, T_a is the ambient temperature and p_a is the ambient pressure. T_a and p_a were taken equal to the mean temperature and pressure measured during the engine test.

Because the SR-30 gas turbine is a land based engine, we can assume the flight speed is set to zero, hence, the inlet mach number for the model is taken as zero ($M_a = 0$) for the inlet conditions of the engine. In addition if $M_a = 0$, according to the equations 4.1 and 4.2, the free stream temperature and pressure are as follow: $T_{0a} = T_a$ and $p_{0a} = p_a$.

4.1.2 Intake Ram Recovery

Figure 4–1 shows the Mollier diagram of the intake [22], this diagram will be considered for the nomenclature and the assumptions used in this work.

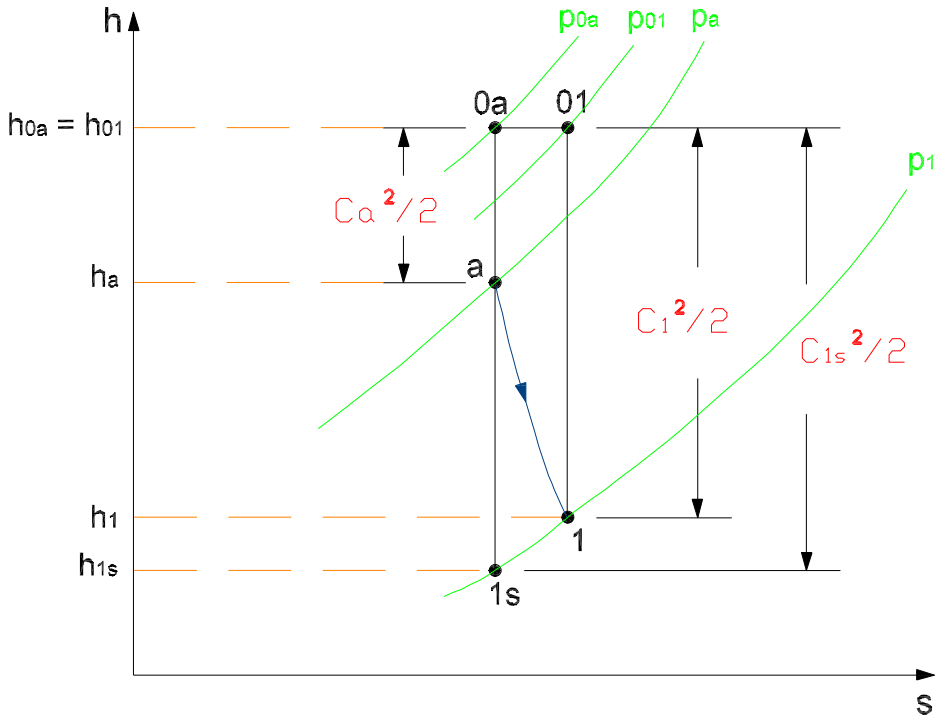

Figure 4–1: Mollier diagram through inlet bell.

The prime requirement of the intake is to minimize the pressure loss up to the compressor face while ensuring that the flow enters the compressor with a uniform pressure and velocity, at all flight conditions. The intake can be treated as an adiabatic duct. Since there is no heat or work transfer, the stagnation enthalpy is constant $h_{01} = h_{0a}$, as shown in Figure 4–1. Because the enthalpy is temperature dependent, it is assumed that:

$$T_{01} = T_{0a} \tag{4.3}$$

Under static conditions or at very low forward speeds, the intake acts as a nozzle in which the air accelerates from zero or low velocity C_a to C_1 at the compressor inlet [46]. For this case the intake efficiency, expressed either as isentropic efficiency η_i or

ram efficiency η_i, is independent of Mach number (up to a value of about 0.8) and it suffer from the drawback of implying zero stagnation pressure loss ($\Delta p_i/p = 0$) when $C_a = 0$. Under these conditions the average velocity in the intake is low, and the flow is accelerating, therefore the effect of friction is very small. According to the expressed above, it is possible to assume $C_a = 0$ for the SR-30 engine, because it is stationary and this implies it is under static condition. The stagnation pressure at the intake exit may be expressed as:

$$p_{01} = p_{0a} * \left(1 - \frac{\Delta p_i}{p}\right) \tag{4.4}$$

where $\Delta p_i/p$ is the loss of stagnation pressure in the intake and it will be assumed zero. Finally:

$$P_{01} = P_{0a} \tag{4.5}$$

The air mass flow $\dot{m}_a$ is calculated using the referred air mass flow from the compressor map:

$$\dot{m}_a = \left(\frac{\dot{m}_a * \sqrt{T_{01}}}{p_{01}}\right)_{cmap} * \frac{p_{01}}{\sqrt{T_{01}}}; \quad \text{(kg/s)} \tag{4.6}$$

$$\dot{m}_1 = \dot{m}_a; \quad \text{(kg/s)} \tag{4.7}$$

where $\dot{m}_1$ is the air mass flow which crosses the intake.

4.1.3 Compressor

Beta lines are used to facilitate loading a compressor map into an engine off design performance computer model [22]. Beta lines are drawn equi-spaced and parallel to the surge line, on the map.

Beta serves simply as an array address, and for a plot of pressure ratio versus flow. It avoids the problem of horizontal and vertical portions of constant speed lines. The map may be tabulated as shown in Figure 4–2 [50].

The engine off design performance can then use these tables to obtain consistent values of referred flow, pressure ratio and efficiency at given levels of referred speed and beta. The steps to follow in the compressor block calculations are:

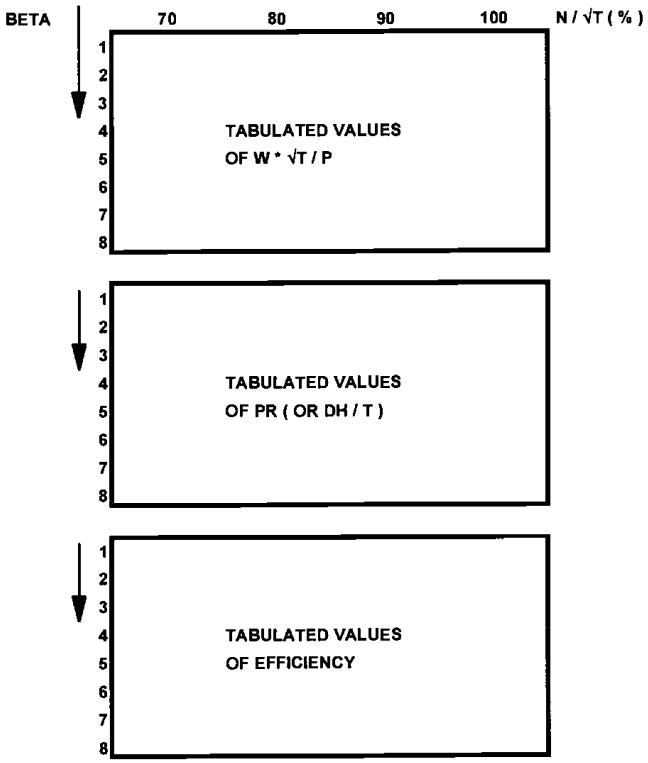

Figure 4–2: The compressor map and beta lines [50].

1. Assume an initial value for beta line and the referred speed:
2. Guess BETA.
3. Evaluate referred speed: $\frac{N}{\sqrt{T_{01}}}$

   where "N" will be between 50000 rpm and 90000 rpm which are the minimum and maximum values of rotational speed for operation on the SR-30 turbojet engine.
4. Look up the map with a referred speed and BETA:

$$\left(\frac{\dot{m}_a * \sqrt{T_{01}}}{p_{01}}\right)_{map} = f_{RF_c}\left(\frac{N}{\sqrt{T_{01}}}, BETA\right) \tag{4.8}$$

$$(PR_c)_{map} = f_{PR_c}\left(\frac{N}{\sqrt{T_{01}}}, BETA\right) \tag{4.9}$$

$$(\eta_c)_{map} = f_{\eta_c}\left(\frac{N}{\sqrt{T_{01}}}, BETA\right) \tag{4.10}$$

5. Scale FACTORs and DELTAs could be applied to the compressor map developed to align an engine off design performance model and test data. The following equations are obtained from reference [50]:

$$\left(\frac{\dot{m}_a * \sqrt{T_{01}}}{p_{01}}\right)_{cmap} = CF1 * \left(\frac{\dot{m}_a * \sqrt{T_{01}}}{p_{01}}\right)_{map} + DELTA1 \tag{4.11}$$

$$(PRc)_{cmap} = \{[(PRc)_{map} - 1] * CF3 + DELTA3\} + 1 \tag{4.12}$$

$$(\eta_c)_{cmap} = CF2 * (\eta_c)_{map} + DELTA2 \tag{4.13}$$

DELTAs, will be zero in the engine modeling. When the Kalman filter is applied, DELTAs will perform as deviation parameters, in order to adjust the model's results with the experimental data, and will vary with time.

6. Because there is no accumulation of fluid between the intake and the compressor, the continuity of flow is considered, then:

$$\dot{m}_2 = \dot{m}_1 \tag{4.14}$$

where $\dot{m}_2$ is the air mass flow across the compressor.

7. Evaluate exit stagnation pressure:

$$p_{02} = (PRc)_{cmap} * p_{01} \tag{4.15}$$

8. Evaluate exit stagnation temperature. The enthalpy-entropy diagram from Figure 3–2 and the correlations for the gas property calculations, from chapter three, are used. For an isentropic process:

$$\phi_{02ss} = \phi_{01} + R * ln(PRc)_{cmap} \tag{4.16}$$

where $\phi_{01} = f_\phi(T_{01})$ is obtained from equation 3.7, and R is the specific gas constant for dry air, which is, $R = 287.05\ J/kgK$, obtained from equation 3.1

$$T_{02ss} = T_{01} * e^{(\phi_{02ss} - \phi_{01})/c_p} \tag{4.17}$$

where c_p is the specific heat at constant pressure, which depends on the average temperature T_m. Also, $c_p = f(T_m)$ calculated from equation 3.2, and $T_m = (T_{02ss} + T_{01})/2$.

$$h_{02ss} = f_h(T_{02ss}) \tag{4.18}$$

$$h_{02} = h_{01} + \frac{h_{02ss} - h_{01}}{(\eta_c)_{cmap}} \tag{4.19}$$

$$T_{02} = f_T(h_{02}) \tag{4.20}$$

The calculation of the relation 4.20 is obtained from the inverse of equation 3.5.

9. The compressor power is:

$$PW_c = \dot{m}_2 * (h_{02} - h_{01}); \qquad \text{(kW)} \tag{4.21}$$

4.1.4 Combustor Calculations

The calculations for the combustor follows:

1. Guess $T_{03} = SOT$: where SOT is the stator outlet temperature, which is the temperature after a hypothetical complete mixing of the cooling air with the hot gas downstream of the turbine stator row.
2. Obtain efficiency from correlation versus loading [50]: Combustion efficiency is the ratio of fuel burnt in the combustor to the total fuel input. It may be correlated versus combustor loading as follows.

$$\begin{aligned} \eta_b = & -5.46974 * 10^{-11} * CL^5 + 3.97923 * 10^{-8} * CL^4 \\ & - 8.73718 * 10^{-6} * CL^3 + 0.000300007 * CL^2 \\ & - 0.004568246 * CL + 99.7 \end{aligned} \tag{4.22}$$

where CL is the combustor loading, it may be considered as a measure of the difficulty of the combustor design duty. It could be expressed with the correlation

obtained from Walsh & Fletcher [50]:

$$CL = \frac{\dot{m}_2}{VOL * P_{02}^{1.8} * 10^{0.0045*(T_{02}-400)}}; \qquad (kg/s\ atm^{1.8}\ m^3) \tag{4.23}$$

where $\dot{m}_2$ is the total air flow at compressor exit, VOL is the can volume (not including the outer annuli), as this reflects the entire combustion process, T_{02} and P_{02} are the stagnation (total) temperature and pressure respectively at the compressor exit and at inlet of the combustion chamber.

The obtained combustion efficiency, from equation 4.22, was corrected by multiplying a factor which depend on the rotational speed, as follows,

$$(\eta_b)_{corr} = CF4_{RPM} * \eta_b \tag{4.24}$$

where $CF4_{RPM}$ is the correction factor obtained from experiments.

3. Evaluate fuel-air ratio. The fuel-air ratio (FAR) is that required to transform unit mass of air at T_{02} and FAR kg of fuel at the fuel temperature T_f to $(1 + FAR)$ kg of products at T_{03} [46]. FAR may be calculated by:

$$FAR = \frac{h_{03} - h_{02}}{LHV * \eta_b} \tag{4.25}$$

where:

   * $h_{03} = f_{h_g}(T_{03})$; MJ/kg
   * $h_{02} = f_{h_a}(T_{02})$; MJ/kg
   * η_b is the combustion efficiency described above.
   * LHV is the lower heating value.

   LHV does account the latent heat of vaporization of liquid water and hence is the parameter most commonly used for gas turbine performance calculations.

4. Evaluate fuel flow:

$$\dot{m}_f = FAR * \dot{m}_2; \qquad (kg/s) \tag{4.26}$$

where $\dot{m}_2$ is the air mass flow at the inlet of combustion chamber.

5. Evaluate exit gas flow $\dot{m}_3$ by adding fuel flow to inlet air flow:

$$\dot{m}_3 = \dot{m}_2 + \dot{m}_f; \qquad (kg/s) \tag{4.27}$$

6. Evaluate the stagnation pressure at combustor exit p_{03}:

$$p_{03} = p_{02} * \left(1 - \frac{\triangle P_b}{p_{02}}\right); \qquad \text{(kPa)} \tag{4.28}$$

where:

$$\frac{\Delta p_b}{p_{02}} = PLF * \frac{R}{2}\left(\frac{\dot{m}_2\sqrt{T_{02}}}{A_{mc}p_{02}}\right)^2 \tag{4.29}$$

and,

$$PLF = \frac{p_{02} - p_{03}}{\dot{m}_2^2/2\rho_2 A_{mc}^2} \tag{4.30}$$

where PLF is the pressure loss factor, R is the specific gas constant for the dry air, A_{mc} is the maximum cross-sectional area of the chamber, ρ_2 is the static density at combustor inlet, its difference with the stagnation density ρ_{02} is ignored because the flow velocity at that point is low.

Combustion chamber pressure loss is due to two distinct causes:

i. Skin friction and turbulence.

ii. The rise in temperature due to combustion.

4.1.5 Turbine

The axial turbine, in the SR-30 engine, extracts power from gas stream to drive the compressor.

The turbine map for SR-30 engine, generated to define its performance under all off design conditions, was obtained in chapter three. Capacity (referred flow) and

efficiency were plotted for lines of constant referred speed versus the work parameter (dH/T or $CP.dT/T$ as shown in Figures 3–25 and 3–26).

Figure 4–3 shows the two tables, obtained from the turbine map developed, which are loaded into the engine off design performance model. And the calculations follow.

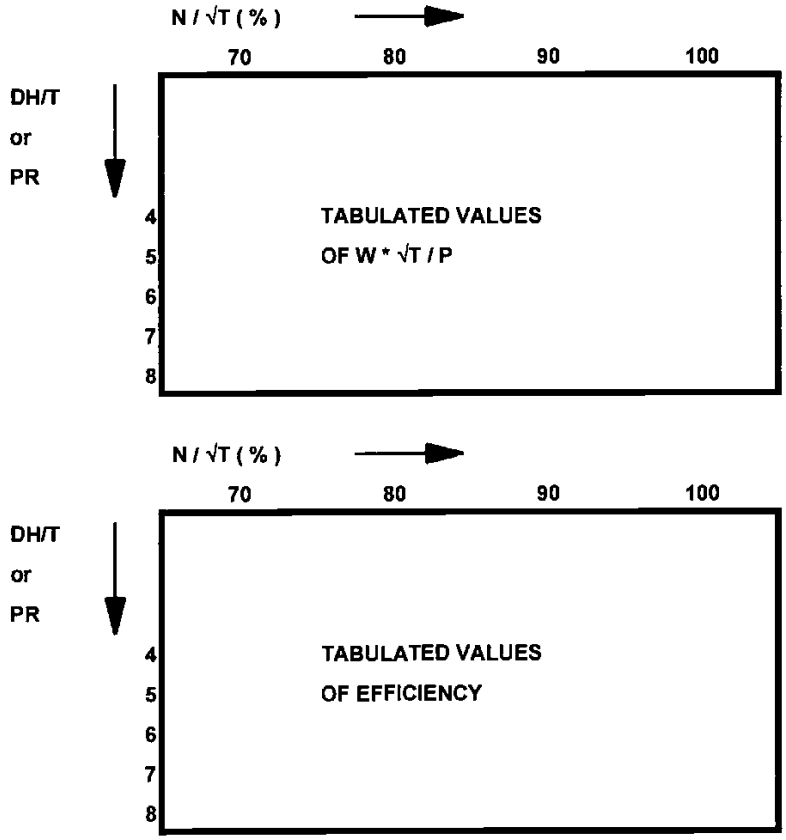

Figure 4–3: Turbine map representation [50].

1. Power loss. The shaft power of SR-30 engine is lost due to friction and windage. Windage losses is due to the frictional work done on air between the rotating compressor or turbine disc and a static structural member. Windage losses were already included in the compressor and turbine efficiency through the development of their characteristic maps, therefore, only the frictional losses will be considered here.

Frictional losses in the SR-30 are due to the friction torque in the ball bearing. It can be determined by the equation obtained from Sabitov et al. [56]:

$$PWloss = N_b * f_g * 10^{-8}(\nu_{oil} * N)^{2/3} * d_0^3; \qquad \text{(kW)} \tag{4.31}$$

where N_b is the number of bearings, f_g is the coefficient which depend on the type of bearing, d_0 is the pitch circle diameter of the bearing, N is the rotational velocity and ν_{oil} is the kinematic viscosity of the oil (equal to 5 cst).

Oils used for gas turbine engines fall into two major categories: mineral oils and synthetic oils. Synthetic oils are used almost exclusively in gas generators, as is the case of SR-30 engine, due to their vastly higher auto-ignition temperature.

2. Shaft mechanical efficiency:

$$\eta_m = 100 * \frac{PW_c}{PW_c + PW_{loss}} \tag{4.32}$$

where PW_c is the compressor output power and PW_{loss} is the power loss.

Correction factor $CF5_{RPM}$ was introduced into the equation 4.32 to improve the results of mechanical efficiency, as follow:

$$(\eta_m)_{corr} = CF5_{RPM} * \eta_m \tag{4.33}$$

At steady state, the following relation is fulfilled:

$$PW_t = \frac{PW_c}{\eta_m} \tag{4.34}$$

Where $PW_t = \dot{m}_3 * (h_{03} - h_{04})$ and $PW_c = \dot{m}_2 * (h_{02} - h_{01})$, so we can get h_{04} from equation (4.34):

$$h_{04} = h_{03} - \frac{PW_c}{\eta_m * \dot{m}_3} \tag{4.35}$$

3. The exit stagnation temperature T_{04} can be obtained, by equation , as follow:

$$T_{04} = f_T(h_{04}); \qquad {}^\circ K \tag{4.36}$$

4. Evaluate work parameter DH/T. Because the turbine map was developed such that the capacity and efficiency were plotted for lines of constant referred speed versus the work parameter, in this calculation, it will be used the work parameter is used of instead of expansion ratio (either one could be used in other cases).

$$\frac{DH}{T} = \frac{h_{03} - h_{04}}{T_{03}}; \qquad kJ/kg\,^\circ\mathrm{K} \tag{4.37}$$

5. Evaluate referred speed: $\frac{N}{\sqrt{T_{03}}}$
6. Taking into account the work parameter and referred speed, look up the turbine map for referred flow (capacity) $\left(\frac{\dot{m}_3\sqrt{T_{03}}}{p_{03}}\right)_{map}$ and efficiency η_{map}:

$$\left(\frac{\dot{m}_3\sqrt{T_{03}}}{p_{03}}\right)_{tmap} = f_{RF_t}\left(\frac{DH}{T}, \frac{N}{\sqrt{T_{03}}}\right); \tag{4.38}$$

$$(\eta_t)_{tmap} = f_{\eta_t}\left(\frac{DH}{T}, \frac{N}{\sqrt{T_{03}}}\right) \tag{4.39}$$

Additionally, apply scale FACTORs and DELTAs if required to a turbine map, similar to the compressor map. These adjustiments will be used to align the SR-30 engine off design performance model with the test data:

$$\left(\frac{\dot{m}_3\sqrt{T_{03}}}{p_{03}}\right)_{ctmap} = CF6 * \left(\frac{\dot{m}_3\sqrt{T_{03}}}{p_{03}}\right)_{tmap} + DELTA1 \tag{4.40}$$

$$(\eta_t)_{ctmap} = CF7 * (\eta_t)_{tmap} + DELTA2 \tag{4.41}$$

In the same way as for the compressor, DELTAs, will be zeros in this calculation, and it will be considered as deviation parameters when implementing the Kalman filter.

7. Next we have to calculate capacity from gas path parameters resulting from earlier guesses of BETA and SOT: matching the constraint value of $\dot{m}\sqrt{T}/p$

$$Q_{tcal} = \left(\frac{\dot{m}_3\sqrt{T_{03}}}{p_{03}}\right)_{cal}; \qquad (kg\sqrt{K}/s\,kPa)$$

8. Compare map and calculated values and re-guess SOT. If $Q_{tmap} = \left(\frac{\dot{m}_3\sqrt{T_{03}}}{p_{03}}\right)_{tmap}$, the error may be expressed as:

$$Error = \frac{Q_{tcal} - Q_{tmap}}{Q_{tmap}} * 100 \tag{4.42}$$

9. New guess:

$$T_{03new} = T_{03old} * \left(\frac{Q_{tmap}}{Q_{tcalc}}\right)^2; \qquad (^\circ K) \tag{4.43}$$

After calculating T_{03new}, we have to recalculate: FAR, $\dot{m}_f$, $\dot{m}_3$, T_{04}, Q_{tmap}, and Q_{tcal}.

This iteration loop should be repeated until $error < 0.05\%$

10. Evaluate stagnation exit pressure, P_{04}. First look up the turbine efficiency from the tabulated form of the map as shown in Figure 4–3, with the work parameter DH/T_{03} and referred speed $N/\sqrt{T_{03}}$, previously calculated, as it is expressed by relation 4.39.

Then obtain the pressure ratio:

$$PR_t = \frac{1}{\left[1 - \frac{T_{03}-T_{04}}{(\eta_t)_{tmap} * T_{03}}\right]^{\left(\frac{\gamma}{\gamma-1}\right)}} \tag{4.44}$$

Now evaluate the exit pressure:

$$p_{04} = \frac{p_{03}}{PR_t}; \qquad \text{kPa} \tag{4.45}$$

11. The mass flow from conservation of mass:

$$\dot{m}_4 = \dot{m}_3; \qquad \text{kg/s} \tag{4.46}$$

Also apply Reynolds number (Re) corrections to map values to the turbine map:

$$(\eta_t)_{tmap} = 1 - \frac{1 - (\eta_t)_{map}}{\left(\frac{Re}{Re_{critical}}\right)^{k_1}} \tag{4.47}$$

$$Q_{tmap} = Q_{map} * \left[1 - \frac{k_2 * (\eta_{tmap}) - \eta_t}{\eta_{tmap}}\right] \tag{4.48}$$

$$\tag{4.49}$$

where:

$$Re = \frac{\dot{m}_3 * C_4}{A_t * \nu_4}$$

$$k_1 = 0.05 - 0.25$$

$$k_2 = 0.4 - 0.6$$

where $\dot{m}_3$ is the mass flow of the working fluid at turbine inlet; C_4 is the exit annulus height; A_t is the average cross section area of the turbine; ν_4 is the viscosity of the working fluid and $Re_{critical}$ is the critical Reynolds number, which is around 1×10^5.

4.1.6 Propelline Nozzle

The propelling nozzle is the component in which the working fluid is expanded to give a high velocity jet. SR-30 engine uses a convergent nozzle. The nozzle could operate in chocked or un-chocked conditions. Figure 4–4, modified from Dixon [22], illustrates the real and isentropic processes on the enthalpy-entropy (h-s) Mollier diagram. It shows the expansion proceeding from state 4 to state 5. The corresponding calculations follow:

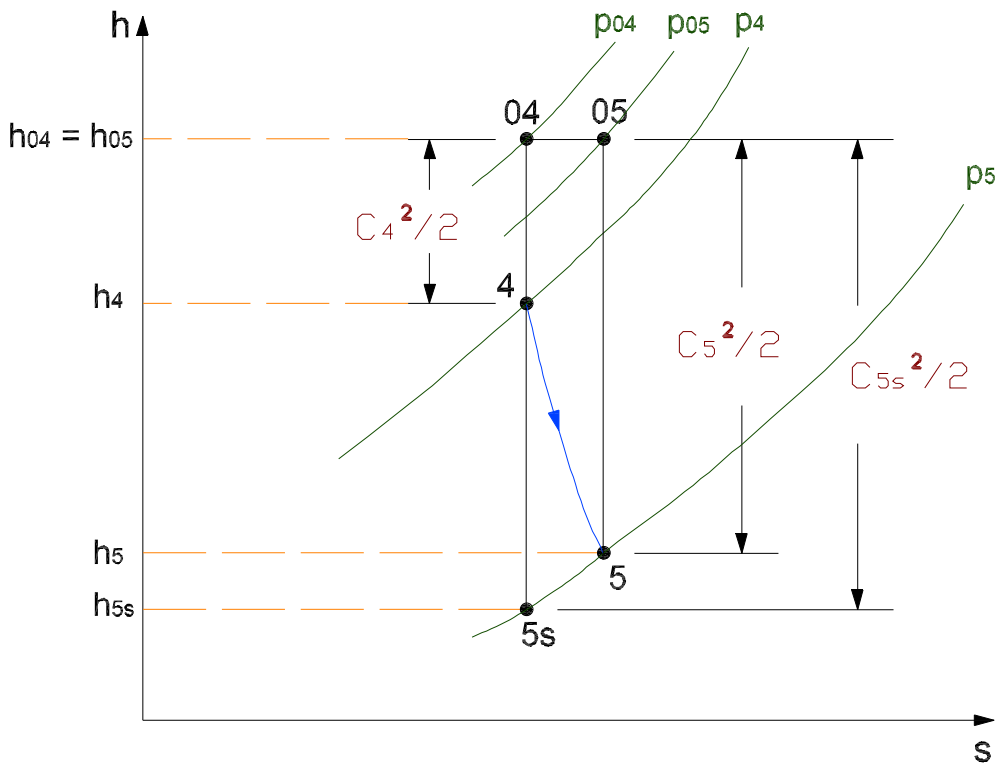

Figure 4–4: Mollier diagram for the complete centrifugal compressor stage.

- From previous considerations, It is assumed that the process is adiabatic with no work transfer [46], and thus:

$$h_{05} = h_{04} \tag{4.50}$$

$$T_{05} = T_{04} \tag{4.51}$$

By conservation of mass flow:

$$\dot{m}_5 = \dot{m}_4 \tag{4.52}$$

The fuel air ratio (FAR) is homogeneous, constant and equal to that calculated for the combustion process.

$$R = f_R(FAR) \tag{4.53}$$

- Evaluate exit stagnation pressure p_{05}:

$$p_{05} = p_{04} * \left[1 - \frac{\Delta p_n}{p_{04}}\right] \tag{4.54}$$

where:

$$\frac{\Delta p_n}{p_{04}} = k_{45} * \left(\frac{\dot{m}_4\sqrt{T_{04}}}{p_{04}}\right)^2 \tag{4.55}$$

where k_{45} is the pressure loss coefficient obtained from experiment.

- Evaluate critical temperature T_c and critical pressure p_c: It is necessary to assume a value for the nozzle efficiency η_N:

$$T_c = \frac{2T_{04}}{\gamma + 1} \tag{4.56}$$

$$p_c = p_{04}\left[1 - \frac{1}{\eta_N}\left(1 - \frac{T_c}{T_{04}}\right)\right]^{\frac{\gamma}{\gamma-1}} \tag{4.57}$$

- Evaluate nozzle pressure ratio, (PR_n):

$$PR_n = \frac{p_{04}}{p_5} \tag{4.58}$$

If $\frac{p_{04}}{p_{amb}} \geq \frac{p_{04}}{p_c}$ then $\frac{p_{04}}{p_5} = \frac{p_{04}}{p_c}$, in other case $\frac{p_{04}}{p_5} = \frac{p_{04}}{p_{amb}}$, the relations for each cases are:

a.- For choked propelling nozzle, $(M_5 = 1)$ therefore $p_5 = p_c$:

$$PR_n = \frac{p_{04}}{p_c} \tag{4.59}$$

also:

$$p_5 = p_c \tag{4.60}$$

$$T_5 = T_c \tag{4.61}$$

$$\rho_5 = \frac{p_5}{R_g * T_c} \tag{4.62}$$

$$C_5 = M_5 * \sqrt{\gamma R_g T_c} \tag{4.63}$$

where ρ_5 is the static density at the nozzle exit, p_5 is the static pressure at nozzle exit, C_5 is the absolute flow velocity at nozzle exit and M_5 is the exit Mach number at the nozzle exit.

From the design point performance parameters we can get the exit effective area A_{5ef} for the mainstream flow is obtained:

$$A_{5ef} = \frac{\dot{m}_5}{\rho_5 C_5} \tag{4.64}$$

b.- For unchoked propelling nozzle, $(M < 1)$ therefore $p_5 = p_{amb}$:

The following relationships are fulfilled to obtain T_5 and h_5:

$$\phi_5 = \phi_{05} - R_g * ln\left(\frac{p_{05}}{p_5}\right); \qquad \text{kJ/kg} \tag{4.65}$$

where:

$$\phi_{05} = f_\phi(T_{05}) \tag{4.66}$$

then:

$$T_5 = f_T(\phi_5); \qquad \text{K} \tag{4.67}$$

$$h_5 = f_h(T_5); \qquad \text{K} \tag{4.68}$$

The nozzle exit velocity is:

$$C_5 = \sqrt{2(h_{04} - h_5)} \tag{4.69}$$

The effective nozzle area is:

$$A_5 = \frac{\dot{m}_5}{\rho_5 \ C_5} \tag{4.70}$$

Where the density.

– The effective geometric area A_{5eff} is:

$$A_{5eff} = CD_{RPM} * A_{5geo} \tag{4.71}$$

where A_{5geo} is the geometric area, obtained from the nozzle of the SR-30 engine; C_D is a discharge coefficient.

For a good design with low cone angle and diameter ratio and the likely design point expansion ratio of $2:1$ to $4:1$ C_D varies between 0.95 and 0.97 [50]. However, in this work, C_D was obtained from matching the model results in steady state with experimental data at different rotational speeds.

– Evaluate matching constraint value of nozzle:

$$Error = \left\| \frac{A_5 - A_{5eff}}{A_{5eff}} \right\| * 100; \qquad \% \tag{4.72}$$

– Re-guess BETA:

$$BETA_{new} = BETA_{old} * \left(\frac{A5eff}{A_5} \right)^{1/6} \tag{4.73}$$

Equation 4.73 was found in this work to make the convergence process for the steady state performance. It was observed that a exponent higher than $1/6$ impedes the convergence process.

The calculation process now goes back where the compressor map is looked up and the process is repeated until the error in the effective area at nozzle exit is $< 0.05\%$. The compressor map will be linearly interpolated with the new value of BETA.

4.1.7 Final Calculations

Once the previous iteration converges the final calculations follow:

- The momentum drag is:

$$F_D = \dot{m}_a * C_a; \qquad \text{kN} \tag{4.74}$$

- Evaluate gross thrust as the sum of momentum thrust and pressure thrust:

  If $p_5 = p_c$;

$$F_G = \dot{m}_5 * C_5 * C_X + (p_5 - p_a) * A_{5geo}; \qquad \text{kN} \qquad (4.75)$$

  In other case if $p_5 = p_a$;

$$F_G = \dot{m}_5 * C_5 * C_X; \qquad \text{kN} \qquad (4.76)$$

  where C_X is the coefficient of thrust. C_X take into account that the actual velocity (C_{5act}) is slightly lower than that calculated C_5 as there is some friction and flow non-uniformity. This value was found through matching the model results and experimental data in steady state performance.

- Net thrust:

$$F_N = F_G - F_D; \qquad \text{kN} \qquad (4.77)$$

- Specific net thrust:

$$SFN = \frac{F_N}{\dot{m}_a}; \qquad \text{N s/kg} \qquad (4.78)$$

- Specific fuel consumption:

$$SFC = 3600 * \frac{\dot{m}_f}{F_N}; \qquad \text{kg/N h} \qquad (4.79)$$

4.2 Transient Performance

Transient performance deals with the operating regime where engine performance parameters are changing with time. There are some considerations here:

a. Because the inter-component volumes are not so large in the SR-30 engine, the volume dynamics will be neglected. This implies that the pressure, temperature and hence density of the fluid will not change with time.

b. During transient operation there are significant net heat fluxes between the working fluid and the engine metal. This net heat transfer from the working fluid to the metal is termed heat soakage. In the SR-30 engine, Heat soakage, may have the largest effect in the combustor. But this could be neglected because the model does not take into account the abrupt change of operating conditions from idle to full power. Heat soakage, also could be neglected in the combustor due to its small surface area, thermal mass and temperature change (because it operate only from 50000 rpm to 90000 rpm).

c. And, the model neglects the effects of tip clearance change and combustion delay.

The iterative method was used to calculate the transient state of the engine.

The spool acceleration rate is:

$$\frac{dN}{dt} = \frac{DPW}{J * N * (\frac{2\pi}{60})^2}; \qquad rpm/s \tag{4.80}$$

where:

$$DPW = PW_t - \frac{PW_c}{\eta_m} \tag{4.81}$$

J is the moment of inertia, N is the rotational speed and $(\frac{2\pi}{60})^2$ is a conversion factor.

The BogackiShampine method was chosen, from Simulink/Matlab software [32], as the numerical solution of the differential equation for the spool acceleration rate. The BogackiShampine method is a third order RungeKutta method. It has an embedded second-order method which can be used to implement the adaptive step size.

4.3 Matching the Steady State Model With Transient State

Fig. 4–5 shows the complete flow chart for the calculations described in this chapter. The flow chart shows the nested iteration loops used for the nonlinear SR-30 engine model. The core of the simulation is in fact the steady state performance

model, run to specified speeds. The simulation initializes at 50000 rpm. At this operating speed the steady state model runs two iteration loops, which are:

1. First iteration loop; in which the parameter guessed is the Outlet Stator Temperature (SOT) which is equal, in this case, to the Turbine Inlet Temperature (TIT or T_{03}. The constraint is that the calculated flow capacity must be compared to the capacity obtained from the turbine map, the error may be calculated with the equation 4.42. T_{03} should be actualized with equation 4.43 for convergence process.
2. Second iteration loop; in which the non-physical parameter guessed is $BETA$. The constraint is the effective area at nozzle exit according to equation 4.72. The convergence process, to actualize BETA, is done by equation 4.73.

When fuel is incremented the model is switched in transient mode. A third iteration loop is done here, in which the parameter guessed is the unbalanced power. The constrain is the fuel flow set externally. When the calculated fuel flow, from steady state model, is close enough to the fuel flow set externally then the unbalanced power (DPW), calculated from equation 4.81, will tend to zero, this means that the model is in steady state. And, when the calculate fuel flow is very different to that set externally, due to rising fuel, then DPW will tend to be different from zero, this means the model is in transient state.

Correction factors were applied to the model, but these will be discussed in the following chapter, because they are obtained performing the matching between the model results and the experimental data.

4.4 Implementing the Model in Simulink

The engine modeling was performed in Matlab/simulink environment. Figure 4–6 shows the overall model which implements these calculation using the Simulink environment.

In order to load the component maps into the engine simulation, the blocks "Lookup Table (2-D)" was used. For the compressor map, the input for row index input values parameter is $BETA$, referred speed is introduced into the "column index input values parameter" and tabulated form of $BETA$ vs referred speed is introduced into the "table data input". For the turbine map, the work parameter and the referred speed are used as input parameters and the tabulated form is used for the table data input.

A variable-step continuous solver was chosen to solve the differential equation of the spool acceleration rate, which dynamically varies the step size during the simulation. This solver is the Bogacki−Shampine method (or ode23 solver) which increases or reduces the step size using its local error control to achieve the tolerances that was specified (min step size = 0.189 and max step size = 0.2 were used). The Bogacki−Shampine method was chosen as the numerical solution of the differential equation for the spool acceleration rate due to the better results obtained. Computing the step size at each time step adds to the computational overhead but can reduce the total number of steps, and the simulation time required to maintain a specified level of accuracy. The Bogacki−Shampine method can be more efficient than higher order solver, such as ode45, at crude error tolerances and in the presence of mild stiffness. This solver provides accurate solutions for "free" by applying a cubic Hermite interpolation to the values and slopes computed at the ends of a step.

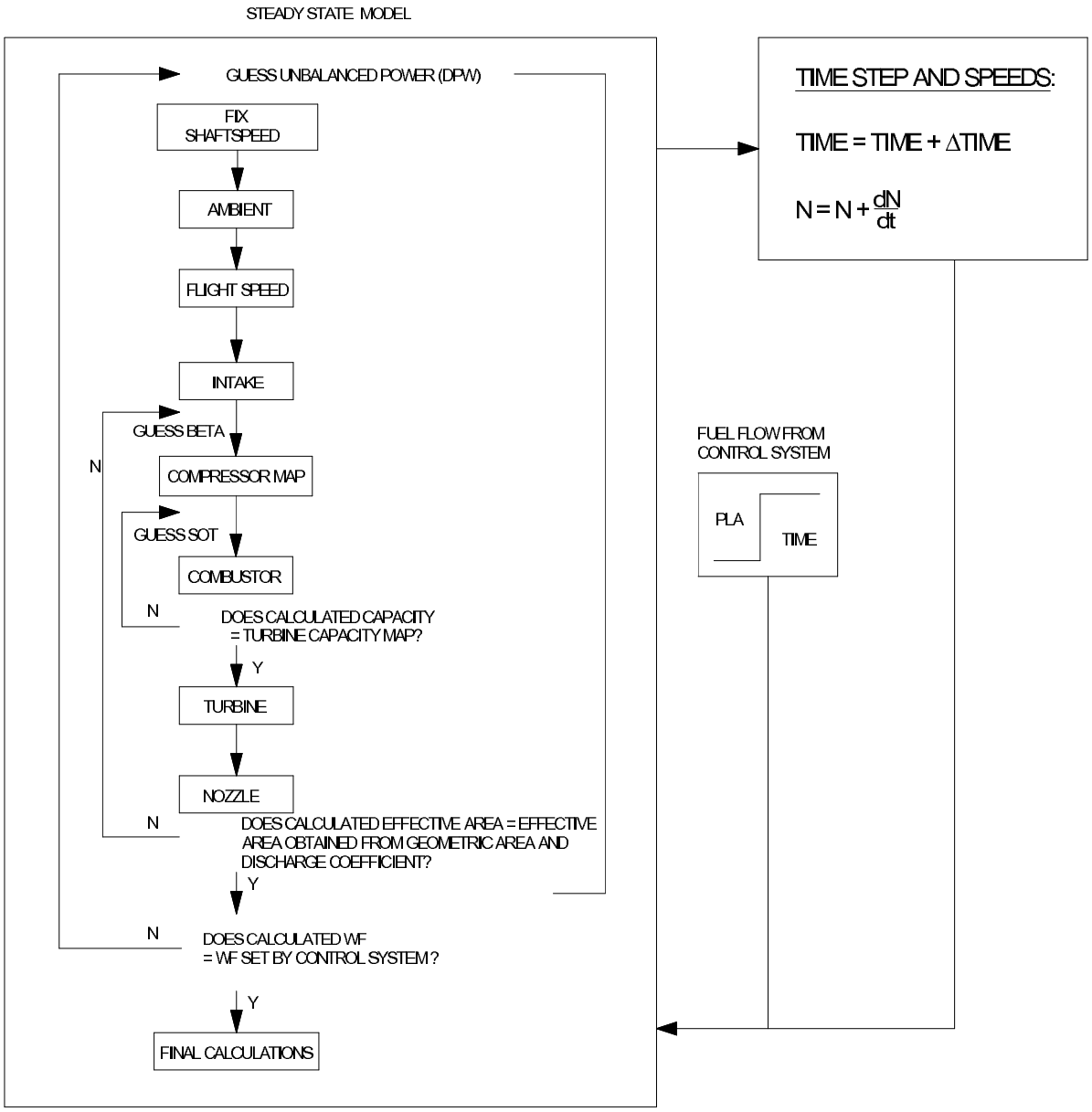

Figure 4–5: Flow diagram of the SR-30 gas turbine simulation.

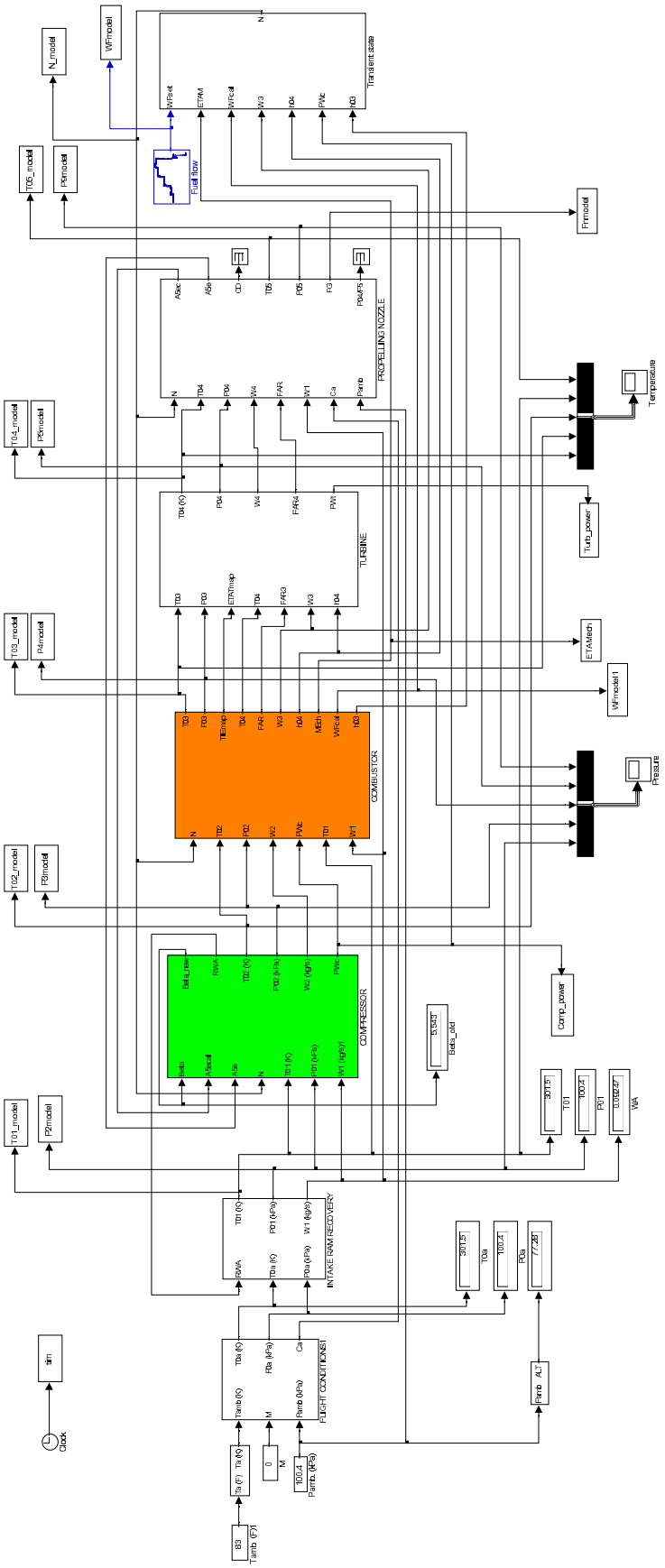

Figure 4–6: SR-30 gas turbine simulation.

CHAPTER 5
EXPERIMENTAL VALIDATION

The SR-30 turbojet engine, shown in Figure 5–1, is designed and manufactured by Turbine Technologies. The compact engine features a centrifugal flow compressor, reverse flow annular combustor and an axial flow turbine stage. The SR-30 follows the fundamental gas turbine cycle: Ambient air enters the engine through the bell shaped inlet. The air is then compressed, diffused and directed into the combustor can. Kerosene based fuel, introduced via six high-pressure atomization nozzles, is mixed with the compressed air and ignited. Heated combustion gas expands and accelerates through the vane guide ring causing the turbine to rotate. Useful work is extracted from this rotation as the turbine powers the compressor. The combustion gases are further accelerated through the thrust nozzle where the remaining heat energy is converted to kinetic energy in the form of jet thrust. The ejected gas returns to ambient atmospheric conditions thereby completing the thermodynamic cycle. The SR-30 engine will be tested under both steady state conditions and transient conditions in order to refine and validate the mathematical model presented in the previous chapters.

5.1 Kerosene

SR-30 engine uses kerosene based fuel. Kerosene is a faction of crude oil primarily comprising a band of hydrocarbons with an average composition of $C_{12}H_{23.5}$ and molecular weight of 167.7. There are a number of commercial grades available such as JP-4, JP-5 and JP-8 (Jet A-1).

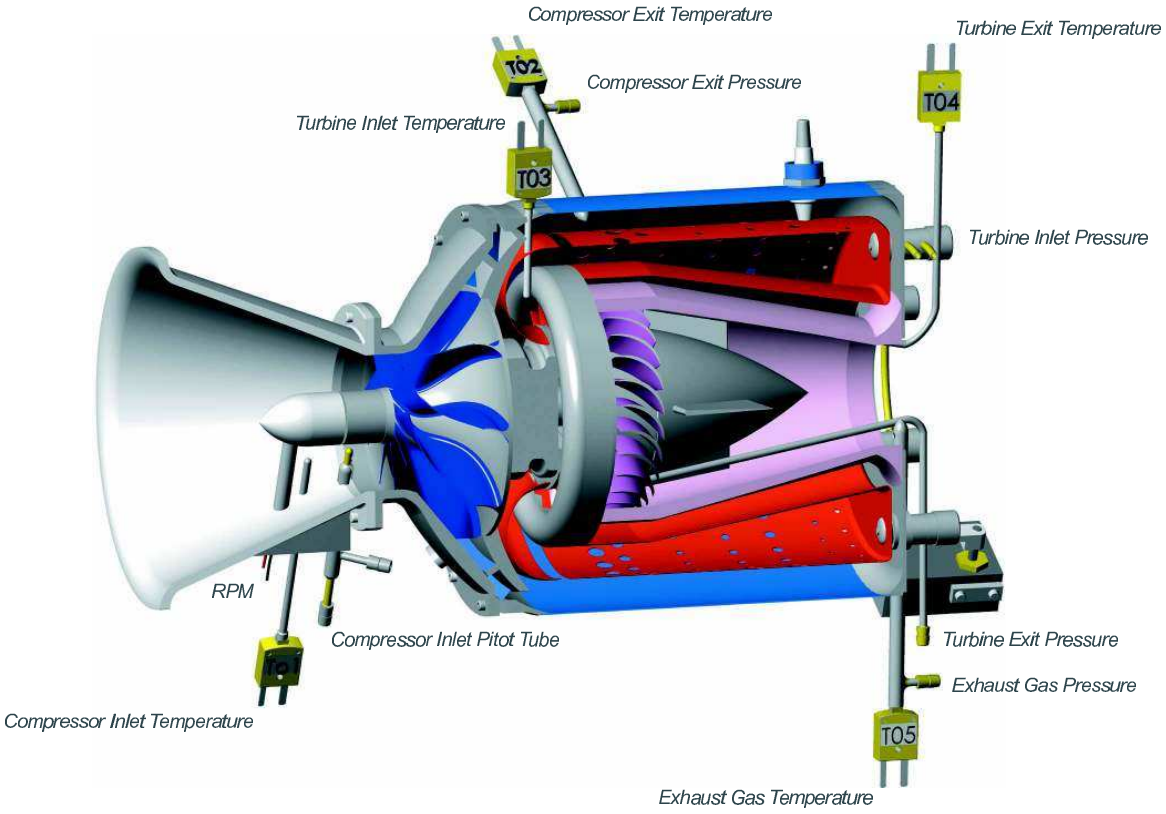

Figure 5–1: SR-30 Turbojet Engine [48].

Table 5–1 lists the various types of jet fuel available that can be used. It also shows the density and the lower heating value (LHV) used in test data analysis.

Commercial grade Jet A-1 fuel was used in the in the validation experiments.

Table 5–1: Typical Jet Fuel Properties

Property	**Military/Commercial Kerosene**			**Low Temp Diesel**		**Military Diesel**
	JP-4 (Jet B)	JP-5	JP-8 (Jet A/Jet A-1)	DL-1	DL-2	F-54
Density kg/lt	0.755	0.817	0.797	0.812	0.852	0.830
Lower Heating Value (kJ/kg)	43571	42929	43008	43219	42917	42851

5.2 Lubricating oil

The approved oil for the SR-30 engine is MIL-PRF-23699F-STD [57]. This class of oil is a standard (Non-Corrosion inhibiting) synthetic oil. The kinematic viscosity is 4.9 to 5.4 centistokes (cst) for 100 °C, and 23 cst for −40 °C.

5.3 Intake

The SR-30 engine under study is in static conditions, that means, that its intake acts as a nozzle, in which the air accelerates from zero velocity (C_a) to C_1 at the compressor inlet.

According to Cohen et al. [46], when the compressor is part of a stationary gas turbine, having a short intake fairing that can be regarded as part of the compressor, both the isentropic efficiency η_i and the ram recovery factor η_r suffer equally from the drawback of implying zero stagnation pressure loss when the velocity of the ambient air C_a, is zero. That is P_{01} and T_{01} will be equal to P_{amb} and T_{amb} respectively and $p_{amb} = p_{0a}$, as seen in figure 5–2.

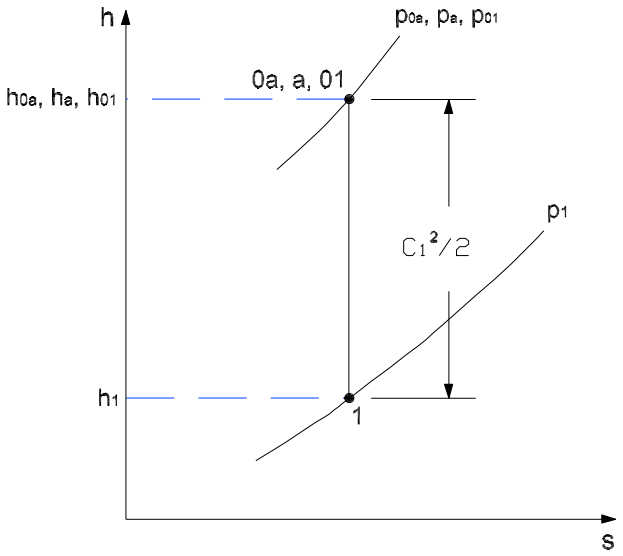

Figure 5–2: Mollier diagram for the flow process through the SR-30 intake.

The parameters used in the off design performance model, are:

- Inlet total loss:

$$\begin{aligned} \frac{\Delta p_i}{p_{0a}} &= \frac{p_{0a} - p_{01}}{p_{0a}} \\ &= 0 \end{aligned} \tag{5.1}$$

- Pressure loss coefficient:

$$k_{a1} = \frac{\left(\frac{p_{0a}-p_{01}}{p_{0a}}\right) * 100}{\left(\frac{\dot{m}_a\sqrt{T_{0a}}}{p_{0a}}\right)^2} \tag{5.2}$$

From the test bed, at the compressor inlet, we can measure the dynamic pressure d_p and the static temperature T_1, with this values we can find the static pressure p_1 and the stagnation temperature T_{01} making use of the next equations:

$$p_1 = p_{01} - d_p; \qquad kPa \tag{5.3}$$

$$T_{01} = T_1 + \frac{C_1^2}{2\ c_p}; \qquad K \tag{5.4}$$

With this the density ρ_1 and the velocity at compressor inlet C_1 are calculated:

$$\rho_1 = \frac{p_1 * 1000}{R * T_1}; \qquad kg/m^3 \tag{5.5}$$

$$C_1 = \sqrt{\frac{2000\ \gamma\ p_1}{\rho_1(\gamma - 1)}\left[\left(\frac{d_p}{p_1} + 1\right)^{\frac{\gamma-1}{\gamma}} - 1\right]}; \qquad m/s \tag{5.6}$$

The area A_1 at the compressor inlet can be obtained from:

$$A_1 = \frac{\pi(d_t^2 - d_r^2)}{4}; \qquad m^2 \tag{5.7}$$

where d_t is the tip diameter and d_r is the root diameter, both referring to the impeller eye.

Then the air mass flow is calculated from the continuity equation, as follow:

$$\dot{m}_a = \rho_1\ C_1\ A_1; \qquad kg/s \tag{5.8}$$

Then, the mass flow at the compressor inlet is:

$$\dot{m}_1 = \dot{m}_a \tag{5.9}$$

5.4 Compressor

In the compressor, we can find two important performance parameters, the isentropic efficiency and the compressor power.

- The isentropic efficiency is defined as:

$$\eta_c = \frac{h_{02ss} - h_{o1}}{h_{02} - h_{01}} \tag{5.10}$$

From the experimental data the stagnation (or total) temperatures at the compressor inlet T_{01} and the compressor outlet T_{02} are obtained. The stagnation enthalpies $h_{01} = f_h(T_{01})$ and $h_{02} = f_h(T_{02})$ are determined.

The stagnation pressure p_{02} is found adding the gauge pressure at compressor exit p_{g2}, measured directly, and the atmospheric pressure p_{amb}, as follow:

$$p_{02} = p_{amb} + p_{g2}; \qquad \text{kPa}; \tag{5.11}$$

Then the pressure ratio is:

$$PR_c = \frac{p_{02}}{p_{01}} \tag{5.12}$$

To find the enthalpy h_{02ss} which would have been reached after an isentropic ram compression to p_{02}, equations 3.5, 3.7 and the Mollier diagram of the compressor

are used in the following relations:

$$\phi_{01} = f_\phi(T_{01}); \qquad kJ/kg\ K \tag{5.13}$$

$$\phi_{02ss} = \phi_{01} + R * ln\left(\frac{p_{02}}{p_{01}}\right); \qquad kJ/kg\ K \tag{5.14}$$

$$T_{02ss} = f_T(\phi_{02ss}); \qquad K \tag{5.15}$$

$$h_{02ss} = f_h(T_{02ss}); \qquad kJ/kg\ K \tag{5.16}$$

- By conservation of mass, the air mass flow at the compressor exit $\dot{m}_2$, is:

$$\dot{m}_2 = \dot{m}_1 \tag{5.17}$$

- The compressor output power is:

$$PW_c = \dot{m}_2(h_{02} - h_{01}); \qquad kW \tag{5.18}$$

5.5 Combustor

The heat released by the fuel, $\dot{Q}_{in}$, is the amount of energy input into the engine. It can be found by multiplying the lower heating value (LHV) of the fuel and the mass flow rate of the fuel ($\dot{m}_f$) entering the combustor chamber.

$$\dot{Q}_{in} = \dot{m}_F * LHV; \qquad kW \tag{5.19}$$

The combustion efficiency is:

$$\eta_b = \frac{(\dot{m}_3) * h_{03} - \dot{m}_a * h_{02}}{\dot{Q}_{in}} \tag{5.20}$$

where $\dot{m}_3$ is the total mass flow rate leaving the combustor, which is:

$$\dot{m}_3 = \dot{m}_a + \dot{m}_f \tag{5.21}$$

The fuel air ratio is:

$$FAR = \frac{\dot{m}_f}{\dot{m}_a} \tag{5.22}$$

It is nessary to obtain the pressure loss coefficient (or pressure loss factor, PLF) for the combustor of SR-30 engine, in order to use it in the off-design performance model. The PLF may be calculated using the equation obtained from Cohen et al. [46].

$$\begin{aligned} PLF &= \frac{p_{02} - p_{03}}{\dot{m}_2^2 / 2\rho_2 A_{mc}^2} \\ &= K_{cold} + K_{hot}\left(\frac{T03}{T02} - 1\right) \end{aligned} \tag{5.23}$$

where the denominator is a conventional dynamic head based on a velocity calculated from the inlet density, air mass flow $\dot{m}_a$, and maximum cross-sectional area A_{mc} of the chamber through which the gas flow passes. The difference between the static density ρ_2 and the stagnation density ρ_{02} can be ignored because the velocity at the inlet of the combustion chamber is low; then the density can be calculated as a function of total pressure and total temperature as follows,

$$\rho_2 \approx \rho_{02} = \frac{p_{02} * 1000}{R\ T_{02}}; \qquad kg/m^3 \tag{5.24}$$

The cold loss factor K_{cold} and the hot loss factor K_{hot} are calculated from the combustion chamber on a test rig from a cold run and a hot run as follows,

$$K_{cold} = \frac{\frac{\Delta p_{cold}}{p_{02}}}{\left(\frac{W_2\sqrt{T_{02}}}{p_{02}}\right)^2} \tag{5.25}$$

$$K_{hot} = \frac{\frac{\Delta p_{hot}}{p_{02}}}{\left(\frac{T_{03}}{T_{02}} - 1\right)\left(\frac{W_2\sqrt{T_{02}}}{p_{02}}\right)^2} \tag{5.26}$$

5.6 Turbine

- The turbine isentropic efficiency is defined as:

$$\eta_t = \frac{h_{03} - h_{04}}{h_{03} - h_{04ss}} \tag{5.27}$$

Where the stagnation enthalpies are obtained through equation 3 with the relations:

$$h_{03} = f_h(T_{03}, FAR); \qquad kJ/kg \tag{5.28}$$

$$h_{04} = f_h(T_{04}, FAR); \qquad kJ/kg \tag{5.29}$$

The stagnation temperatures T_{03} and T_{04} are measured from the SR-30 test bed. Also from test bed we can measure the gauge pressures at the turbine inlet p_{g3} and the turbine outlet p_{g4}, therefore the corresponding stagnation pressures are found from:

$$p_{03} = p_{amb} + p_{g3}; \qquad kPa \tag{5.30}$$

$$p_{04} = p_{amb} + p_{g4}; \qquad kPa \tag{5.31}$$

In order to calculate the efficiency, h_{04ss} is calculated using the relations:

$$\phi_{04ss} = \phi_{03} - R\ ln\left(\frac{p_{03}}{p_{04}}\right); \qquad kJ/kg \tag{5.32}$$

$$\phi_{03} = f_\phi(T_{03}); \qquad kJ/kg \tag{5.33}$$

$$T_{04ss} = f_T(\phi_{04ss}); \qquad K \tag{5.34}$$

$$h_{04ss} = f_h(T_{04ss}); \qquad kJ/kg \tag{5.35}$$

- The gas flow, by virtue of the law of conservation of mass, is:

$$\dot{m}_4 = \dot{m}_3 \tag{5.36}$$

- The power output is:

$$PW_t = \dot{m}_3(h_{03} - h_{04}); \qquad kW \tag{5.37}$$

$$\tag{5.38}$$

5.7 Nozzle

From test rig direct measurements at the nozzle exit, the gauge pressure p_{g5} and the total temperature T_{05} are obtained. The stagnation pressure at nozzle exit is calculated from:

$$p_{05} = p_{amb} + p_{g5}; \qquad kPa \tag{5.39}$$

The pressure loss coefficient is:

$$k_{45} = \frac{\frac{p_{04} - p_{05}}{p_{04}}}{\left(\frac{W_4\sqrt{T_{04}}}{p_{04}}\right)^2} \tag{5.40}$$

The isentropic efficiency η_N is obtained by:

$$\eta_N = \frac{h_{04} - h_5}{h_{04} - h_{5s}} \tag{5.41}$$

- Case A: Subsonic flow (or un-chocked flow)

  Subsonic flow occurs when the expansion to p_{amb} is completed in the nozzle, such that:

$$\frac{p_{04}}{p_{amb}} \leq \frac{p_{04}}{p_c}$$

  Where p_{04}/p_c is the critical pressure ratio and $p_5 = p_{amb}$.

The static enthalpy h_5 is found following the next relations:

$$\phi_5 = \phi_{05} - R_g * ln\left(\frac{p_{05}}{p_{amb}}\right); \qquad \text{kJ/kg} \tag{5.42}$$

$$T_5 = f_T(\phi_5); \qquad \text{K} \tag{5.43}$$

$$h_5 = f_h(T_5); \qquad \text{K} \tag{5.44}$$

where $\phi_{05} = f_\phi(T_{05})$

Then, the nozzle exit velocity C_5 is:

$$C_5 = \sqrt{2(h_{04} - h_5)} \tag{5.45}$$

By conservation of mass:

$$\dot{m}_5 = \dot{m}_4 \tag{5.46}$$

The effective nozzle area is:

$$A_5 = \frac{\dot{m}_5}{\rho_5 \, C_5} \tag{5.47}$$

Where ρ_5 is the static density at nozzle exit.

- Case B: chocked flow If the expansion to p_a is completed in the nozzle such that,

$$\frac{p_{04}}{p_a} > \frac{p_{04}}{p_c}$$

then chocked flow takes place.

In this case $M_5 = 1$. The critical temperature and the critical pressure are:

$$T_c = \frac{2 \, T_{04}}{\gamma + 1}; \qquad \text{K} \tag{5.48}$$

$$p_c = p_{04}\left[1 - \frac{1}{\eta_N}\left(1 - \frac{T_c}{T_{04}}\right)\right]^{\frac{\gamma}{\gamma-1}} \tag{5.49}$$

The static enthalpy h_{5c} is obtained from the following relations:

$$\phi_{cs} = \phi_{04} - R * ln\left(\frac{p_{04}}{p_c}\right); \qquad \text{kJ/kg} \qquad (5.50)$$

$$T_{cs} = f_T(\phi_{cs}); \qquad \text{K} \qquad (5.51)$$

$$h_{cs} = f_h(T_{cs}); \qquad \text{kJ/kg} \qquad (5.52)$$

The density, critical nozzle exit velocity and the effective nozzle area are:

$$\rho_5 = \frac{p_c}{R\ T_c}; \qquad \text{K} \qquad (5.53)$$

$$C_5 = \sqrt{2(h_{04} - h_c)}; \qquad \text{m/s} \qquad (5.54)$$

$$A_5 = \frac{\dot{m}_5}{\rho_c\ C_c}; \qquad m^2 \qquad (5.55)$$

- Case C: supersonic flow occurs in convergent-divergent nozzles [46]. Because the SR-30 engine has a convergent nozzle, this case will not be considered.

5.8 Thrust

The thrust is not measured by the SR-30 test bed, but it may be calculated as well by conservation of linear momentum, through the following equation:

$$F_N = (\dot{m}_5)C_5 - \dot{m}_a C_a + (p_5 - p_{amb})A_5 \qquad (5.56)$$

5.9 Thrust Specific Fuel Consumption

Thrust specific fuel consumption is used to determine the fuel consumption (kg/s) per unit of thrust (kN), as follows:

$$TSFC = \frac{\dot{m}_f}{F_N}; \qquad (kg/hr)/kN \qquad (5.57)$$

5.10 Validation and Discussion of Results

Figure 5–3 shows the variation of fuel flow with time. The variation of fuel flow was performed through a manual control on the power lever angle (PLA) of the SR-30 engine. The fuel flow data was registered and introduced into the engine model.

For this reason the fuel flow signal, obtained from experimental data, coincides with the fuel flow signal used by the engine model.

The fuel flow was varied with the aim of providing steady and transient states.

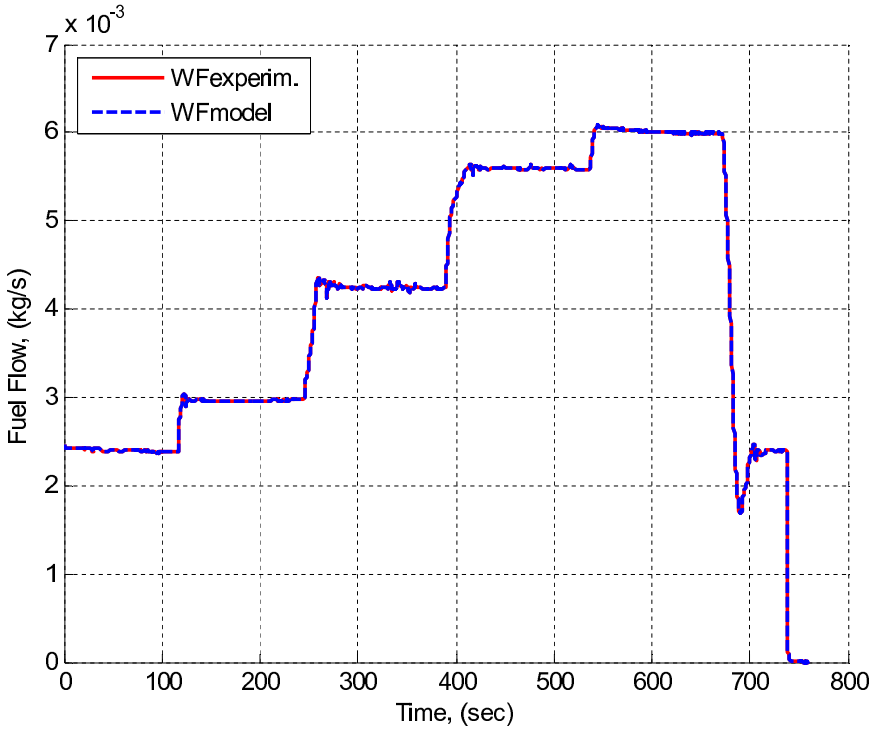

Figure 5–3: Fuel flow vs time.

Pressure loss coefficients were calculated for the intake, combustor and nozzle, from experimental data. This coefficients were obtained at a fixed rotational speed. This is the design speed (77500 was considered for the design speed) at which the engine works for the longest time during its normal operation. The calculated values were maintained constant for all the operating conditions. Thus:

1. Intake: the pressure loss coefficient for the intake was obtained: $ka1 = 0$. $ka1$ is obtained, using experimental data, from equation 5.2. This value is obtained when $p_{0a} = p_{01}$ (discussed in chapter 4). This is the case only for the SR-30 engine due to its fixed location.

2. Combustor: the pressure loss factor (PLF) for the combustor, is: $PLF = 0.9916$. It is obtained from equation 5.23
3. Nozzle: the pressure loss coefficient $k45$ is 4.9. Its calculated value is obtained from equation 5.40.

Correction factors (CFs) were used to make an initial adjustment to closely match the simulated output (such as rotational speed, temperature, pressure, etc.), with outputs obtained from experimental data. These plots will be presented in the following figures. The correction factors used and their corresponding values are detailed below.

1. Compressor map: correction factors used in the compressor map, were obtained in steady state performance at 77500 rpm (which is considered as the design speed [9]), from the comparison of air mass flow, pressure ratio and isentropic efficiency from the simulated results at the compressor with the corresponding experimental data recorded.
   - Referred flow: $CF1 = 0.8421$, used in equation 4.11.
   - Isentropic efficiency: $CF2 = 1.2442$, used in equation 4.12
   - Pressure ratio: $CF3 = 1.4731$, used in equation 4.13.
2. Combustor: correction factors ($CF4_{RPM}$) were used in the equation 4.24 to improve the results of the combustion efficiency correlation 4.22. They were obtained by the comparison between simulated and experimental results at various speeds, as it is specified below:
   - For 45000 rpm: $CF4_{45000} = 1.2643$
   - For 50000 rpm: $CF4_{50000} = 1.0784$
   - For 60000 rpm: $CF4_{60000} = 0.8679$
   - For 70000 rpm: $CF4_{70000} = 0.8363$
   - For 77500 rpm: $CF4_{77500} = 0.9152$

   The result plots for the combustion efficiency corrected are shown in Figure 5–4.

3. Mechanical efficiency: correction factors $CF5_{RPM}$ used in equation 4.33, were obtained in the same way as it was obtained for the combustion efficiency, as follows:
   - For 45000 rpm: $CF5_{45000} = 0.9015$
   - For 50000 rpm: $CF5_{50000} = 0.8989$
   - For 60000 rpm: $CF5_{60000} = 0.8042$
   - For 70000 rpm: $CF5_{70000} = 0.7487$
   - For 77500 rpm: $CF5_{77500} = 0.7499$

   The resulting plots for mechanical efficiency corrected are shown in Figure 5–5.
4. Turbine map: correction factors CFs were obtained from comparing the values of gas flow at the turbine inlet and turbine isentropic efficiency, between simulated results and experimental data, at 77500 rpm (assumed design speed [9]), thus:
   - Referred flow: $CF6 = 0.9728$, used in equation 4.40
   - Isentropic efficiency: $CF7 = 1.2811$, used in equation 4.41
5. Effective area at nozzle exit: discharge coefficients CD_{RPM} used in equation 4.71, were were applied for various rotational speeds, to model better the equation used to obtain the effective area at the nozzle exit.
   - For 45000 rpm: $CD_{45000} = 0.9015$
   - For 50000 rpm: $CD_{50000} = 0.8989$
   - For 60000 rpm: $CD_{60000} = 0.8042$
   - For 70000 rpm: $CD_{70000} = 0.7487$
   - For 77500 rpm: $CD_{77500} = 0.7499$

   The steady states were obtained at various average rotational speeds, as shown in the Figure 5–6. This rotational speeds were: 45000 rpm, 50000 rpm, 60000 rpm, 70000 rpm and 77500 rpm. The engine shuts down after returning to 45000 rpm, but, the computer continued registering the data until it was observed that the fuel flow data reached to zero.

Figure 5–7 shows the temperature plots. For comparison, only the temperatures T_{02}, T_{03} and T_{04} were used. The figure shows as the rotational speed increases, temperatures increase, and that the simulated temperatures are very close to the measured data. It is shown that transients need to be improved. Fig. 5–8 shows the pressure plots. For comparison, only the pressures p_{02}, p_{03} and p_{04} were used. Errors corresponding to the simulated rotational speeds, temperatures and pressures will be shown in the following chapter.

There is a great error in the last part of each plots, because after the engine was shutdown at 45000 rpm, the computer continued the registering of data. The model is not intended to simulate so well that behavior.

From the plots presented for the combustion and mechanical efficiencies, it is shown that the model results are not very accurate compared with the corresponding experimental results, especially in the transient states. This suggests the need to find correlations which improve the results. Also the need to introduce in the transient model, phenomenons such as heat soakage in the combustor are suggested. The next chapter presents an approach to attend these issues.

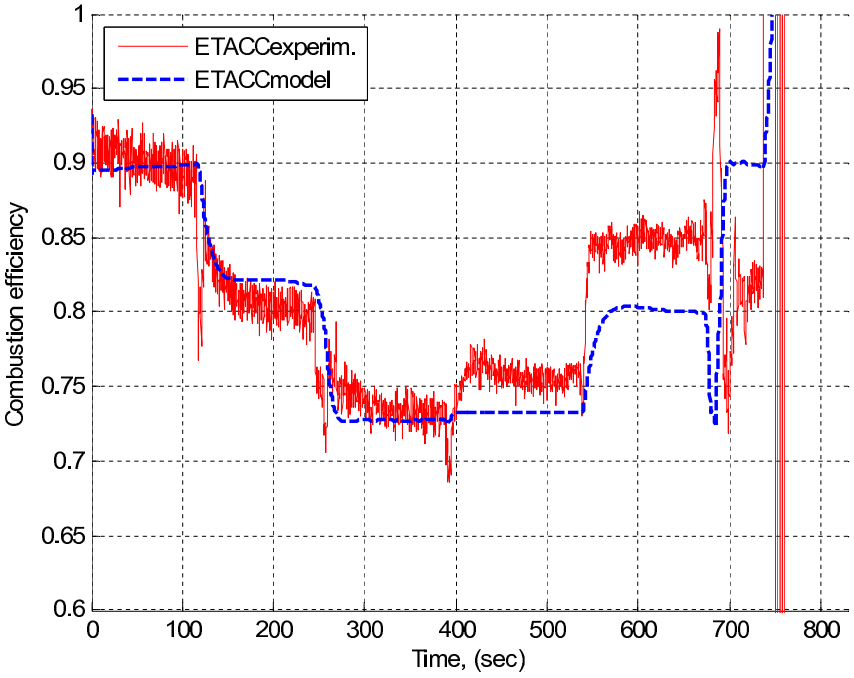

Figure 5–4: Combustion efficiency vs time.

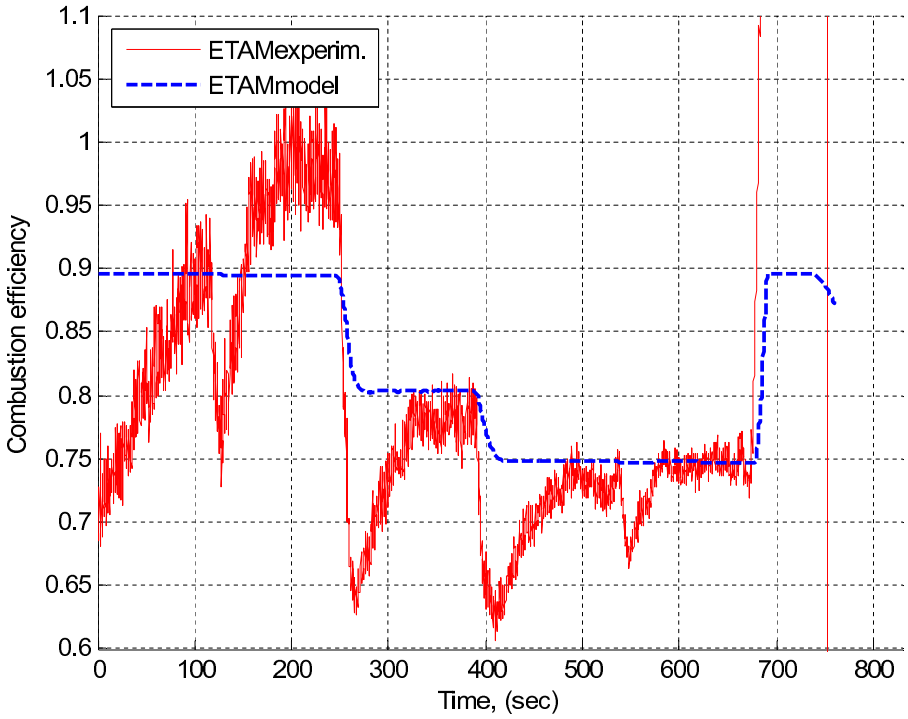

Figure 5–5: Mechanical efficiency vs time.

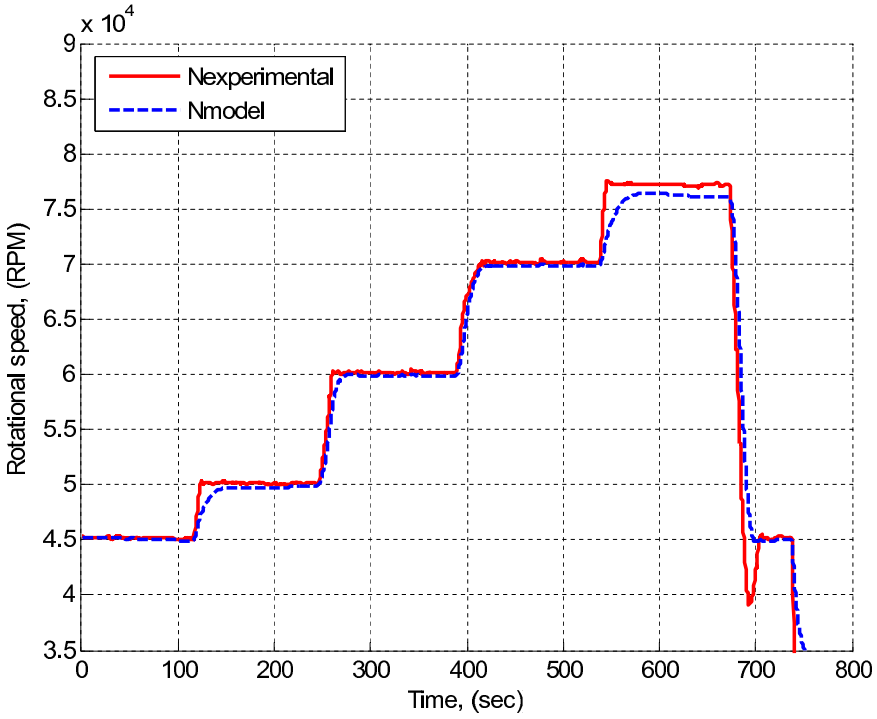

Figure 5–6: Rotational speed vs time.

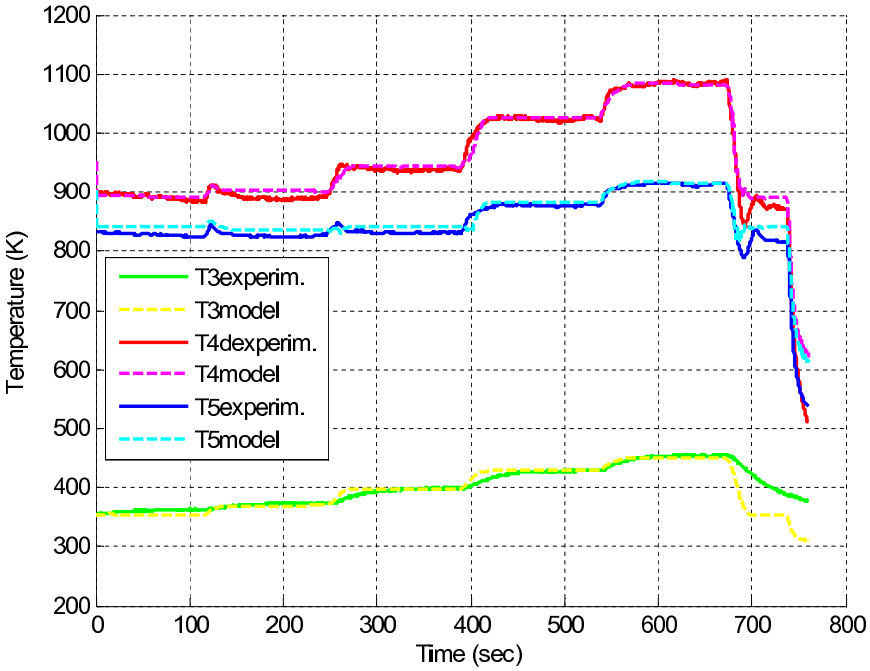

Figure 5–7: Temperature vs time.

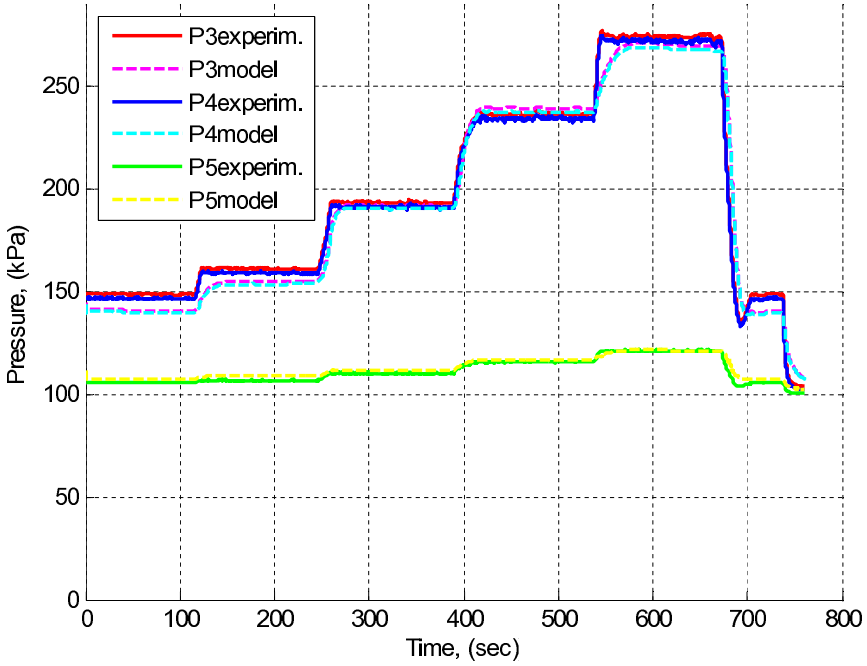

Figure 5–8: Pressure vs time.

CHAPTER 6
ESTIMATION OF PERFORMANCE PARAMETERS

In order to maintain accurate on-line estimation of aircraft engine performance parameters, it is necessary to develop a design approach to meet this. A critical aspect in designing a hybrid model is to make it robust to off-nominal engine behavior caused by both degradation and anomalies. Component degradation is a natural phenomenon which occurs to all aircraft engines as a result of normal usage. The level of component degradation worsens gradually with time, and consequently the engine performance deviates gradually from its nominal level. Component faults similarly result in off-nominal engine performance, but they occur abruptly due to anomalous events such as foreign or domestic object damage.

In this chapter the dual unscented Kalman filter (DUKF) is implemented for the SR-30 turbojet engine which consists of simultaneously estimating the state variables and the health parameters. A detailed explanation to the approach used in the current work follows.

6.1 UKF dual estimation

Figure. 6–1 shows the architecture of dual Kalman filtering, which was introduced by Wan and Van der Merwe [42] and explained with more details in Van der Merwe's Thesis [58], proposed for the identification of physical nonlinear model. A schematic diagram, for the Dual Unscented Kalman Filter (UKF), is presented in Figure 6–1. As shown in the figure, the DUKF consists of two Kalman filters which are the state variable and the health parameter estimation Kalman filters.

The actual engine and DUKF receive the same command input (u_k). The measured outputs (y_k) from the actual engine is used by the two filters of DUKF. The health parameter estimation uses the measured output from experimental data, the previous estimates of health parameter ($\hat{h}_{k-1}$), and the previous state variable estimation ($\hat{x}_{k-1}$) to obtain the new health parameters ($\hat{h}_k$). Health parameters, such as flow capacity and efficiency will act as "tuners" to minimize the residuals (which are into the filters, it will be explained into the next sections) and so to obtain more accurate model predictions. The state variable estimation will receive, in addition to the control input and measured outputs, the previous state estimation ($\hat{x}_{k-1}$) and the actual health parameter estimation ($\hat{h}_k$) to correct the state variable ($\hat{x}_k$).

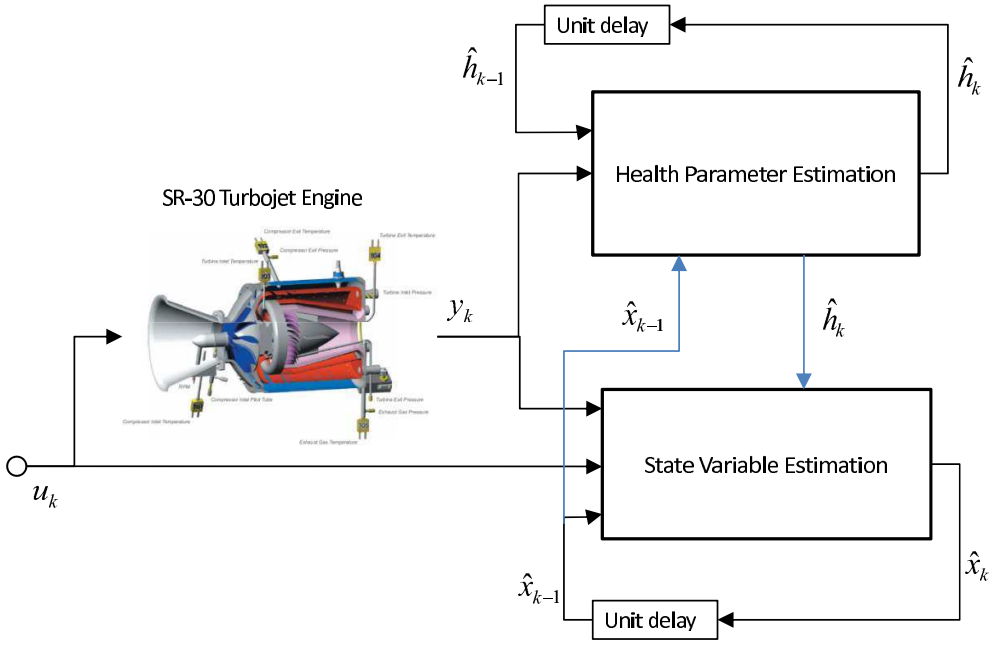

Figure 6–1: Schematic diagram of UKF dual estimation.

The DUKF will be presented and follows the algorithm presented by Wan and van der Merwe [42].

The discrete-time engine nonlinear dynamical model is expressed as follows:

$$x_{k+1} = f(x_k, u_k, h_k) + \omega_k \tag{6.1}$$

$$y_k = g_y(x_k, u_k, h_k) + \nu_k \tag{6.2}$$

Where, x_k: vector of state variables, u_k: control command inputs, h_k: health parameters, y_k: measurable outputs vector, ν_k: process noise vector and ω_k: measurement noise vector.

6.1.1 State Variable Estimation

The block diagram of the state variable estimation procedure is shown in Fig. 6–2. According to the diagram the previous state estimates $\hat{x}_{k-1}$ is used in conjunction with the state transition equation defined by relation 6.1 to predict a prior estimate of the state variables $\hat{x}_k^-$. The prior estimate is used by the measurement update equation 6.2 which gives as a result the a priori measurable output parameter $\hat{y}_{k1}^-$. The difference between the experimental data and the estimated outputs are the residuals which are multiplied by the Kalman gain K_{x_k} and then added to the a priori estimate $\hat{x}_k^-$ to update the state variables. Each iteration requires $2L_x + 1$ calculations of relations 6.1 and 6.2, where L_x is the number of state variables. Therefore, the number of sigma point for the state estimation will be three because the number of states used is one (the rotational speed).

The calculation procedure to build the algorithm was developed by Wan and Van der Merwe [42, 58], as follows:

1. Given the relations which represent the discrete nonlinear engine model, the unscented Kalman filter (UKF) is initialized as follows:

$$\hat{x}_0 = E(x_0) \tag{6.3}$$

$$P_{x0} = E[(x_0 - \hat{x}_0)(x_0 - \hat{x}_0)^T] \tag{6.4}$$

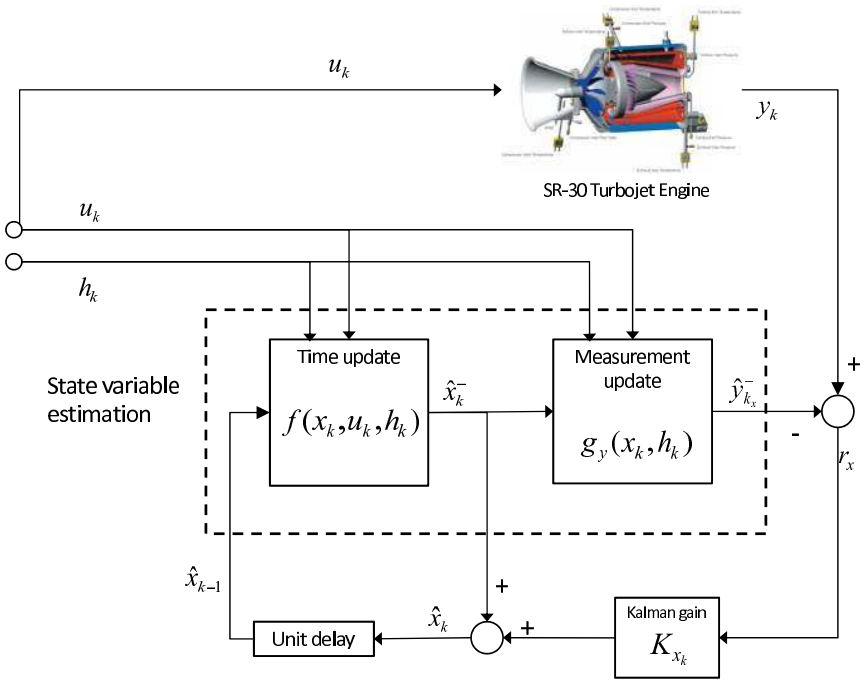

Figure 6–2: State variable estimation.

where, x_0 is the actual value of the random state variable, $\hat{x}_0$ is the estimated values of the random state variable, $E(x_0)$ is the expected value of the random variable x_0, and P_{x0} is the covariance between the actual state and the estimated state.

2. The following time update equations are used to propagate the state estimate and covariance from one measurement time to the next.

   (a) To propagate from time step (k-1) to k, first choose sigma points $\hat{x}_{k-1}^i$, since the current best guess for the mean and covariance of x_k are $\hat{x}_{k-1}$ and P_{k-1}:

$$\hat{x}_{k-1}^i = \hat{x}_{k-1} \qquad i = 0 \tag{6.5}$$

$$\hat{x}_{k-1}^i = \hat{x}_{k-1} + \left(\sqrt{(L_x+\lambda)P_{k-1}}\right)_i \qquad i = 1, ..., L_x \tag{6.6}$$

$$\hat{x}_{k-1}^i = \hat{x}_{k-1} - \left(\sqrt{(L_x+\lambda)P_{k-1}}\right)_{i-L_x} \qquad i = L_x+1, ..., 2L_x \tag{6.7}$$

   where: $\hat{x}_{k-1}^i$ obtained from equations 6.5 to 6.7 from a state vector of $[1 \times 3]$, L_x is the number of states and λ is the composite scaling parameter which is

calculated from:

$$\lambda = \alpha^2 * (L_x + k_x) - L_x \tag{6.8}$$

where: α determines the spread of sigma points around x and is usually set to a small positive value ($10^{-4} \leq \alpha < 1$), k_x is a secondary scaling parameter which usually set to "0". In this work, the following values were used: $\alpha = 0.99$ and $k_x = 0$.

(b) The known nonlinear system of equation 6.1 is used to transform the sigma points into x_k^i vectors:

$$\hat{x}_k^i = f\left(\hat{x}_{k-1}^i, u_k, \hat{h}_k\right) \tag{6.9}$$

where: u_k is the control input and $\hat{h}_k$ is the actualized health parameter estimation.

(c) The $\hat{x}_k^i$ vectors are combined to obtain a priori state estimate at time k:

$$\hat{x}_k^- = \sum_{i=0}^{2L} W_i^{(m)} \hat{x}_k^i \tag{6.10}$$

(d) The a priori error covariance is calculated by adding Q_{x_k} to the end of the equation to take the process noise into account:

$$P_{x_k}^- = \sum_{i=0}^{2L} W_i^{(c)} \left(\hat{x}_k^i - \hat{x}_k^-\right)\left(\hat{x}_k^i - \hat{x}_k^-\right)^T + Q_{x_k} \tag{6.11}$$

The weights, $W_i^{(m)}$ introduced in equation 6.10, and $W_i^{(c)}$ from equation 6.11 , are calculated using:

$$W_0^{(m)} = \frac{\lambda}{\lambda + L_x} \tag{6.12}$$

$$W_0^{(c)} = \frac{\lambda}{\lambda + L_x} + 1 - \alpha^2 + \beta \tag{6.13}$$

$$W_i^{(c)} = W_i^{(m)} = \frac{1}{2(L_x + \lambda)}, \qquad i = 1, ..., 2L_x \tag{6.14}$$

Where: λ is the composite scaling parameter and it was obtained by equation 6.8. For Gaussian distribution, $\beta = 2$ is optimal [58].

3. Once the time update equations are complete, the measurement-update equations are evaluated. Here a complete new set of sigma points may be used, these sigma points discard any odd-moments information captured by the original propagated sigma points calculated by equations 6.5 to 6.7. The sigma points may be represented in the vectorial form as follow:

   (a) Choose sigma points $\hat{x}_k^i$ taking into account that the current best guess for the mean and covariance of x_k are $\hat{k}_x^-$ and P_k^-:

$$\hat{x}_k^i = \left[\hat{x}_k^- \qquad \hat{x}_k^- \pm \sqrt{(L_x + \lambda)P_{x_k}^-}\right] \tag{6.15}$$

   (b) Use the nonlinear measurement equation 6.2 to transform the sigma points into $\hat{y}_k^{(i)}$ vectors (predicted measurements):

$$\hat{y}_k^{(i)} = g_y\left(\hat{x}_k^{(i)}, \hat{h}_k\right) \tag{6.16}$$

   (c) Combine the $\hat{y}_k^{(i)}$ vectors to obtain the predicted measurement at time k:

$$\hat{y}_k^- = \sum_{i=0}^{2L} W_i^{(m)} \hat{y}_k^{(i)} \tag{6.17}$$

   (d) Estimate the covariance of the predicted measurement:

$$P_y = \sum_{i=0}^{2L} W_i^{(c)} \left(\hat{y}_k^{(i)} - \hat{y}_k^-\right)\left(\hat{y}_k^{(i)} - \hat{y}_k^-\right)^T + R_{x_k} \tag{6.18}$$

$$\tag{6.19}$$

   (e) The residual is:

$$r_k = \left(y_k - \hat{y}_k^-\right) \tag{6.20}$$

(f) Estimate the cross covariance between $\hat{x}_k^-$ and $\hat{y}_k^-$:

$$P_{xy} = \sum_{i=0}^{2L} W_i^{(c)} \left(\hat{x}_k^{(i)} - \hat{x}_k^-\right) \left(\hat{y}_k^{(i)} - \hat{y}_k^-\right)^T \tag{6.21}$$

(g) The Kalman gain matrix is approximated from the cross-correlation and measurement covariances using:

$$K_{x_k} = P_{xy} \left(P_y\right)^{-1} \tag{6.22}$$

(h) The measurement update equations used to determine the mean, $\hat{x}^k$, and covariance, P_k, of the filtered state are:

$$\hat{x}_k = \hat{x}_k^- + K_{x_k} \left(y_k - \hat{y}_k^-\right) \tag{6.23}$$

$$P_{x_k} = P_{x_k}^- - K_{x_k} P_y K_{x_k}^T \tag{6.24}$$

The algorithm above assumes that the process and measurement equations are linear with respect to the noise, as shown in equations 6.1 and 6.2.

6.1.2 Health Variable Estimation

The flow diagram which represents the health estimation procedure is shown in Fig. 6–3. According to the diagram, the time update does not require the calculation of sigma points, then, the a priori health parameter $\hat{h}_k^-$ is equal to the previous health parameter estimated $\hat{h}_{k-1}$. The measurement update needs to calculate the sigma points and it require the previous state estimated $\hat{x}_{k-1}$.The residual r_h is generated in the same way as in the state estimation case, it is the difference between the experimental data and the output measurements $\hat{y}_{k_h}$. The residual multiplied by the Kalman gain K_{h_k} and then added to the a priori health parameters, serve to recalculate the new health parameter $\hat{h}_k$.

The same authors [42, 58], who presented the state estimation, took into account the health parameter estimation. The parameter estimation equations for the UKF

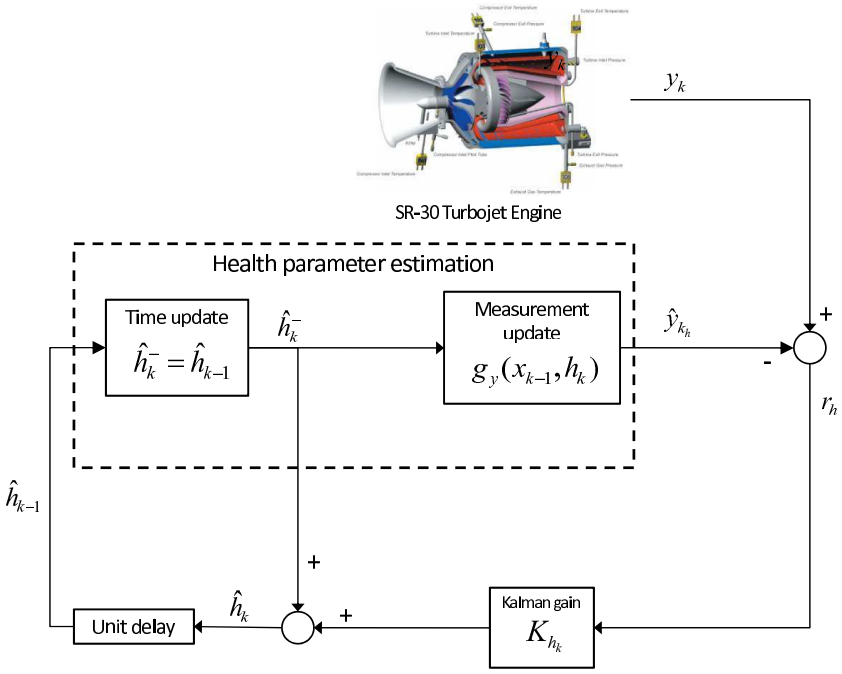

Figure 6–3: Health parameters estimation.

differers from the state estimation, in the time update equations used to find the a priori mean and covariance of the state. The system equations for the health parameter filter are:

1. The filter is initialized with the predicted mean and covariance of the parameters:

$$\hat{h}_0 = E(h_0) \tag{6.25}$$

$$P_{h0} = E[(h_0 - \hat{h}_0)(h_0 - \hat{h}_0)^T] \tag{6.26}$$

where: h_0 is the actual health parameter which is a scalar and varies with time, $E(h_0)$ is the mean of the health parameters, $\hat{h}_0$ is the estimated health parameter and P_{h0} is the initial covariance.

2. The time update and the parameter covariance is performed using

$$\hat{h}_k^- = \hat{h}_{k-1} \tag{6.27}$$

$$P_{h_k}^- = P_{h_{k-1}} + Q_{h_{k-1}} \tag{6.28}$$

Where: $Q_{h_{k-1}}$ is the covariance of the process noise.

Roughly speaking, The larger the covariance $P_{h_k}^-$, the more quickly older data is discarded. There are several options on how to choose $Q_{h_{k-1}}$. In this work a method analogous to recursive least squares is used:

$$Q_{h_k} = \left(\lambda_{RLS}^{-1} - 1\right) P_{h_{k-1}} \tag{6.29}$$

where $\lambda_{RLS} \in (0, 1]$ is often referred to as the forgetting factor [58]. This scheme adjusts $P_{h_k}^-$ such that it is slightly larger than $P_{h_{k-1}}$, which has the effect of discarding older data more quickly. Smaller values of λ increase this effect. In this work, a value of (0.9995) was used, because it was observed that it produces the most stable filter results. Note that λ_{RLS} should not be confused with λ used for sigma point calculation.

3. Implement the measurement update equations.
   (a) The sigma points are calculated from the a priori mean and covariance of the parameters using:

$$\hat{h}_k^i = \left[\hat{h}_k^- \qquad \hat{h}_k^- \pm \sqrt{(L+\lambda)P_{h_k}^-}\right] \tag{6.30}$$

   (b) The expected measurement matrix, $\hat{y}_{h_k}^i$, is determined using the nonlinear measurement model as follows:

$$\hat{y}_{h_k}^i = g_y\left(\hat{h}_k^i, \hat{x}_{k-1}\right) \tag{6.31}$$

   (c) The mean measurement is:

$$\hat{y}_{h_k}^- = \sum_{i=0}^{2L} W_i^{(m)} \hat{y}_{h_k}^{(i)} \tag{6.32}$$

(d) the measurement covariance:

$$P_y = \sum_{i=0}^{2L} W_i^{(c)} \left(\hat{y}_{h_k}^{(i)} - \hat{y}_{h_k}^{-}\right) \left(\hat{y}_{h_k}^{(i)} - \hat{y}_{h_k}^{-}\right)^T + R_{h_k} \tag{6.33}$$

where: R_{h_k} is the covariance of the measurement noise and it is additive to the measurement covariance.

(e) The residual is:

$$r_{h_k} = \left(y_k - \hat{y}_{h_k}^{-}\right) \tag{6.34}$$

(f) The cross-correlation covariance, P_{xy} , is calculated using:

$$P_{xy} = \sum_{i=0}^{2L} W_i^{(c)} \left(\hat{h}_k^{(i)} - \hat{h}_k^{-}\right) \left(\hat{y}_{h_k}^{(i)} - \hat{y}_{h_k}^{-}\right)^T \tag{6.35}$$

(g) The Kalman gain matrix is approximated from the cross-correlation and measurement covariances using:

$$K_{h_k} = P_{xy} \left(P_y\right)^{-1} \tag{6.36}$$

(h) The measurement update equations are:

$$\hat{h}_k = \hat{h}_k^{-} + K_{h_k} \left(y_k - \hat{y}_{h_k}^{-}\right) \tag{6.37}$$

$$P_{h_k} = P_{h_k}^{-} - K_{h_k} P_y K_{h_k}^T \tag{6.38}$$

6.1.3 DUKF for SR-30 Turbojet Engine

Experimental data are available for this engine. The nonlinear simulation block diagram developed has computational modules for intake, compressor, combustor, turbine, nozzle and rotor.

Engine state vector, x, is defined as follows:

$$x = (N)' \tag{6.39}$$

Where N is the rotor speed.

Since inter-component volumes are not very large in this jet engine, its dynamics do not contribute significantly to dynamic behavior of jet engine in the frequency range under $10Hz$ (Seldner 1972 [59]). Hence, volume dynamics can be neglected.

In this work, engine component deviation parameter vector Δh will act as a tuner to minimize the residual between the measured outputs and estimated outputs.

Two sets of tuners were considered, the first one is:

$$\Delta h_1 = (\Delta G_c, \Delta \eta_c, \Delta G_t, \Delta \eta_t, \Delta A_n)' \tag{6.40}$$

and the second one is:

$$\Delta h_2 = (\Delta G_c, \Delta \eta_c, \Delta G_t, \Delta \eta_t, \Delta A_n, \Delta PR_c, \Delta \eta_b, \Delta \eta_m)' \tag{6.41}$$

Where ΔG_c is the flow deviation parameter of the compressor, $\Delta \eta_c$ is the efficiency deviation parameter of the compressor, ΔG_t is the flow deviation parameter of the turbine, $\Delta \eta_t$ is the efficiency deviation parameter of the turbine, and ΔA_n is the area deviation parameter of the nozzle, ΔPR_c is the pressure ratio deviation parameter of the compressor, $\Delta \eta_b$ is the combustion efficiency deviation parameter and $\Delta \eta_m$ is the mechanical efficiency deviation parameter.

If an engine component performance is changed gradually or suddenly, due to engine degradation or anomalies, it will cause difference between measurement and estimation values; DUKF will be able to minimize this difference by modifying Δh.

The control vector , u, is defined as follows:

$$u = (W_f)' \tag{6.42}$$

Where W_f is the fuel flow rate

The measurable vector, y_m is determined by the engine test rig, as follows:

$$y_m = (N, P_1, T_1, P_2, T_2, P_3, T_3, P_4, T_4, P_5, T_5)' \tag{6.43}$$

The unmeasurable vector, y_u, is selected as follows:

$$y_u = (F, W_a, S_{fc})' \tag{6.44}$$

Where F is the net thrust, W_a is the air flow rate, and S_{fc} is the thrust specific fuel consumption.

6.2 Discussion of Results

With the application of DUKF, the model matches more closely with the experimental data as shown in the figures below. DUKF was implemented for two sets of deviation parameters. The first, is composed of five deviation parameters, as it is shown by relation 6.40, and the second is composed of eight deviation parameters, as expressed by relation 6.41.

Figure 6–4 shows the fuel flow introduced as the command input, which is the same for the test rig, model and estimation procedure. Figure 6–5 shows the rotational speeds plots, from: experimental data, model and DUKF estimation. As shown in the plot 6–6, the best fit is achieved with the use of DUKF. The same precision was achieved with the two sets of deviation parameters. With the model without DUKF, the results show approximately 6% of error in transient state, and 1.5% of error in steady state. With the use of DUKF, for both cases, the results show a maximum error of 4% in transient state and 0.8% for steady state.

To verify the estimation of measurements, the plot of the temperature T_{03} is presented, as shown in Figure 6–7. Other temperatures exhibit similar behavior. Its corresponding error percentage is shown in Figure 6–8. From the plots, it is observed that the dual filter did not improves results compared with the model results, practically, is the same. In transient state, there is a maximum error of 6% for each cases. In steady state, the maximum error was approximately 1.9%.

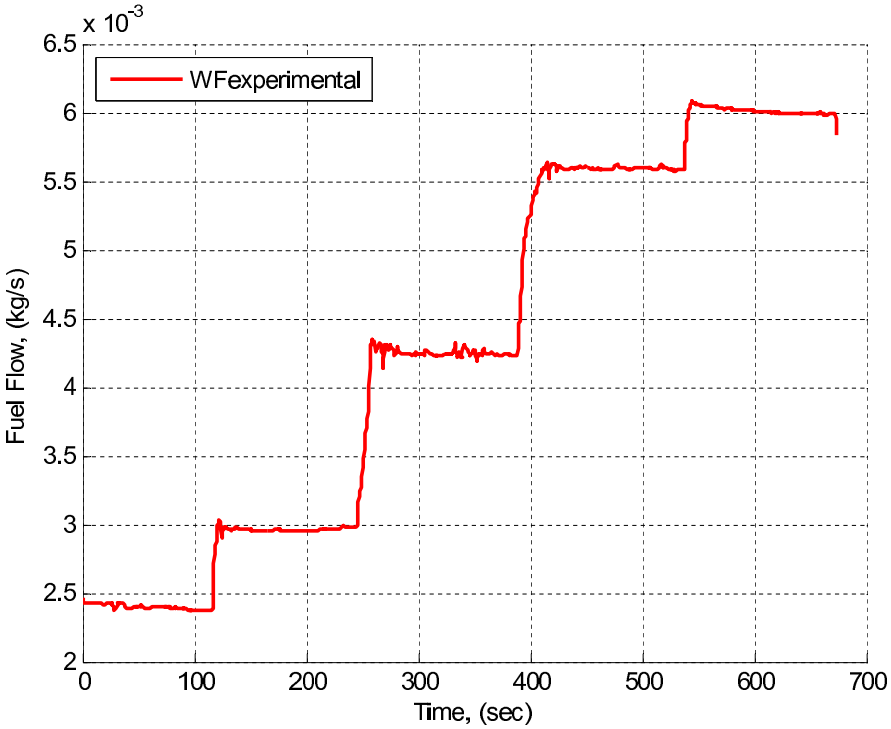

Figure 6–4: Fuel flow vs time.

In the case of pressure, p_{02}, is used to make the comparison, there is a slight improvement in results, as shown in Figures 6–9 and 6–10. Other pressures exhibit similar behavior. With the model, a maximum error in transient state of 9.5% and in steady state of 5.5% was achieved. With DUKF, with the two sets of deviation parameters, maximum errors obtained, in transient state was 9% and in steady state was 5.3%. But it was observed that, in some operating ranges there are better results with DUKF, in others, DUKF performance is slightly poor.

The objective of applying parameter estimation filter, in this work, was to obtain deviation of parameters for the tuning procedure. The DUKF performance was tested for two cases. In one case, five parameter deviations were considered, this is shown in Figure 6–11. The plot shows that the dual filter modifies greatly the values of two parameters for the fitting procedure, these are: the turbine isentropic efficiency deviation ($detat$), which ranged up to a value of approximately 2.7×10^{-4} and the turbine flow capacity deviation (dGt), which tends toward negative values

until the value of -3×10^{-4}. In the other case, it was added three other parameter deviations, with this configuration, the dual filter vary the turbine efficiency deviation until 3×10^{-3} was reached.

According to the results , the dual filter is able to predict with greater accuracy the state variable (rotational speed). But in the case of predicting the experimental measurements, its performance was not as good as for the state variable. This is mainly due to two reasons, which are:

- It was found that initial conditions for both filters (filters for the state and parameter estimation), through trial and error procedure. The initial conditions obtained were only approximated values. The exact initial conditions perhaps can be obtained by exact equations.
- It was observed that the experimental results are time-continues data. The Kalman filter based on DUKF is a discrete filter and it should be applied on a discrete environment. In this work, it was not possible to introduce the experimental data in discrete time.

Taking into account these items, the DUKF technique will perform better, and it may be a very good option for using in diagnostics methods.

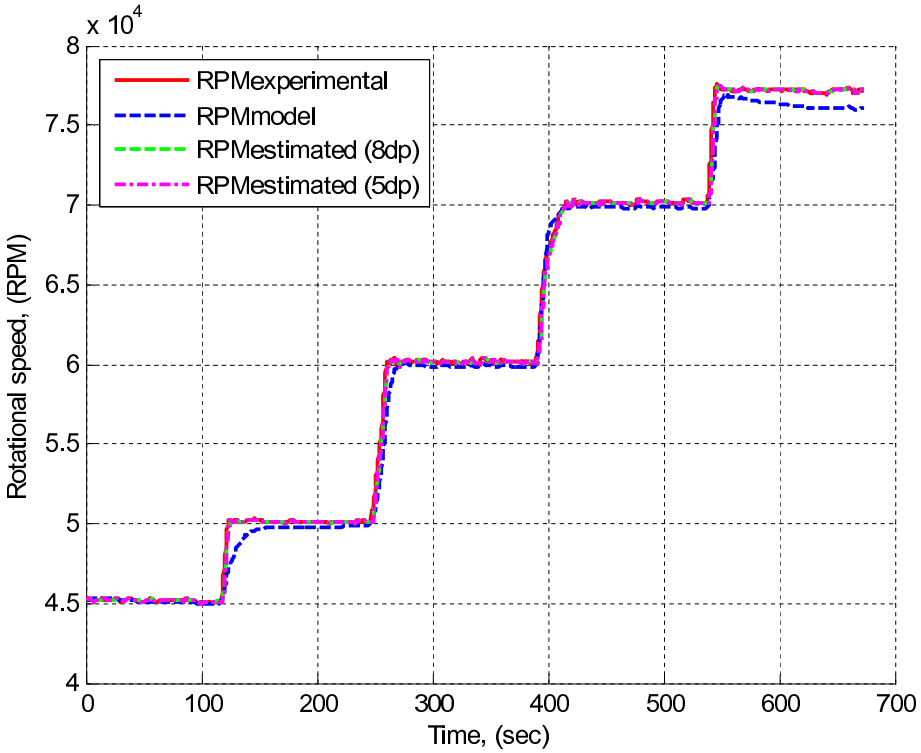

Figure 6–5: Rotational speed vs time.

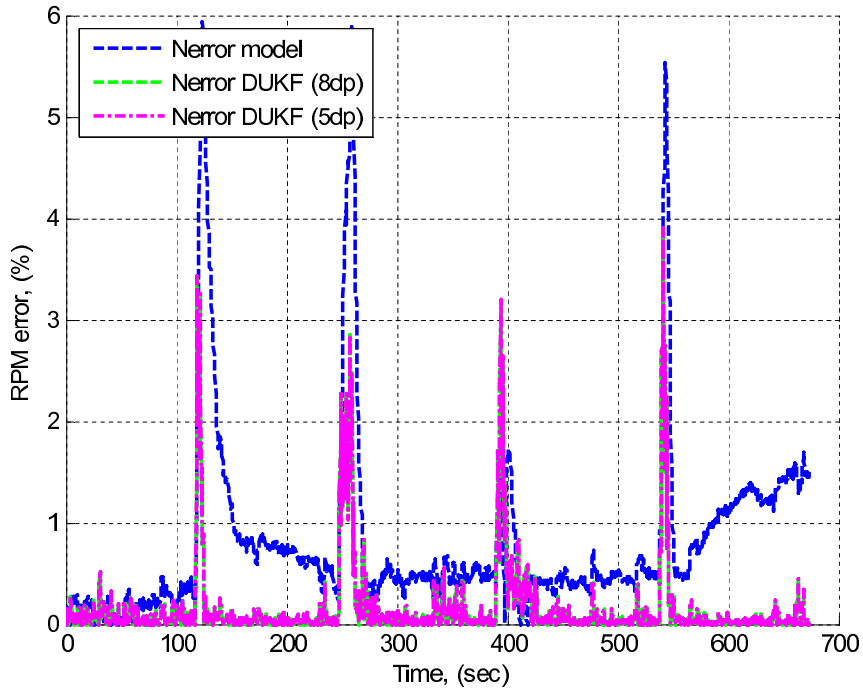

Figure 6–6: Rotational speed error vs time.

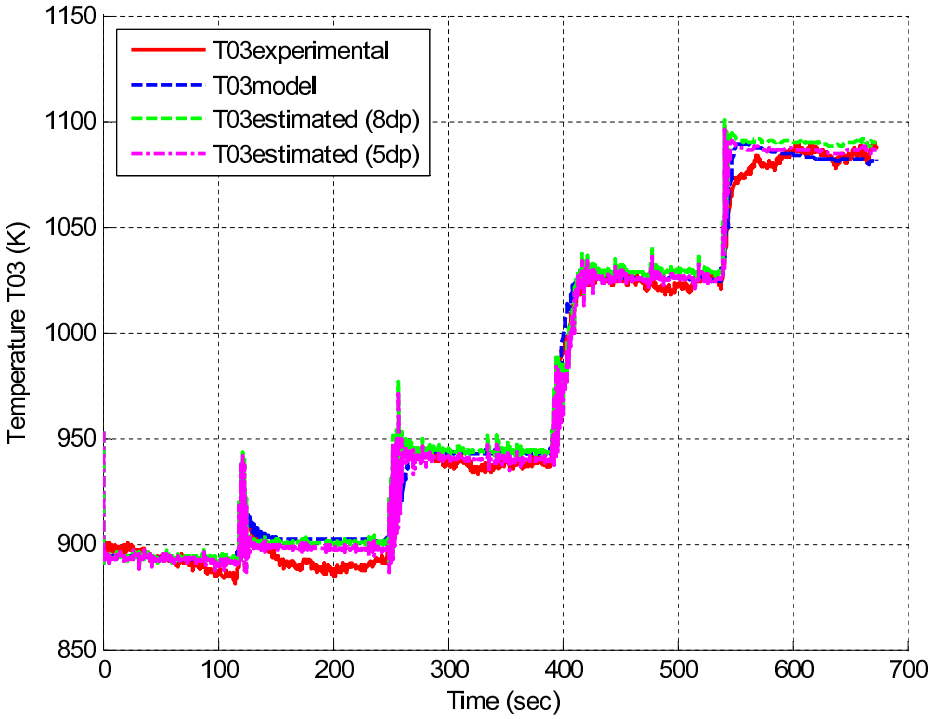

Figure 6–7: Temperature T_{03} vs time.

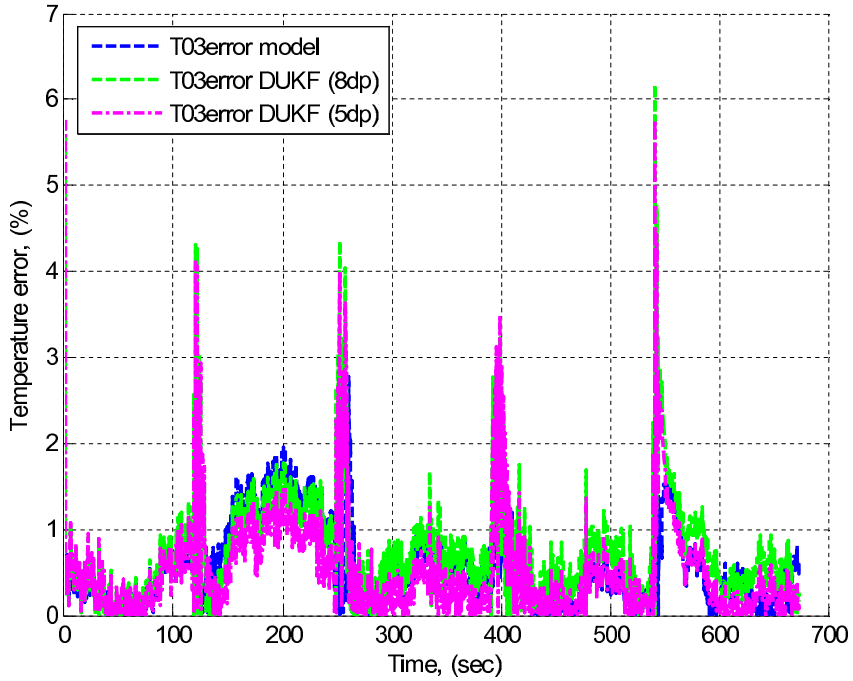

Figure 6–8: Temperature error T_{03} vs time.

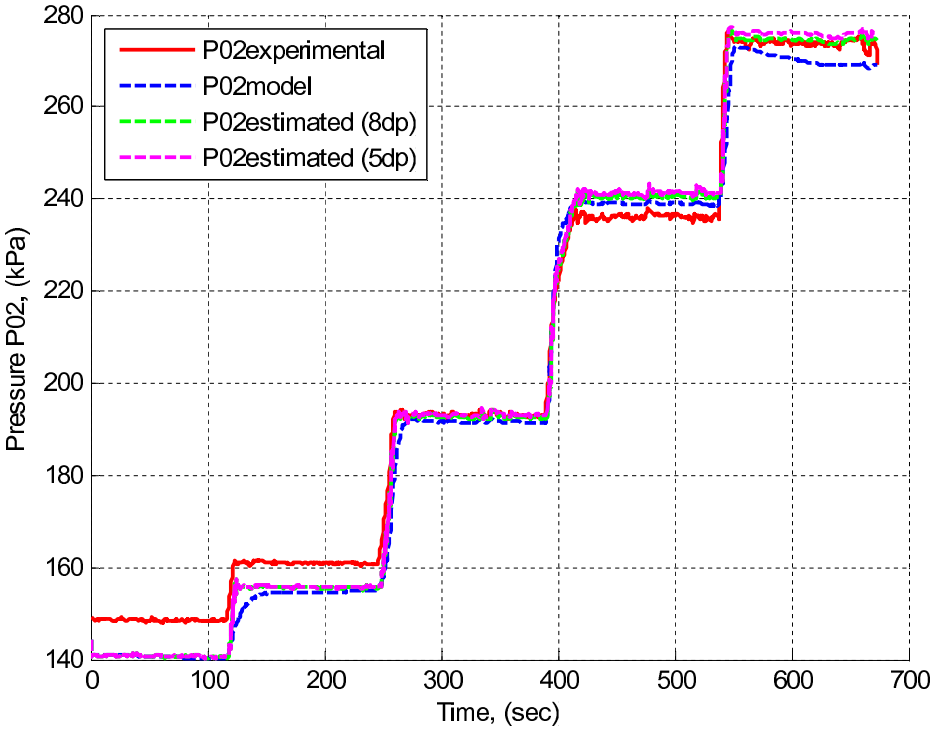

Figure 6–9: Pressure p_{02} vs time.

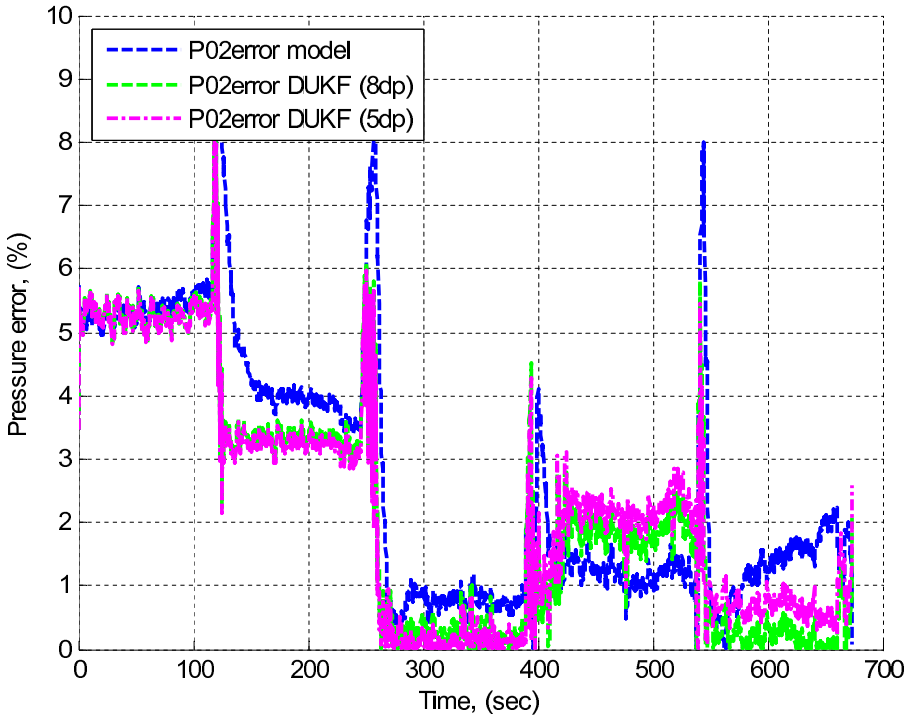

Figure 6–10: Pressure error p_{02} vs time.

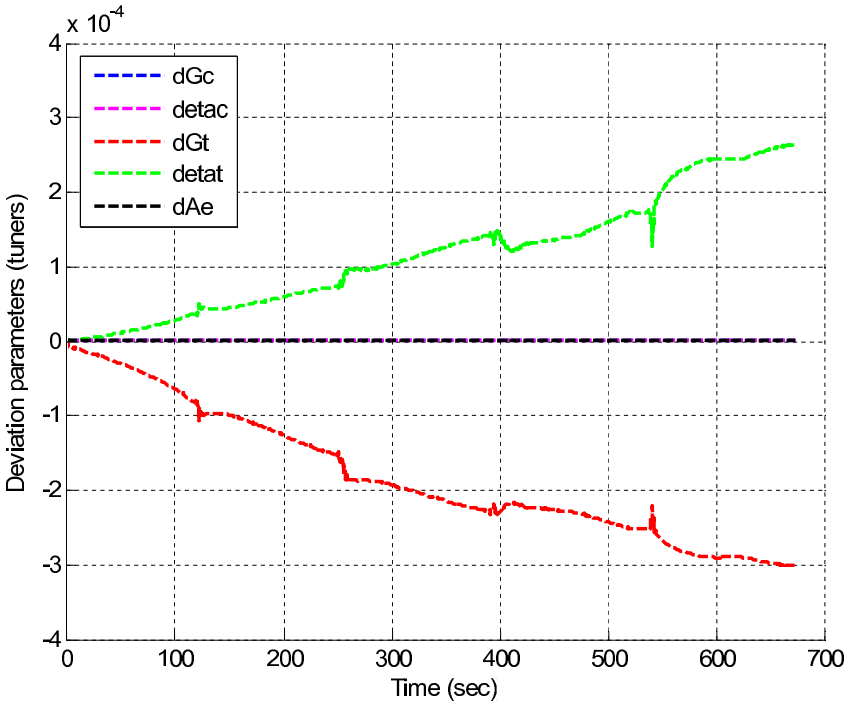

Figure 6–11: Deviation parameters (5dp) vs time.

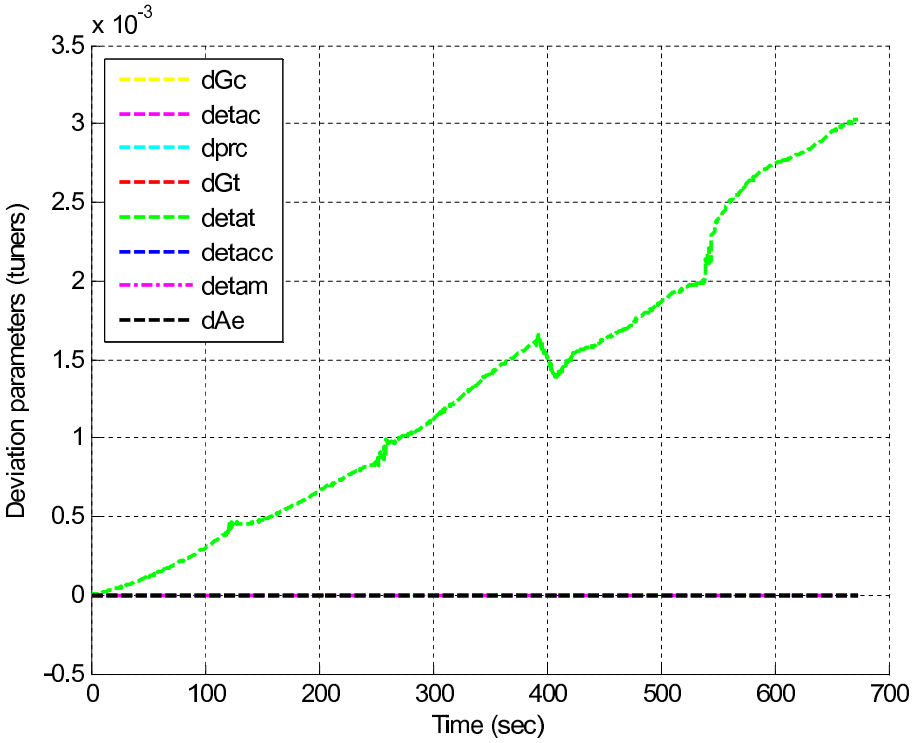

Figure 6–12: Deviation parameters (8dp) vs time.

CHAPTER 7
CONCLUSIONS AND RECOMMENDATIONS

7.1 Conclusions

According to the stated objectives, we can make the following conclusions:

1. According to the stated objectives it may be conducted that the development of an on-line estimation model of the SR-30 gas turbine performance based on dual unscented Kalman filters was successfully achieved. In order to complete the model both compressor and turbine maps were developed and validated experimentally. The model of the SR-30 represents both steady state and transient behavior.
2. The component maps were used to develop the nonlinear model of the engine in Simulink/Matlab. The accuracy of the simulation is strongly dependant on the use of precise engine component performance maps. Correction factors were used to approximate the results to the measured values. It was observed that the mathematical model did not predict very well the mechanical efficiency and combustion efficiency very well. It was necessary to use correction factors at various points of operation. The correction factors were estimated using the experimental data.
3. Updated results for the engine simulation, with correction factors, for all operating range from 45000 rpm to 77000 rpm were obtained. The updated model was validated with experimental data. The maximum errors were as follows:
   - Rotational speed, N : 6% and 1.5% in transient and steady state, respectively.
   - Temperature, T_{03}: 6% and 1.9% in transient and steady state respectively.
   - Pressure, p_{02}: 9.5% and 5.5% in transient and steady state respectively.

4. An on-line estimation technique based on dual estimation unscented Kalman filter, was developed and implemented using Simulink. The nonlinear engine simulation developed was used to implement this approach. Improved results were obtained in predicting the state variable (rotational speed), but, in the case of predicting the temperature T_{03} and pressure p_{02} only, slight improvements were obtained. Maximum errors obtained with respect to experimental results were:
   - Rotational speed, N : 4% and 0.8% in transient and steady state, respectively.
   - Temperature, T_{03}: 6% and 1.7% in transient and steady state respectively.
   - Pressure, p_{02}: 9% and 5.3% in transient and steady state respectively.

   The disadvantage of this method is that the use of nonlinear models makes it too slow to achieve real time health monitoring.

7.2 Thesis Contribution

The contribution given in this thesis is based on the tasks developed to meet the objectives proposed. These are:

7.2.1 Compressor map and turbine map

1. Use of a unified equation for slip factor, in the compressor map, recommended by Theodor W. von Backström [16]. This equation gives a better results than that used by Witkowski et al. [9].
2. Use of internal and parasitic loss correlations selected by Yoon et al. [15], for the compressor map, instead of the loss coefficients and scaling factors used by Witkowski et al. [9].
3. Incorporate iteration loops, used to obtain the axial component of absolute flow velocity, for both component maps, are developed in this work.

4. Equation 3.106 was modified, according to the velocity diagram at the turbine outlet (for the one-dimensional analysis in the axial turbine), from that presented by Cohen [46]. This equation has not been published in any paper.
5. Tabulated form was obtained for the compressor and turbine maps according to the suggestion done by Walsh & Fletcher [50]. This procedure was not done by Witkowski et al. [9].

Finally, it is important to mention that many equations were obtained from the Mollier diagram of the corresponding component.

7.2.2 Nonlinear engine model

The contributions of this thesis in the SR-30 engine modeling are the following:

1. Combustion efficiency, was not considered constant as it was considered by Mohan [30]. Correlation 4.22, obtained from Walsh & Fletcher [50], was used.
2. Mechanical efficiency was not considered constant. It was obtained from equation 4.31, considering the dimensions and operating conditions of SR-30 engine.
3. BETA coordinate converged with a equation developed in this work (eq. 4.73).
4. Correction factors were used to match the model results with experimental data.
5. A specific calculation procedure was developed for the steady state performance model.
6. It was used the appropriate equations to obtain the pressures, temperatures, coefficients and all the performance parameters of the SR-30 engine, which will serve to make the engine model validation.

7.2.3 On-line Engine Parameter Estimation

The contributions are:

1. It was implemented the dual unscented Kalman filter (DUKF) for the SR-30 engine. This was not done before.
2. It was compared the behavior of DUKF with eight and five deviation parameters. Deviation parameters such as compressor pressure ratio deviations, mechanical efficiency deviations, and combustion efficiency deviations, taking into account in this work, were not considered in other publications.
3. The implementation of DUKF was done in Simulink/Matlab environment.

7.3 Recommendations

1. In order to further improve characteristic map models, it is suggested to perform the validation with experimental results or with maps obtained from the manufacturer, if available.
2. Additional improvements to the SR-30 engine model include considerations such as:
   - Consider humidity in the calculation of properties.
   - Search for correlations, that best represent the combustion and mechanical efficiency.
   - Study if it is necessary to include the effects of transient phenomena, as heat soakage, in the combustor.
3. The implementation of the health parameter estimation, was done for tuning purposes. For future work it is suggested to apply the dual filter in the implementation of diagnostic methods. In this case, the deviation of parameters will be useful as an indication of engine condition.
4. It is recommended to compare the performance of different types of filters, and determine whether to use a particular filter or a hybrid filter to implement reliable diagnostic faults and/or control methods.

REFERENCE LIST

[1] T. Brotherton, A.J. Volponi, R. Luppold, and D.L. Simon. Enhanced self tuning on-board real-time engine model. *Proceedings of the 2003 IEEE Aerospace Conference*, March 2003.

[2] T. Kobayashi, D.L. Simon, and J.S. Litt. Application of a constant gain extended kalman filter for in-flight estimation of aircraft engine performance parameters. *ASME Paper*, September GT2005-68494.

[3] N. Sugiyama. System identification of jet engines. *ASME Journal of Engineering for Gas Turbines and Power.*, 122(19), January 2000.

[4] A. J. Volponi. Enhanced self tuning on-board real-time model (estorm) for aircraft engine performance health tracking. Technical report, National Aeronautics and Space Administration, July 2008.

[5] P. Dewallef and O. Léonard. On-line performance monitoring and engine diagnostic using robust kalman filtering techniques. *ASME Turbo Expo*, June GT2003-38379.

[6] S. Chatterjee and J. S. Litt. Online model parameter estimation of jet engine degradation for autonomous propulsion control. *AIAA*, October 2003-5425.

[7] R. Kurz and K. Brun. Degradation in gas turbine systems. *ASME Journal*, GT-345, August 2000.

[8] S.O.T. Ogaji, S. Sampath, R. Singh, and S.D. Probert. Parameter selection for diagnosing a gas-turbines performance-deterioration. *Elsevier Science Ltd.*, (73):25–46, 2002.

[9] T. Witkowski, S. White, C. Ortiz, P. Strykowski, and T. Simon. Characterizing the performance of the SR-30 turbojet engine. *Proceedings of the 2003 American Society for Engineering Education Annual Conference and Exposition*, Dec 2003.

[10] EES. Engineering equation solver. http://www.mhhe.com/engcs/mech/ees/na.html.

[11] D. May, S. Farber, V. Poirier, C. Yu Chen, and I. Stiharu. Design of a comprehensive condition monitoring system for gas turbine engines. Technical report, Mechanical Engineering, Concordia University, 2005.

[12] GasTurb. Gas turbine performance. http://www.mathworks.com/.

[13] O. Leónard, J.P. Thomas, and S. Borguet. Ten years of experience with a small jet engine as a support for education. *ASME Turbo Expo*, June 2008.

[14] B. Vertessen. Design of a variable guide vane for the SR-30 turbojet (in french). Master thesis, University of Liège, 2001.

[15] H.W. Oh, E.S. Yoon, and M.K. Chung. An optimum set of loss models for performance prediction of centrifugal compressors. *Proceeding of the Institution of Mechanical Engineers*, Apr 1997.

[16] Theodor W. von Backström. A unified correlation for slip factor in centrifugal impellers. *Journal of Turbomachinery*, 128, January 2006.

[17] A. Busemann. Das frderhöhenverhältniss radialer kreiselpumpen mit logarithisch-spiraligen schaufeln. *Z. Angew. Math. Mech.*, 8:371–384, 1928.

[18] A. Stodola. *Steam and Gas Turbines*. McGraw-Hill, New York, sixth edition, 1945.

[19] J. D. Stanitz. Some theoretical aerodynamic investigations of impellers in radial- and mixed-flow centrifugal compressors. *Trans. ASME*, (74):473–476, 1952.

[20] F. J. Wiesner. A review of slip factors for centrifugal impellers. *Trans. ASME: J. Eng. Gas Turbines Power 89*, pages 558–572, 1967.

[21] B. Eck. *Fans.* Pergamon Press, Elmford, New York, 1973.

[22] S. L. Dixon. *Fluid Mechanics, Thermodynamics of Turbomachinery.* Butterworth-Heinemann, England, 4th edition, 1998.

[23] W. Jiang, J. Khan, and R.A. Dougal. Dynamic centrifugal compressor model for system simulation. *Power Source*, (158):1333–1343, Dec 2005.

[24] J.T. Gravdahl and O. Egeland. Centrifugal compressor surge and speed control. *IEEE Transactions on Control Systems Technology, VOL. 7, NO. 5*, September 1999.

[25] S.C. Gustafson and G.R. Little. Correlation of transient and study-state compressor performance using neural networks. *Submitted to Proceedings AutoTest Con'92, Advanced Technology Session*, September 1992.

[26] K. Ghorbanian and M. Gholamrezaei. An artificial neural network approach to compressor performance prediction. *Elsevier Ltd.*, July 2008.

[27] J. Kurzke. How to get component maps for aircraft gas turbine performance calculations. *ASME paper 96-GT-164*, 1996.

[28] EcosimPro. Modeling and simulation software. http://www.ecosimpro.com/.

[29] GSP. Gas turbine simulation program. http://www.gspteam.com/.

[30] Sharma S. Mohan. Sliding mode control of gas turbines. 2007.

[31] P. Ailer, I. Santa, G. Szederkenyi, and K. Hangos. Nonlinear model-building of a low power gas turbine. *Periodica Polytechnica Ser. Transp. Eng.*, October 2001.

[32] MathWorks. Matlab/simulink. http://www.mathworks.com/.

[33] C.R. Davison and A.M. Birk. Steady state and transient modeling of a micro turbine with comparison to operational engine. *ASME Turbo Expo*, June 2004.

[34] A. Lazzaretto and A. Toffolo. Analytical and neural network models for gas turbine design and off-design simulation. *Int.J. Applied Thermodynamics*, 4(4):173–182, December 2001.

[35] R. Sekhon, H. Bassily, J. Wagner, and J. Gaddis. Stationary gas turbines a real time dynamic model with experimental validation. *Proceedings of the 2006 American Control Conference*, June 2006.

[36] R. Chacartegui, D. Snchez, A. Muoz, and T. Snchez. Real time simulation of medium size gas turbines. *Energy Conversion and Management*, 52(1):713–724, August 2010.

[37] A. J. Volponi, H. DePold, R. Ganguli, and C. Daguang. The use of kalman filter and neural network methodologies in gas turbine performance diagnostics:a comparative study. *NASA/CR*, 125(917), October 2009.

[38] T. Kobayashi and D.L. Simon. Hybrid kalman filter approach for aircraft engine in-flight diagnostics: Sensor fault detection case. *ASME Paper*, October GT2006-90870.

[39] S. Borguet, P. Dewallef, and O. Leonard. On-line transient engine diagnostics in a kalman filtering framework. *ASME Turbo Expo*, June GT2005-68013.

[40] T. Kobayashi and D.L. Simon. Application of a bank of kalman filters for aircraft engine fault diagnostics. *ASME Turbo Expo*, August GT200338550.

[41] T. Kobayashi and D.L. Simon. Evaluation of an enhanced bank of kalman filters for in-flight aircraft engine sensor fault diagnostics. *ASME Turbo Expo*, August GT200453640.

[42] Eric A. Wan and Rudolph van der Merwe. The unscented kalman filter for nonlinear estimation. *Wiley Publishing*, 2001.

[43] J. Choi, T.H. Yeap, and M. Bouchard. Online dgps correction prediction using recurrent neural networks with unscented kalman filter. *IEEE International Conference on Systems, Man and Cybernetics*, 2004.

[44] J. Choi, A.C. Lima, and S. Haykin. Unscented kalman filter-trained recurrent neural equalizer for time-varying channels. *IEEE*, 2003.

[45] Yanrui Geng. Online dgps correction prediction using recurrent neural networks with unscented kalman filter. *IGNSS Symposium*, December 2007.

[46] H. Cohen, G.F.C. Rogers, and H.I.H. Saravanamuttoo. *Gas Turbine Theory.* Longman Scientific and Technical, New York, fourth edition, 1998.

[47] M.J. Moran and H.N. Shapiro. *Fundamentals of Engineering Thermodynamics.* John Willey and Sons, United States, sixth edition, 2008.

[48] Turbine Technology Ltd. http://www.turbinetechnologies.com/.

[49] Turbine Technology. *Minilab: Gas Turbine Power System Operator's Manual.* Chetek, WI 54728, July 2006.

[50] P.P. Walsh & P. Fletcher. *Gas Turbine Performance.* Blackwell Science, United States, 2nd edition, 2004.

[51] Meherwan P. Boyce. *Gas Turbine Engineering Handbook.* Gulf Professional Publishing - Elsevier, United States, 3rd edition, 2006.

[52] M.G. Grewal and A.P. Andrews. *Kalman Filtering: Theory and Practice.* Wiley-Interscience, second edition, 2001.

[53] Dan Simon. *Optimal State Estimation.* Wiley-Interscience, fourth edition, 2006.

[54] Simon J. Julier, Jeffrey K. Uhlmann, and Hugh F. Durrant-Whyte. A new approach for filtering nonlinear systems. *In The Proceedings of the American Control Conference*, pages 1628–1632, 1995.

[55] Simon J. Julier and Jeffrey K. Uhlmann. A new extension of the kalman filter to nonlinear systems. *In Proc. of AeroSense: The 11th Int. Symp. on Aerospace/Defence Sensing, Simulation and Controls*, 1997.

[56] V. Kh. Sabitov, V. A. Repin, V. F. Kanaev, and A. A. Kil'kinov. Investigations and calculation of friction losses in dental microturbines and burrs. *Medical Instrument Scientific-Industrial Association, Kazan*, (1):26–31, February 1983.

[57] Metric. *Performance Specification: Lubricatin Oil, Aircraft Turbine Engine, Synthetic Base, Nato Code Number 0-156*, May 1997.

[58] Rudolph van der Merwe. *Sigma-Point Kalman Filters for Probabilistic Inference in Dynamic State-Space Models*. PhD thesis, OGI School of Science & Engineering at Oregon Health & Science University, 2004.

[59] K. Seldner, J.R. Mihaloew, and R.J. Blaha. Generalized simulation technique for turbojet engine system analysis. *NASA TN D-6610*, 1972.

APPENDICES

APPENDIX A
ESTIMATION OF LOSSES ON CENTRIFUGAL COMPRESSOR

Loss correlations were extracted from reference [23] and [15].

1. Internal loss correlations.

   a) Incidence loss:

   Impeller:

$$\begin{aligned}\Delta h_{iI} &= f_{iI}\frac{V_{w1}^2}{2} \\ &= f_{iI}\frac{\left[V_1 * \frac{\sin(\beta_{1b}-\beta_1)}{\sin\beta_{1b}}\right]^2}{2} \\ &= \frac{f_{iI}}{2}\left[C_{a1} - U_1\cot\beta_{1b}\right]^2; \qquad \text{J/kg}\end{aligned}$$

   Where $f_{iI} = 0.5-0.7$, f_{iI} is the incidence factor corresponding to the impeller; V_{w1} is the tangential component of impeller inlet relative velocity, V_1 is the relative velocity at station 1, β_{1b} is the blade angle, β_1 is the relative angle at station 1, C_{a1} is the axial component of the absolute flow velocity at station 1 and U_1 is the tangential velocity at station 1.

   Diffuser:

$$\begin{aligned}\Delta h_{iD} &= f_{iD}\frac{C_{2i}^2}{2} \\ &= f_{iD}\frac{\left(\sigma U_2 - C_{r2D}\cot\alpha_{2b}\right)^2}{2}; \qquad \text{J/kg}\end{aligned}$$

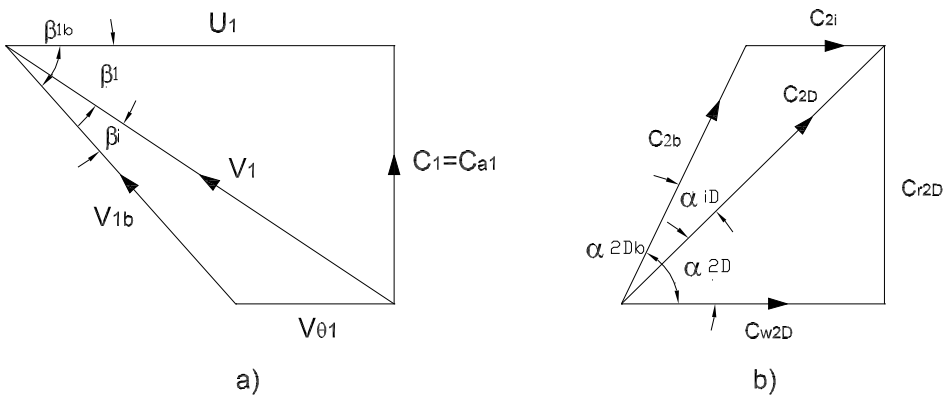

Figure A–1: a) Incidence loss for fluid entering impeller. b) Incidence loss for fluid entering diffuser.

Where from the figure (A–1.b), $C_{2i} = \sigma U_2 - C_{r2D} \cot \alpha_{2b}$. f_{iD} is the incidence factor corresponding to the diffuser; C_{2i} is the tangential component of the inlet absolute velocity at the diffuser inlet, σ is the slip factor, C_{r2D} is the radial component of the absolute flow velocity at diffuser inlet and α_{2b} is the absolute flow angle.

b) Blade loading loss:

$$\Delta h_{old} = 0.05 D_f^2 U_{2I}^2; \qquad \text{J/kg}$$

where,

$D_f = 0.4 - 0.6,$ is used to select blade pitch chord ratio.

U_{2I} : tangential impeller speed at exit.

$$D_f = 1 - \frac{V_{2I}}{V_{1t}} + \frac{0.75 \frac{\Delta h_{euler}}{U_{2I}^2}}{\left(\frac{V_{1t}}{V_{2I}}\right)\left[\left(\frac{n_b}{\pi}\right)\left(1 - \frac{D_{1t}}{D_{2I}}\right) + 2\frac{D_{1t}}{D_{2I}}\right]}$$

where D_f is the diffusion factor, V_{2I} is the relative velocity at impeller exit, V_{1t} is the relative velocity at impeller inlet tip, n_b is the number of blades, D_{1t} is the diameter at the impeller inlet tip, D_{2I} is the diameter at the impeller

exit and Δh_{euler} is the change of enthalpy of the working fluid.

b) Skin friction loss. Impeller:

$$\Delta h_{sfI} = 2C_f \frac{L_b}{D_{hyd}} \bar{W}_I^2; \qquad \text{J/kg}$$

Where:

$$\bar{W}_I = \frac{C_{1t} + C_{2I} + V_{1t} + 2V_{1r} + 3V_{2I}}{8}; \quad \text{m/s}$$

$$C_f = 0.3164(Re)^{-0.25}; \qquad \text{skin friction coefficient}$$

$$RE = 10^{-3} * \frac{\bar{\rho}_I \bar{W}_I D_{hyd}}{\mu_I}; \qquad \text{Reynolds number}$$

$$\bar{\rho}_I = (\rho_1 + \rho_{2I})/2; \qquad \text{average density, } kg/m^3$$

$$\mu_I = 1.5105 * 10^{-6} \frac{T_m^{1.5}}{T_m + 120}; \qquad \text{dynamic viscosity of dry air, } N\,s/m^2$$

$$T_m = \frac{T_1 + T_{2D}}{2}; \qquad \text{mean temperature, K}$$

$$D_{hyd} = \frac{4A_m}{P_m}; \qquad \text{impeller average hydraulic diameter, mm}$$

$$A_m = \frac{A_1 + A_{2I}}{2}; \qquad \text{mean cross section flow area, } mm^2$$

$$P_m = \pi(D_1 + D_{2D}) + 2\,b_{2I}; \quad \text{mm}$$

L_b is the impeller flow length.

Diffuser:

$$\Delta h_{sfD} = 2C_{fD} \frac{L_D}{D_{hyD}} \bar{W}_D^2; \qquad \text{J/kg}$$

Where:

$$RE = \frac{\bar{\rho}_{2D} C_{2D} D_{hyd}}{\mu_D}; \qquad \text{Reynolds number}$$

$$\bar{\rho}_{2D} = \frac{\rho_{2D} + \rho_2}{2}; \qquad \text{density, } kg/m^3$$

$$\bar{W} = C_{2b}; \qquad \text{m/s}$$

c) Clearance loss.

$$\Delta h_{cl} = 0.6 \frac{\varepsilon}{b_{2I}} C_{w2} \left\{ \frac{4\pi}{b_{2I}\, n_b} \left[\frac{r_{1t}^2 - r_{1h}^2}{(r_2 - r_{1t})(1 + \rho_2/\rho_1)} \right] C_{w2} C_1 \right\}^{1/2}; \qquad \text{J/kg}$$

where ε is the clearance, C_{w2} is the tangential component at impeller exit, r_{1t} is the radius at impeller inlet tip, r_{1h} is the radius at impeller inlet root, r_2 is the radius at impeller exit, ρ_1 and ρ_2 are the fluid density.

d) Mixing loss.

$$\Delta h_{mix} = \frac{1}{1 + \tan^2 \alpha_{2I}} \left(\frac{1 - \varepsilon_{wake} - b^*}{1 - \varepsilon_{wake}} \right)^2 \frac{C_{2I}^2}{2}; \qquad \text{J/kg}$$

where α_{2I} is the absolute angle at impeller exit, ε_{wake} is the wake fraction of blade-to-blade space and C_{2I} is the absolute flow velocity at impeller exit.

d) Vaneless diffuser loss: The mean purpose of using the vaneless diffuser is to reduce the mach number of fluid leaving the impeller.

$$\Delta h_{vld} = c_p T_{02I} \left[\left(\frac{p_{2D}}{p_{02D}} \right)^{\frac{\gamma-1}{\gamma}} - \left(\frac{p_{2D}}{p_{02I}} \right)^{\frac{\gamma-1}{\gamma}} \right]$$

where c_p is the specific heat at constant pressure, γ is the ratio of specific heat, p_{2D} is the static pressure at the diffuser inlet, p_{02D} is the total pressure at the diffuser inlet, p_{02I} is the total pressure at impeller exit and T_{02I} is the total temperature

at impeller exit.

2. Parasitic loss correlations.

   a) Disc friction loss:

$$\Delta h_{df} = f_{df} \frac{\bar{\rho}\, r_2^2\, U_2^3}{4\,\dot{m}}; \qquad \text{J/kg}$$

   where:

$$\bar{\rho} = \frac{\rho_1 + \rho_2}{2}; \qquad \text{average density, } kg/m^3$$

$$f_{df} = \begin{cases} \frac{2.67}{Re_{dif}^{0.5}} & \text{if } Re_{dif} < 3 * 10^5, \\ \frac{0.0622}{Re_{dif}^{0.2}} & \text{if } Re_{dif} \geq 3 * 10^5. \end{cases}$$

$$Re_{df} = 10^{-3} * \frac{\rho_{2I}\, U_{2I}\, r_{2I}}{\mu_{2I}}$$

   where f_{df} disc friction factor, Re is the Reynolds number, $\dot{m}$ is the mass flow and μ_{2I} is the dynamic viscosity of the working fluid.

   b) Recirculation loss:

$$\Delta h_{rc} = 8 * 10^{-5} \sinh(3.5\alpha_{2I}^3) D_f^2\, U_{2I}^2; \qquad \text{J/kg}$$

   b) Leakage loss:

$$\Delta h_{lk} = \frac{\dot{m}_{cl}\, U_{cl}\, U_{2I}}{2\,\dot{m}}; \qquad \text{J/kg}$$

Where:

$$U_{cl} = 0.816\sqrt{\frac{2\Delta P_{cl}}{\rho_{2I}}}; \qquad \text{m/s}$$

$$\Delta P_{cl} = \frac{\dot{m}(r_2\, C_{w2I} - r_1\, C_{w1})}{n_b\, \bar{r}\, \bar{b}\, L_\theta}; \qquad kg/s^2\, m$$

$$\bar{r} = \frac{r_1 + r_{2I}}{2}; \qquad \text{mm}$$

$$\bar{b} = \frac{b_1 + b_{2I}}{2}; \qquad \text{mm}$$

$$m_{cl} = \rho_{2I}\, n_b\, \varepsilon\, L_\theta\, U_{cl}; \qquad \text{kg/s}$$

where L_θ is the impeller meridional length, $\bar{b}$ is the average of impeller width and $\bar{r}$ is the average radius between the impeller inlet and outlet.